Published in final edited form as:
Prog Nucl Magn Reson Spectrosc. 2016 August ; 96: 1–46. doi:10.1016/j.pnmrs.2016.02.001.

Studying Dynamics by Magic-Angle Spinning Solid-State NMR Spectroscopy: Principles and Applications to Biomolecules

Paul Schanda[1,2,3] and **Matthias Ernst**[4]

[1]CEA, Institut de Biologie Structurale (IBS), 38027 Grenoble, France [2]CNRS, Institut de Biologie Structurale (IBS), 38027 Grenoble, France [3]Université Grenoble Alpes, IBS, 38027 Grenoble, France [4]ETH Zürich, Physical Chemistry, Vladimir-Prelog-Weg 2, 8093 Zürich, Switzerland

Abstract

Magic-angle spinning solid-state NMR spectroscopy is an important technique to study molecular structure, dynamics and interactions, and is rapidly gaining importance in biomolecular sciences. Here we provide an overview of experimental approaches to study molecular dynamics by MAS solid-state NMR, with an emphasis on the underlying theoretical concepts and differences of MAS solid-state NMR compared to solution-state NMR. The theoretical foundations of nuclear spin relaxation are revisited, focusing on the particularities of spin relaxation in solid samples under magic-angle spinning. We discuss the range of validity of Redfield theory, as well as the inherent multi-exponential behavior of relaxation in solids. Experimental challenges for measuring relaxation parameters in MAS solid-state NMR and a few recently proposed relaxation approaches are discussed, which provide information about time scales and amplitudes of motions ranging from picoseconds to milliseconds. We also discuss the theoretical basis and experimental measurements of anisotropic interactions (chemical-shift anisotropies, dipolar and quadrupolar couplings), which give direct information about the amplitude of motions. The potential of combining relaxation data with such measurements of dynamically-averaged anisotropic interactions is discussed. Although the focus of this review is on the theoretical foundations of dynamics studies rather than their application, we close by discussing a small number of recent dynamics studies, where the dynamic properties of proteins in crystals are compared to those in solution.

1 Introduction

Among the unique strengths of nuclear magnetic resonance (NMR) spectroscopy is its ability to probe molecular motion with atomic resolution in solution, solids and in the gas phase. In structural biology, solution-state NMR plays a central role in elucidating not only three-dimensional structures of proteins, nucleic acids and their complexes, but also in characterizing how these molecules fluctuate around their equilibrium positions, and how they change over time under non-equilibrium conditions. Over the last decades a wide array of techniques have been developed to study (bio-)molecular dynamics by solution-state

paul.schanda@ibs.fr maer@ethz.ch.

Europe PMC Funders Author Manuscripts

NMR spectroscopy. Nowadays, a range of different aspects of dynamics can be probed routinely by solution-state NMR, such as the amplitude of fast (picosecond-to-nanosecond) internal motion, properties of overall rotational tumbling as well as exchange processes occurring on millisecond time scales, often involving a small number of distinct states [1-5]. In addition to these equilibrium experiments, kinetic off-equilibrium approaches are available to study processes such as slow folding/unfolding and binding [6-8].

Even though solution-state NMR has proven to be a very powerful tool for studying various aspects of biomolecular structure, dynamics and function, it has several inherent limitations. (i) Solution-state NMR studies get more challenging as the molecules become larger. The slower overall tumbling leads to a rapid decay of the signal, leading to decreased resolution and sensitivity. (ii) Molecules to be studied by solution-state NMR need to be soluble at sufficient concentration. For many molecular systems of biological interest these two points cannot easily be met: many interesting biological processes involve large assemblies of molecules or molecules in lipid bilayers, which are hardly amenable to solution-state preparations. (iii) Internal dynamics that is slower than the overall tumbling cannot be detected by relaxation measurements, which hinders the study of nanosecond-microsecond motions.

Magic-angle spinning (MAS) solid-state NMR does not have these inherent limitations of increasing line width with increasing molecular size, and is sensitive to all time scales without “blind spots”. However, MAS solid-state NMR spectra tend to have broader lines due to incomplete averaging of anisotropic interactions and distribution of chemical shifts. This leads to a crowding in multi-dimensional spectra especially for larger molecules with a large number of resonances. Advances in NMR hardware, sample preparation and isotope-labeling schemes, as well as development of new spectroscopic approaches have led to significant improvements in resolution and sensitivity allowing the determination of atomic-resolution structures of proteins and nucleic acids of increasing size and complexity [9-14]. This is particularly interesting since MAS solid-state NMR can study proteins, which are either non-crystalline, and thus not accessible to X-ray-diffraction methods, and/or insoluble or too large to be studied by solution-state NMR. Solid-state NMR has, therefore, opened new fields of applications to structural biology, providing atomic-resolution insight into fibrils, membrane proteins, complexes of biomolecules in the context of their native environment, such as bound to cell walls, membranes or cell organelles [15-17]. In addition to studying structure, solid-state NMR spectroscopy has also been used for over 30 years to gain information about dynamical aspects of biomolecules [18,19]. However, many questions can only now be addressed, due to the increased capabilities of MAS solid-state NMR to provide atomic resolution at sufficient sensitivity for larger molecules. Examples of such questions are: What can we learn about the dynamics-function relationship in membrane proteins or large molecular assemblies? Which molecular rearrangements do membrane transporters undergo in their native lipid-bilayer environment? How do molecules interact with entire cell organelles or cell walls? In addition to these biological questions, there are also more fundamental biophysical questions that solid-state NMR could help resolving, e.g.: How do proteins move in crystalline lattices? Does the crystalline packing impact their internal motion, compared to the solution state? How do proteins move at very low temperatures? Triggered by these perspectives and possibilities of MAS solid-state

NMR, interesting methodological developments and applications have been reported over the last decade. The present article aims at outlining the theoretical basis for dynamics measurements, and illustrating some recent applications.

This review is organized as follows. Following a basic and more qualitative overview aimed at readers who are not yet familiar with the field (Section 1.1), Section 2 revisits the theoretical foundation of nuclear spin relaxation (Redfield theory), with a particular emphasis on relaxation in rotating solids. We briefly show the derivation of the master equation of Redfield relaxation theory and highlight the parts of the derivation where solid-state NMR is distinct from the solution-state case. Section 3 focuses on ways to measure different longitudinal and transverse relaxation parameters and motional-averaged anisotropic interactions, as well as the information one can obtain by combining different experimental observables. We also investigate the validity of Redfield theory in solid-state NMR. Section 4 discusses some recent applications of biomolecular dynamics studies by solid-state NMR. Given the space limitations, we deliberately focus only on one question, namely the dynamics in crystalline proteins, and how crystal packing possibly impacts dynamics. Many of the other exciting applications of dynamics studies cannot be treated in this review. In this review we focus on spin-1/2 nuclei, and deliberately omit methods that use quadrupolar couplings, such as deuterium relaxation and line shape analysis. These approaches, (for biomolecules in particular deuterium-based experiments), have been reviewed elsewhere [19-23]. For additional complementary views of (bio-)molecular dynamics studied by solution- or solid-state NMR spectroscopy, we refer the reader to existing reviews [3,5,23-30].

1.1 General Overview of Observables Reporting on Dynamics in Solid-State NMR

Determining structure and dynamics of molecules using NMR methods relies on the sensitivity of NMR parameters to their local environment. Therefore, we would first like to review the relevant NMR interactions in diamagnetic (bio-)molecules which are listed in Figure 1a, sorted roughly according to their typical interaction strengths. The NMR interactions can be divided into spin-field interactions (Zeeman, magnetic susceptibility, chemical shift, and radio-frequency fields) and spin-spin interactions (isotropic J coupling, dipolar coupling, quadrupolar coupling).

The strongest interaction in high-field NMR is almost always the Zeeman interaction, i.e. the interaction of the spin with the applied external static magnetic field B_0. It gives rise to a precession of nuclear spins about the external magnetic field at the Larmor frequency $\nu_0 = \omega_0/(2\pi) = -\gamma B_0/(2\pi)$ and is typically in the range of tens of MHz to about 1 GHz. The Zeeman interaction is the same for all nuclei of a given type and does not provide any direct information about structure or dynamics. The electrons around a nucleus lead to a shielding or de-shielding of the effective field experienced by the nucleus relative to a reference substance and, therefore, modify the precession frequency of the spins. The interaction between the nucleus and the induced fields are typically divided into a part that is homogeneous over the material (susceptibility) and a part that is varying on an atomic length scale which is called chemical shielding or chemical shift. The electronic environment around a nucleus has in general a low symmetry and the chemical shift is an anisotropic

interaction, i.e., it depends on the orientation of the molecule with the external field. The chemical shift can be described in Cartesian coordinates by a general 3×3 matrix which can be decomposed into its isotropic part corresponding to the trace of the matrix, the first-rank tensor part corresponding to the antisymmetric part of the matrix and the second-rank tensor part corresponding to the traceless symmetric part of the matrix. The anisotropic orientation-dependent first-rank tensor part is almost always neglected since it is not directly visible in NMR spectra. Both the isotropic part and the anisotropic orientation-dependent second-rank tensor part can provide information about structure and dynamics.

Spin-1/2 nuclei experience two types of spin-spin interactions. The scalar coupling is a through-bond coupling that is mediated by the electrons in the bond(s) that connect the involved nuclear spins. The scalar coupling can be described in Cartesian coordinates like the chemical shift by a general 3×3 matrix and has isotropic and anisotropic components. The anisotropic parts are almost always neglected and it is assumed that the scalar coupling is an isotropic quantity. The second-rank anisotropic part of the J coupling has the same functional form as the dipolar coupling. Since it is typically much smaller than the dipolar coupling, it is often absorbed into the dipolar coupling leading to a small error in the distance derived from the dipolar coupling [31]. Scalar J couplings depend on the local geometry and can provide information about structure and dynamics. The dipolar coupling is the direct through-space interaction between two nuclear spins. The dipolar coupling has no isotropic but only a second-rank tensor component and is, therefore, also orientation dependent, i.e., the coupling between two spins depends on the angle between the inter-atomic vector and the magnetic field B_0. Its magnitude depends on the inverse third power of the distance between the two nuclei. Dipolar couplings are the most direct source of structural and dynamic information available in NMR spectroscopy. In quadrupolar nuclei, i.e., nuclei with a spin-quantum number of $I > 1/2$ (^{2}H ($I = 1$), ^{14}N ($I = 1$), ^{17}O ($I = 5/2$), there is an additional interaction of the quadrupolar moment with the electric-field gradient. Similar to the dipolar coupling, the quadrupolar interaction has no isotropic component and is purely described by an anisotropic second-rank tensor.

The relative strengths of these interactions are shown in Figure 1: quadrupolar couplings are often large, and for the nucleus that is of primary relevance in biomolecular systems, deuterium (^{2}H), it has a strength (i.e., an anisotropy of the tensor, see Section 3.4 for definitions) of about 200 kHz. The dipolar coupling has an anisotropy in the range of a few kHz to tens of kHz for directly bound nuclei, while typical CSA anisotropies are on the order of several kHz for biomolecules. The range of isotropic chemical shifts for a given category of nucleus (e.g. amide-^{1}H or carbonyl-^{13}C or amide-^{15}N) is of the order of several ppm for ^{1}H and ^{13}C spins, and about 20-30 ppm for ^{15}N; this range typically corresponds to a range of hundreds of Hz to several kHz on the frequency scale. Scalar-coupling constants are typically on the order of less than 200 Hz.

Dynamic processes in molecules lead to a modulation of NMR parameters as a function of time since they depend on the local environment. Any nucleus samples different states with different local environments, distances between atoms, relative orientations, or bond geometries – and thus different isotropic and anisotropic chemical shifts, quadrupolar couplings, dipolar couplings, and scalar couplings. All these different time-dependent

quantities can be used to gain information about the magnitude and time scale and in favorable cases also about the type of motion. There are several ways how this information can be obtained from NMR spectra.

The first class of experiments to measure dynamics applies to cases where the motion is slow compared to the interaction strength under consideration (Figure 1c). The most prominent example here is the case of exchange between states with different isotropic chemical shifts. If the exchange is slow, i.e., if the rate of exchange is much slower than the chemical-shift difference (in angular frequencies) between the states, then one observes distinct resonance frequencies corresponding to the individual states. Exchange spectroscopy (EXSY) [32] or chemical-exchange saturation transfer (CEST) [33,34] experiments allow elucidating the dynamic processes between the different states. As isotropic chemical-shift averaging in solids is identical to solution-state NMR, we will not treat such experiments in this review, and refer the reader to literature on this topic [35]. In the solid state, it is possible to extend the concept of exchange spectroscopy also to anisotropic interactions, i.e., to dipolar-coupling and anisotropic chemical-shift interactions. The so-called CODEX experiments [36-39] probe the slow exchange of states with different CSA or dipolar couplings. These techniques are not within the scope of this review, and have been treated elsewhere [27].

If the dynamic process becomes faster and is on a time scale comparable to the interaction strength, a situation often called “intermediate exchange” regime, one can observe line broadening (see Figure 1d). This is well known and exploited for the case of isotropic chemical-shift exchange. If an exchange process occurs at a rate that is comparable to the chemical-shift difference between the involved states, i.e. $k_{ex} \approx |\Delta\Omega|$, the exchange process leads to broadening of the peaks. In the slow-to-intermediate regime ($k_{ex} \lesssim |\Delta\Omega|$) one may observe separate lines for each state, each broadened by the exchange, while if the exchange occurs on the fast-to-intermediate time scale, a single frequency (the population-weighted averaged between the two conformations) is observed, but it is broadened due to exchange. By quantitatively measuring the line broadening, one can obtain detailed information about the underlying process, even if one of the exchanging states has only a small population of few percent and cannot be observed directly in the spectrum. In solution-state NMR, so-called relaxation-dispersion experiments (CPMG or $R_{1\varrho}$ relaxation dispersion) have been developed and applied very successfully to biomolecules, being used over the last two decades to gain insight into low-populated states, such as folding intermediates or marginally populated alternative conformers of proteins [1,40-43]. Recent studies that probe conformational exchange in the solid state, based on isotropic chemical-shift fluctuations, are discussed in Sections 3.3.3 and 3.3.4 [44,45]. Unlike in solution, where anisotropic interactions are averaged out by fast molecular tumbling, exchange in the solid state can also occur in the “intermediate regime” with respect to dipolar couplings or CSA interactions. In Section 3.4 we show using simulations that the dipolar powder patterns are broadened if the exchange occurs on a time scale of microseconds similar to the exchange broadening of isotropic lines in liquids. In this exchange regime, one can observe interference between the various time-dependent processes present in a MAS solid-state NMR experiment: magic-angle spinning (at frequencies of tens of kilohertz), radio-frequency irradiation (at up to ~100 kHz nutation frequencies) and dynamic processes on the time scale of microseconds.

Examples for such interference effects are found in $R_{1\varrho}$ experiments (discussed in Section 3.3.4).

For even faster processes where the dynamics are fast relative to the strength of a given interaction, the interaction is averaged, i.e., the NMR parameter one can observe is the average over all the sampled states. The best-known example in this context is the averaging of the isotropic chemical shift in the fast-exchange regime. If a spin exchanges between states in which it has different isotropic chemical shifts, the observable chemical shift is the population-weighted averaged over these states. The criterion for this averaging is that the rate of dynamic exchange (in s^{-1}) is much faster than the isotropic chemical-shift difference between the involved states (in angular frequencies). The same principles apply also to the anisotropic interactions. The anisotropic interactions considered here (dipolar couplings and the anisotropy of the chemical shift) have typical interaction strengths of several kilohertz, and are thus averaged by motion occurring on time scales shorter than tens of microseconds (see Figure 1b). For quadrupolar couplings, which are often significantly larger, the time scale over which averaging occurs is, accordingly, shorter. Purely second-rank interactions like the dipolar coupling, quadrupolar coupling and (the anisotropic part of the) chemical-shift tensors have an isotropic average of zero. As a consequence of this, in isotropic solution the anisotropic interactions are all averaged to zero by the overall molecular tumbling. Consequently, one cannot obtain any information about internal motion from the averaged anisotropic interactions, as they are averaged to zero even without internal motion. In contrast, in the solid state the overall tumbling is absent. In solid-state NMR, the anisotropic interactions are averaged out by MAS, which is a continuous and deterministic rotation at constant frequency. We use the term deterministic here and throughout this review to distinguish such processes (e.g., sample rotation) from stochastic processes (e.g., Brownian motion in liquids or methyl rotation). While the former show a predictable and uniform behavior, the latter are random and vary over the ensemble of spins. Through the use of recoupling sequences MAS averaging can be (partially) cancelled, such that one can measure the anisotropic interactions in MAS solid-state NMR (see Section 3.4). Comparing the observed interaction strength to the expected one for the rigid-limit case provides direct access to the amplitude of the motion underlying the averaging. This works best for dipolar couplings where the rigid-limit value can easily be calculated from the distance of the two nuclei. For CSA tensors and quadrupolar couplings, quantum-chemical calculations have to be used to obtain a good estimate of the rigid-limit value. In Section 3.4 we discuss in detail the information that can be obtained from partially averaged anisotropic interactions and ways to measure them. We also show the transition from the fast regime through an intermediate regime to the slow regime on the dipolar-coupling time scale.

In the fast motion limit, one can use second-order perturbation theory to calculate the line broadening induced by the time-dependent modulation of the interactions (see Figure 1e). The most common form used in NMR is Redfield relaxation theory (see Section 2) [46-48]. Nuclear spin relaxation is induced by the presence of a fluctuating magnetic field at the location of the nucleus. Many processes can generate fluctuating local magnetic fields. In our context, reorientation of orientation-dependent interactions, i.e., dipolar couplings, chemical-shift anisotropies, or quadrupolar couplings are the most important source. Nuclear spin relaxation drives the spin system back to thermal equilibrium where the density

operator can be described by Boltzmann distribution of the diagonal elements. The rate of these relaxation processes depends on the amplitude of the magnetic-field fluctuation, i.e., the amplitude of motion and the magnitude of the interaction. Furthermore, the efficiency of the relaxation process depends on the time scale of the dynamic process. The rate constants of nuclear spin relaxation contain, therefore, information not only about the amplitude but also about the time scale of the motional process. For longitudinal relaxation, i.e., the relaxation that reestablishes the Boltzmann equilibrium of the diagonal elements of the density operator (populations), the relevant frequencies correspond to the Larmor frequencies of the involved nuclei (picosecond-to-nanosecond time scales). Transverse relaxation, i.e., the decay of off-diagonal elements of the density operator (coherence), is also sensitive to slower motion, i.e. motions on time scales of nanoseconds to milliseconds. The theory of relaxation and use of relaxation parameters are discussed in detail in Sections 2 and 3.

It is instructive to consider the differences between dynamics measurements in solution and in the solid state. In solution, molecules tumble rapidly and isotropically on time scales of picoseconds to nanoseconds. As a consequence, all anisotropic interactions are averaged to zero, leading to high-resolution spectra. In the solid state, molecules are static and in a solid sample dipolar-coupling and chemical-shift interactions lead to very broad spectral features, generally tens of kilohertz large. This broadening is usually larger than the isotropic chemical-shift range, which makes it impossible to obtain any atomic-resolution information. Magic-angle spinning (MAS) is the method of choice to average the anisotropic interactions in order to get back spectral resolution. In a first-order average-Hamiltonian treatment, MAS completely averages these interactions to zero, leading to high-resolution spectra. However, in many cases the averaging by MAS is incomplete since higher-order terms lead to a residual line broadening (see Section 3.1). Thus, the way anisotropic interactions are averaged in solution and in solids is fundamentally different: while it is stochastic and fast (nanoseconds) in solution, it is due to a periodic deterministic process of sample rotation on a microsecond time scale in MAS solid-state NMR. These differences have important consequences for the measurement of dynamic properties. First, in solution the anisotropic interactions are averaged to zero by overall molecular motion, and they do, therefore, not lead to any observable splitting in NMR spectra. Consequently, the averaging of these interactions by restricted internal motion is not visible, as they are already fully averaged by overall motion. In contrast, in MAS solid-state NMR these interactions are only rendered time-dependent in a deterministic manner, and by use of appropriate recoupling sequences the anisotropic interactions can be measured. The amount of averaging seen in such measurements provides rich information about motion (see Figure 1b and Section 3.4). Furthermore, in solution the isotropic overall molecular tumbling leads to a decay of all correlation functions to zero on a time scale of nanoseconds. Consequently, internal motion that occurs on time scales slower than the overall tumbling (i.e., on nanosecond-to-microsecond time scales) becomes invisible to solution-state NMR relaxation studies. This is in contrast to MAS solid-state NMR where overall motion is absent, and where relaxation parameters are sensitive to motions from picoseconds to milliseconds. The fact that the averaging process – MAS – is controlled by the spectroscopist, rather than by random Brownian motion also offers opportunities that are not accessible in solution: there may be

interference effects between the dynamic process, MAS and possibly also an applied RF field, and this interference can be exploited to obtain information about the dynamic process (see e.g. Section 3.3.3).

We note, thus, that solid-state NMR provides more ways to obtain information about dynamics than solution-state NMR, in the sense that it has more observables, e.g., partially averaged anisotropic interactions, and that internal molecular motions occurring on a wider range of time scales can be probed by relaxation measurements. There are, however, also a number of challenges in the measurement and interpretation of dynamics data from MAS solid-state NMR. In particular, as we will discuss in Section 3.1, the time evolution of the density operator in solids is generally due to (i) relaxation (which is due to dynamic properties of the molecule) and (ii) coherent interactions, which are not perfectly averaged by MAS, such as so-called dipolar dephasing and spin diffusion (see Figure 1f). The latter is unrelated to molecular motion, and it may lead to faster evolution of elements in the density operator than the actual relaxation process, such that evolution due to the dynamic process is masked. Measuring relaxation in MAS solid-state NMR is, therefore, challenging, and the obtained rate constants are prone to systematic errors, as contributions not related to dynamics may dominate the measured rate constants and line widths. Another point requires attention when interpreting relaxation data in solids: in the derivation of Redfield theory, which is used generally for quantitative analysis of relaxation, the assumption is made that the process causing relaxation is fast (see Section 2 for details). In solution state this is almost always true, due to the fast overall tumbling. As the tumbling is absent in solids, and the motional process slow, one needs to question the validity of this theory. We investigate this question in Section 2, and in more detail in 3.3.5.

2 Relaxation Theory

2.1 Summary of Redfield Relaxation Theory

2.1.1 Semi-Classical Derivation of the Master Equation—In this section we give a short summary of the derivation of semi-classical relaxation theory as formulated by Wangsness, Bloch, and Redfield (WBR theory) [46-48]. For a detailed derivation and discussion and more details we refer the interested reader to the secondary literature about spin relaxation [25,49-53]. The full system Hamiltonian in the laboratory frame is written as

$$\mathscr{H}(t) = \mathscr{H}_0(t) + \mathscr{H}_1(t) \quad (1)$$

where the deterministic Hamiltonian $\mathscr{H}_0(t)$ in the laboratory frame usually consists of a static part (Zeeman interaction and isotropic interactions) and a time-dependent part that represents the radio-frequency irradiation of the spins. The stochastic Hamiltonian $\mathscr{H}_1(t)$ contains the time-dependent interactions due to the stochastic processes, which can in addition be modulated by magic-angle spinning (MAS). The modulation of the Hamiltonian by stochastic processes are the source of relaxation phenomena. In the following we will neglect the time-dependent part of the deterministic Hamiltonian for the derivation of the

master equation and discuss the influence of magic-angle spinning and radio-frequency terms at a later stage without detailed derivation.

The Liouville-von-Neumann equation

$$\frac{d}{dt}\sigma\left(t\right)=-i\left[\mathscr{H}\left(t\right),\sigma\left(t\right)\right] \quad (2)$$

describes the time-evolution of the density operator $\sigma(t)$ in the laboratory frame. To isolate the effect of the stochastic part of the Hamiltonian on the density operator, we transform the Hamiltonian into an interaction-frame representation, which eliminates the deterministic Hamiltonian $\mathscr{H}_0\left(t\right)$. An operator Q in the laboratory frame is transformed into the interaction frame according to

$$\tilde{Q}\left(t\right)=e^{i\mathscr{H}_0 t}Qe^{-i\mathscr{H}_0 t} \quad (3)$$

Here, the notation '~' over an operator indicates that it is in the interaction frame. The modified Liouville-von-Neumann equation in the interaction frame is given by

$$\frac{d}{dt}\tilde{\sigma}\left(t\right)=-i\left[\tilde{\mathscr{H}}_1\left(t\right),\tilde{\sigma}\left(t\right)\right] \quad (4)$$

and no longer contains the deterministic part of the Hamiltonian $\mathscr{H}_0$ explicitly.

A formal integration of the Liouville-von-Neumann equation leads to

$$\tilde{\sigma}\left(t\right)=\tilde{\sigma}\left(0\right)-i\int_0^t\left[\tilde{\mathscr{H}}_1\left(t'\right),\tilde{\sigma}\left(t'\right)\right]dt'. \quad (5)$$

We can now insert Eq. (5) into the right-hand side of Eq. (4) and obtain

$$\frac{d}{dt}\tilde{\sigma}\left(t\right)=-i\left[\tilde{\mathscr{H}}_1\left(t\right),\tilde{\sigma}\left(0\right)\right]-\int_0^t\left[\tilde{\mathscr{H}}_1\left(t\right),\left[\tilde{\mathscr{H}}_1\left(t'\right),\tilde{\sigma}\left(t'\right)\right]\right]dt'. \quad (6)$$

After a variable substitution using $t'=t-\tau$, $dt'=-d\tau$ and adjusting the integration boundaries we obtain

$$\frac{d}{dt}\tilde{\sigma}\left(t\right)=-i\left[\tilde{\mathscr{H}}_1\left(t\right),\tilde{\sigma}\left(0\right)\right]-\int_0^t\left[\tilde{\mathscr{H}}_1\left(t\right),\left[\tilde{\mathscr{H}}_1\left(t-\tau\right),\tilde{\sigma}\left(t-\tau\right)\right]\right]d\tau. \quad (7)$$

At this point, we have to introduce two modifications into Eq. (7):

(i) We take an ensemble average over all terms. This is necessary despite the fact that the density operator represents already an ensemble average because the stochastic Hamiltonian $\mathscr{H}_1(t)$ is a random function of time and space and different parts of the system will evolve differently under the stochastic Hamiltonian leading to differences in the time evolutions of the density operator. We require that $\mathscr{H}_1(t)$ describes a bias-free perturbation, i.e., the ensemble average $\overline{\mathscr{H}_1(t)}=0$. As a consequence of this the first term of Eq. (7) becomes zero under the ensemble average and can be dropped.

(ii) We replace $\tilde{\sigma}(t-\tau)$ by $\tilde{\sigma}(t-\tau)-\sigma_{\mathrm{eq}}$ where σ_{eq} describes the thermal equilibrium of the spin system. This modification is needed because the lattice has a finite temperature while we have assumed no temperature in our model and identical absorption and emission probabilities. We end up with

$$\frac{d}{dt}\overline{\tilde{\sigma}(t)}=-\int_0^t\overline{\left[\tilde{\mathscr{H}}_1(t),\left[\tilde{\mathscr{H}}_1(t-\tau),\tilde{\sigma}(t-\tau)-\sigma_{\mathrm{eq}}\right]\right]}d\tau \qquad (8)$$

where the overbar represents the ensemble average. So far the derivation of the master equation is rigorous except for the ad-hoc introduction of the thermal-equilibrium density operator.

At this point we have to make an *assumption* about the time scale of the stochastic process that leads to random fluctuations of the local fields. We *assume* that the time scale of the random fluctuations described by τ is much shorter than the variation in $\overline{\tilde{\sigma}}$ which is on the time scale of *t*. This assumption is sometimes referred to as the “weak collision” limit or Redfield limit since we assume that each event that leads to relaxation will change the state of the system only weakly and many events are required before a change in the density operator can be observed. An alternative, related formulation of the weak collision limit is that the characteristic frequency of the relevant interaction is small compared to the time scale of the motion that modulates this interaction [52]. It is important to keep this weak-collision limit in mind, in particular when dealing with relaxation in solids. In solution state NMR, this assumption is typically fulfilled because the molecular tumbling is generally on a much shorter time scale than the relaxation process since slow tumbling leads to broad lines that are unobservable. In solids, where molecular tumbling is absent, the validity of Redfield theory has to be evaluated carefully in each case especially for transverse relaxation rates that are sensitive to slow motions. We will address this question further in section 3.3.5.

Under this assumption we can replace $\tilde{\sigma}(t-\tau)$ by $\tilde{\sigma}(t)$ in the right-hand side of Eq. (8) and drop the overbar on the left-hand side of Eq. (8). We can then also replace the upper integration boundary by infinity since $\tau \ll t$. This leads to the master equation for relaxation in the interaction-frame representation given by

$$\frac{d}{dt}\tilde{\sigma}(t)=-\int_0^\infty\overline{\left[\tilde{\mathscr{H}}_1(t),\left[\tilde{\mathscr{H}}_1(t-\tau),\tilde{\sigma}(t)-\sigma_{\mathrm{eq}}\right]\right]}d\tau. \qquad (9)$$

We transform now the Eq. (9) back into the laboratory frame leading to the master equation for relaxation in the laboratory frame

$$\begin{aligned}\frac{d}{dt}\sigma(t) &= -i\left[\mathscr{H}_0(t),\sigma(t)\right]-\int_0^\infty\overline{\left[\mathscr{H}_1(t),\left[e^{-i\mathscr{H}_0\tau}\mathscr{H}_1(t-\tau)e^{i\mathscr{H}_0\tau},\sigma(t)-\sigma_{\mathrm{eq}}\right]\right]}d\tau\\ &= -i\left[\mathscr{H}_0(t),\sigma(t)\right]-\hat{\Gamma}\left\{\sigma(t)-\sigma_{\mathrm{eq}}\right\}\end{aligned} \tag{10}$$

where the relaxation super operator $\hat{\Gamma}$ is defined by

$$\hat{\Gamma}\{Q\}=\int_0^\infty\overline{\left[\mathscr{H}_1(t),\left[e^{-i\mathscr{H}_0\tau}\mathscr{H}_1(t-\tau)e^{i\mathscr{H}_0\tau},Q\right]\right]}d\tau. \tag{11}$$

Using the commutator super operator $\hat{\mathscr{H}}_0(t)$ leads to the equivalent formulation

$$\frac{d}{dt}\sigma(t)=-i\hat{\mathscr{H}}_0(t)\sigma(t)-\hat{\Gamma}\left\{\sigma(t)-\sigma_{\mathrm{eq}}\right\}=\hat{\mathscr{L}}\sigma(t)+\hat{\Gamma}\sigma_{\mathrm{eq}}. \tag{12}$$

2.1.2 Operator Formulation of Relaxation Theory—Many relaxation processes are induced by the random rotation (rotational diffusion) or the internal mobility of the molecules. Treating rotations is facilitated by choosing an adapted basis for expressing the interactions. While the Cartesian basis would make the treatment of rotations mathematically complicated, the spherical-tensor basis [54,55] is ideally suited for describing rotations. We, thus, write the Hamiltonian $\mathscr{H}_1(t)$ in spherical-tensor notation as

$$\mathscr{H}_1(t)=\sum_\mu\sum_\ell\sum_{m=-\ell}^{\ell}(-1)^m A^{(\mu)}_{\ell,-m}(t)\,T^{(\mu)}_{\ell,m} \tag{13}$$

where the $A^{(\mu)}_{\ell,-m}(t)$ are the space-tensor components and the $T^{(\mu)}_{\ell,m}$ are the spin-tensor components of the interaction (μ) with rank ℓ[55]. The parameter m is the magnetic quantum number characterizing the component of the tensor. After some transformations, one obtains the final form of the relaxation super operator, $\hat{\Gamma}\{Q\}$ which describes the transformation of a spin operator Q under the action of the relaxation super operator

$$\hat{\Gamma}\{Q\}=\frac{1}{2}\sum_{\mu,\mu'}\sum_{\ell,\ell'}\sum_{m,m'}(-1)^{m+m'}\sum_{p'}J^{\left(\mu,\mu'\right)}_{\ell,\ell',-m,-m'}\left(\omega_{p'}\right)\left[T^{(\mu)}_{\ell,m}\left[V^{\left(\mu'\right)}_{p'},Q\right]\right]. \tag{14}$$

Here, the operators $V^{\left(\mu'\right)}_{p'}$ are an expansion of the spherical-tensor operators $T^{\left(\mu'\right)}_{\ell',m'}$ in terms of eigenoperators of the Hamiltonian commutator super operator $\hat{\mathscr{H}}_0$, i.e.,

$$\hat{\mathscr{H}}_0 V_{p'}^{(\mu')} = \omega_{p'} V_{p'}^{(\mu')} \quad (15)$$

and $T_{\ell',m'}^{(\mu')} = \sum_{p'} V_{p'}^{(\mu')}$. The double commutator of the spin part selects the relaxation pathways that are allowed by the interactions (μ) and (μ') and the operator $V_{p'}^{(\mu')}$ determines the frequency $\omega_{p'}$. The spectral-density functions $J_{\ell,\ell',-m,-m'}^{(\mu,\mu')}(\omega_{p'})$ are the Fourier transform of the correlation functions and are defined as

$$J_{\ell,\ell',-m,-m'}^{(\mu,\mu')}(\omega) = \int_{-\infty}^{\infty} C_{\ell,\ell',-m,-m'}^{(\mu,\mu')}(\tau)\, e^{i\omega\tau} d\tau = \int_{-\infty}^{\infty} \overline{A_{\ell,-m}^{(\mu)}(t) \left(A_{\ell',-m'}^{(\mu')}(t-\tau)\right)^*}\, e^{i\omega\tau} d\tau \quad (16)$$

The spatial part characterizes the stochastic process and determines the strength of the relaxation pathway. Since the auto- and cross-relaxation processes of different operators Q are sensitive to the spectral-density function at different frequencies, the different relaxation-rate constants are sensitive to motions on different time scales. Because the integration in Eq. (11) extends only from zero to infinity, there can also be an imaginary component to the spectral-density function that causes (small) dynamic-frequency shifts [24,25,52,56,57]. For simplicity we have neglected this part in the discussion here.

Note that the indices μ and μ' in Eqs. (14) to (16) can, in principle, represent two different interactions. In this case the relaxation process is referred to as cross-correlated relaxation; we will deal with cross-correlated relaxation between a dipolar coupling and a CSA tensor, as well as two different CSA tensors in Section 3.3. If the relaxation is due to a correlation of an interaction with itself (i.e., $\mu = \mu'$), the relaxation process is referred to as auto-correlated relaxation. The notions of auto-correlated and cross-correlated relaxation are different from auto relaxation and cross relaxation. Auto relaxation describes a diagonal element of the relaxation super operator $\hat{\Gamma}$, i.e., the relaxation of an operator Q towards its equilibrium value. Typical auto-relaxation rate constants are $R_{1\mathrm{I}}$, i.e., Γ_{I_Z,I_Z} and $R_{2\mathrm{I}}$, i.e., Γ_{I^+,I^+}. An example of cross-relaxation is the nuclear Overhauser effect, i.e., $\sigma_{\mathrm{NOE}} = \Gamma_{I_Z,S_Z}$, which we will briefly discuss in Section 3.2 for the heteronuclear case.

Equation (14) describes the general action of the relaxation super operator on any operator Q. In order to calculate relaxation-rate constants, one needs to (i) obtain the spectral density function $J_{\ell,\ell',-m,-m'}^{(\mu,\mu')}(\omega)$ which describes a particular motion that leads to relaxation. Furthermore, (ii), we need to evaluate the double commutators in Eq. (14), and thus identify the spherical tensors $T_{\ell,m}^{(\mu)}$, which depends on the particular relaxation mechanism we consider (CSA, dipolar coupling). Determining these double commutators will tell us which

frequencies ω of the spectral-density function are relevant for a particular relaxation mechanism. The approach of calculating these two quantities, double commutators and spectral densities, is the same whether one treats solution or solid-state relaxation theory. However, as we will show in the following section the presence of MAS leads to slight modifications of the frequencies.

2.2 Relaxation in Solids

2.2.1 Correlation Functions in Solids—Key to the calculation of relaxation in solids is the correlation function defined in Eq. (16) which is orientation dependent. Under MAS we have to transform the spatial tensor components from the principal-axis system to a molecule-fixed frame, to the rotor-frame and finally to the laboratory frame. We can write these transformations as a series of Euler rotations (Figure 2) as

$$A^{(\mu)}_{\ell,-m}(t) = \sum_{n,p,q} D^{\ell}_{n,-m}(-\omega_{\mathrm{r}}t, -\theta_{\mathrm{m}}, 0) \quad D^{\ell}_{p,n}(\alpha_{\mathrm{MR}}, \beta_{\mathrm{MR}}, 0) \times D^{\ell}_{q,p}\left(\alpha^{(\mu)}_{\mathrm{PM}}(t), \beta^{(\mu)}_{\mathrm{PM}}(t), \gamma^{(\mu)}_{\mathrm{PM}}(t)\right) \rho^{(\mu)}_{\ell,q} \quad (17)$$

The transformation is time dependent for two reasons: (i) the stochastic process will modulate the transformation from the principal-axis system to the molecule-fixed frame and (ii) magic-angle spinning will lead to a time dependence of the spherical-tensor components in the laboratory frame. Typically, the MAS time dependence is much slower than the stochastic process that can be described by Redfield relaxation theory and we can assume that the MAS is quasi-static on the time scale of the correlation time. If the stochastic process and the MAS rotation are on the same time scale, interference effects are observed and the averaging by MAS becomes inefficient. This is mostly an issue for “slow” stochastic processes and will be discussed in more detail in Section 3.3. The transformations from the molecule-fixed frame to the rotor-fixed frame (powder average) and the transformation from the rotor-fixed frame to the laboratory frame will be identical for both spatial-tensor components that constitute the correlation function if we assume that the stochastic process happens on a much shorter time scale than the MAS rotation ($\tau_{\mathrm{c}} \ll \tau_{\mathrm{r}}$). The difference occurs only in the angles for the transformation from the principal-axis system into the molecule fixed frame which can be different due to the fact that we consider two different interactions (μ) and (μ'), i.e., cross-correlated relaxation or due to the fact that the stochastic process induces motion of the interaction. The correlation function is then defined as

$$
\begin{aligned}
C^{\left(\mu,\mu'\right)}_{\ell,\ell',-m,-m'}(\tau) = {} & \overline{A^{(\mu)}_{\ell,-m}(t)\left(A^{(\mu')}_{\ell',-m'}(t-\tau)\right)^{*}} \\
= {} & \sum_{n,p,q} D^{\ell}_{n,-m}(-\omega_{\mathrm{r}}t,-\theta_{\mathrm{m}},0)\, D^{\ell}_{p,n}(\alpha_{\mathrm{MR}},\beta_{\mathrm{MR}},\gamma_{\mathrm{MR}})\, \rho^{(\mu)}_{\ell,q} \times \\
& \sum_{n',p',q'} {D^{\ell'}_{n',-m'}}^{*}(-\omega_{\mathrm{r}}t,-\theta_{\mathrm{m}},0)\, {D^{\ell'}_{p',n'}}^{*}(\alpha_{\mathrm{MR}},\beta_{\mathrm{MR}},\gamma_{\mathrm{MR}})\, {\rho^{\left(\mu'\right)}_{\ell',q'}}^{*} \times \\
& \frac{}{D^{\ell}_{q,p}\left(\alpha^{(\mu)}_{\mathrm{PM}}(t),\beta^{(\mu)}_{\mathrm{PM}}(t),\gamma^{(\mu)}_{\mathrm{PM}}(t)\right) {D^{\ell'}_{q',p'}}^{*}\left(\alpha^{(\mu')}_{\mathrm{PM}}(t-\tau),\beta^{(\mu')}_{\mathrm{PM}}(t-\tau),\gamma^{(\mu')}_{\mathrm{PM}}(t-\tau)\right)}
\end{aligned}
\tag{18}
$$

One can show that only correlation functions with $\ell = \ell'$ and $m = m'$ do not vanish. For simplicity we will assume auto-correlated relaxation ($\mu = \mu'$) and a simple model where we can describe the stochastic process by a rotation about a single angle γ_{PM}. Under these conditions, the correlation function simplifies to

$$
\begin{aligned}
C^{(\mu,\mu)}_{\ell,\ell,-m,-m}(\tau) = \sum_{n,p,q} \sum_{n',p',q'} {} & e^{i\left(n-n'\right)\omega_{\mathrm{r}}t} d^{\ell}_{n,-m}(-\theta_{\mathrm{m}})\, d^{\ell}_{n',-m}(-\theta_{\mathrm{m}})\, e^{-i\left(p-p'\right)\alpha_{\mathrm{MR}}} d^{\ell}_{p,n}(\beta_{\mathrm{MR}})\, d^{\ell}_{p',n'}(\beta_{\mathrm{MR}}) \times \\
& e^{-i\left(n-n'\right)\gamma_{\mathrm{MR}}} e^{-i\left(q-q'\right)\alpha_{\mathrm{PM}}} d^{\ell}_{q,p}(\beta_{\mathrm{PM}})\, d^{\ell}_{q',p'}(\beta_{\mathrm{PM}})\, \rho^{(\mu)}_{\ell,q} {\rho^{\left(\mu'\right)}_{\ell,q'}}^{*} \overline{e^{-ip\gamma_{\mathrm{PM}}(t)} e^{ip'\gamma_{\mathrm{PM}}(t-\tau)}}
\end{aligned}
\tag{19}
$$

where the first factor describes the time dependence by MAS, the last factor the stochastic process and all other terms are just geometrical factors that characterize the linear combinations of the various angular correlation functions

$$
C^{(\gamma)}_{p,p'}(\tau) = \overline{e^{-ip\gamma_{\mathrm{PM}}(t)} e^{ip'\gamma_{\mathrm{PM}}(t-\tau)}}. \tag{20}
$$

Note that in contrast to liquid-state NMR off-diagonal contributions ($p \neq p'$) to the angular correlation functions are also important and have to be taken into account. For simple jump models or restricted or unrestricted rotational diffusion on a cone the angular correlation function can be calculated analytically.

For a two-site jump model with populations p_1 and p_2 (not to be confused with the summation variables p and p' used in the transformation of the spatial-tensor components from the PAS to the laboratory frame!) with angular positions of 0 and γ_0, jump rate constants k_{12} and k_{21}, where $p_1 = k_{21}/(k_{12}+k_{21})$ and $p_2 = k_{12}/(k_{12}+k_{21})$, and a correlation time of $\tau_{\mathrm{c}} = 1/(k_{12}+k_{21})$ we obtain a correlation function of the form [58,59]

$$C^{(\gamma)}_{p,p'}(\tau) = p_1^2 + p_2^2 e^{i\left(p-p'\right)\gamma_0} + p_1 p_2 e^{-\tau/\tau_c}\left(1 + e^{i\left(p-p'\right)\gamma_0}\right) + p_1 p_2\left(1 - e^{-\tau/\tau_c}\right)\left(e^{ip\gamma_0} + e^{-ip'\gamma_0}\right) \quad (21)$$

which corresponds to a spectral density function of the form

$$J_{p,p'}(\omega) = 8 p_1 p_2 \sin(p\gamma_0/2) \sin\left(p'\gamma_0/2\right) e^{i\left(p-p'\right)\gamma_0/2} \frac{\tau_c}{1+(\omega\tau_c)^2}. \quad (22)$$

For the restricted rotational diffusion in a cone model, the calculation of the correlation function cannot be done analytically in a closed form but only using approximations. The expressions are more complex and can be found in the literature [60].

In the model-free approach [61,62] we assume that the correlation function can be expressed by a mono-exponential decay with the functional form

$$C(\tau) = S^2 + \left(1 - S^2\right) e^{-\tau/\tau_c} \quad (23)$$

which leads to a spectral density function given by

$$J(\omega) = \left(1 - S^2\right) \frac{2}{5} \frac{\tau_c}{1+(\omega\tau_c)^2}. \quad (24)$$

In this approach there are two parameters, namely the correlation time τ_c which characterizes the time scale of the motion and the order parameter S^2 which characterizes the spatial restriction of the motion. In this case the total spectral-density function is independent of the parameters m and m' and we obtain for an two interactions μ and μ' which are both axially symmetric

$$J^{\left(\mu,\mu'\right)}_{\ell,\ell,-m,-m}(\omega) = \rho^{(\mu)}_{\ell,0} \rho^{\left(\mu'\right)}_{\ell,0} P_2\left(\cos\theta^{\left(\mu,\mu'\right)}\right)\left(1 - S^2\right) \frac{2}{5} \frac{\tau_c}{1+(\omega\tau_c)^2}. \quad (25)$$

Because of the orientation dependence of relaxation-rate constants in solids, we would like to discuss some general properties of spin relaxation in MAS NMR, which are illustrated by Figure 3. The top left panel shows the T_1 relaxation-rate constants, as induced by a dipolar coupling, in a static sample (i.e. without MAS). The upper right panel shows this rate constant as a function of the two relevant Euler angles β_{MA} and α_{RL} that characterize the orientation of a crystallite in the rotor-fixed frame (see Figure 2). The magnitude of the

Europe PMC Funders Author Manuscripts

relaxation-rate constant induced by an interaction oriented at a given orientation is indicated by a color code. For example, if the dipolar interaction has a mean orientation parallel to B_0 (and dynamics around this axis), the relaxation rate constant is at a maximum, while if it is oriented along the magic angle it is at a minimum. Magic-angle spinning corresponds to a time dependence of the relaxation-rate constant along the α_{RL} axis, i.e., the considered dipolar interaction will sample all possible values of α_{RL} during sample rotation (horizontal lines in the top right panel). Consequently, the instantaneous relaxation rate varies in the course of the sample rotation. If the relaxation rate constant is small compared to the frequency of the sample rotation, which is almost always the case, we can neglect this fluctuation as only the average rate constant is relevant. However, the rate constants for spin pairs oriented along different angles β_{MR} are not averaged by MAS. This is illustrated for three different angles in Figure 3, corresponding to spin pairs on different “carousels”. Spin pairs oriented on one of these carousels are not converted to another carousel by MAS, and spin pairs at a given β_{MR} will thus have a MAS-averaged (i.e. α_{RL}-averaged) relaxation-rate constant that is different from spin pairs at other angles β_{MR}. An important consequence of this is the inherent multi-exponential character of relaxation in solid-state NMR.

These considerations lead to the following simplifications of the correlation function. The analytical averaging over the MAS rotation (which is usually allowed because the relaxation time is much longer than the rotor period) leads to a simplified correlation function of the form

$$C^{(\mu,\mu)}_{\ell,\ell,-m,-m}(\tau) = \sum_{n,p,q}\sum_{p',q'} \left(d^{\ell}_{n,-m}(-\theta_{\mathrm{m}})\right)^2 e^{-i\left(p-p'\right)\alpha_{\mathrm{MR}}} d^{\ell}_{p,n}(\beta_{\mathrm{MR}})\, d^{\ell}_{p',n}(\beta_{\mathrm{MR}}) \times e^{-i\left(q-q'\right)\alpha_{\mathrm{PM}}} d^{\ell}_{q,p}(\beta_{\mathrm{PM}})\, d^{\ell}_{q',p'}(\beta_{\mathrm{PM}})\, \rho^{(\mu)}_{\ell,q} \rho^{\left(\mu'\right)^*}_{\ell,q'} \overline{e^{-ip\gamma_{\mathrm{PM}}(t)} e^{ip'\gamma_{\mathrm{PM}}(t-\tau)}}. \quad (26)$$

If the correlation function of the internal motion is diagonal, i.e., if the correlation function is zero for $p \neq p'$ then the total correlation function and, therefore, also the relaxation-rate constant is independent of the α_{MR} angle of the powder average and it is sufficient to average over the angle β_{MR}. Therefore, the correlation function becomes even simpler in this case and we end up with

$$C^{(\mu,\mu)}_{\ell,\ell,-m,-m}(\tau) = \sum_{n,p,q}\sum_{q'} \left(d^{\ell}_{n,-m}(-\theta_{\mathrm{m}})\right)^2 \left(d^{\ell}_{p,n}(\beta_{\mathrm{MR}})\right)^2 \times e^{-i\left(q-q'\right)\alpha_{\mathrm{PM}}} d^{\ell}_{q,p}(\beta_{\mathrm{PM}})\, d^{\ell}_{q',p}(\beta_{\mathrm{PM}})\, \rho^{(\mu)}_{\ell,q} \rho^{\left(\mu'\right)^*}_{\ell,q'} \overline{e^{-ip\gamma_{\mathrm{PM}}(t)} e^{ip\gamma_{\mathrm{PM}}(t-\tau)}}. \quad (27)$$

Based on the derivation of the master equation of relaxation (see Eq. (14), every relaxation rate constant can be written in the general form

$$R_{A,B}=\sum_m z_m J^{\left(\mu,\mu'\right)}_{\ell,\ell,-m,-m}(\omega_m)\,. \tag{28}$$

Here $J^{\left(\mu,\mu'\right)}_{\ell,\ell,-m,-m}(\omega_m)$ is the spectral-density function of the interactions μ and μ' (e.g., dipolar coupling, CSA tensor, or quadrupolar coupling) and z_m is the weight of the spectral density sampled at frequency ω_m. The weights with which the various frequencies are sampled depend on the interactions involved, e.g., T_1 relaxation caused by the CSA tensor will have different weights than the T_1 relaxation caused by dipolar couplings. Possible frequencies ω_m are sums and differences of the Larmor frequencies of the involved spins. In isotropic liquids, the spectral density functions $J(\omega)$ are independent of the values of m but they can differ in solids. Magic-angle spinning leads to a modification of the sampling of the spectral-density functions [63]. In principle, all frequencies are sampled at $\omega_i \pm n\omega_\mathrm{r}$ where n can take the values 1 and 2 since most anisotropic interactions in NMR are second-rank tensors. Note that the $n = 1$ sideband has twice the weight of the $n = 2$ sideband. Therefore, a term $n_i J_{z_i}(\omega_i)$ has to be replaced by $\sum_{m=-2}^{2} n_i/(3|m|)\, J_{z_i}(\omega_i + m\omega_\mathrm{r})$ under MAS. Since the MAS frequency is typically much smaller than the Larmor frequencies of the spins, the changes in the sampling frequency are neglected for all frequencies except for $\omega_i = 0$. In a similar way, rotating-frame relaxation leads to a modification of the sampling frequencies to $\omega_i \pm n\omega_1$ where n can be 0, 1, or 2 [64]. Since also ω_1 is typically much smaller than the Larmor frequencies, these changes are usually also neglected except for $\omega_i = 0$. If MAS and spin-lock fields are present at the same time, both modifications have to be combined usually also only for the zero-frequency term [65-67].

2.2.2 Powder Distribution of Relaxation-Rate Constants—As pointed out above, relaxation-rate constants in solids are always orientation dependent [59] and, therefore, one does not expect a mono-exponential decay or mono-exponential magnetization-transfer kinetics. The relaxation-rate constant $R_1 = 1/T_1$ of spin S in a heteronuclear two-spin system is given by

$$\frac{1}{T_1}=R_1=\Gamma_{s_z,s_z}=\frac{1}{24}J^{(\mathrm{D,D})}_{2,2,0,0}(\omega_I-\omega_S)+\frac{1}{8}J^{(\mathrm{D,D})}_{2,2,1,1}(\omega_S)+\frac{1}{4}J^{(\mathrm{D,D})}_{2,2,2,2}(\omega_I-\omega_S)+\frac{1}{2}J^{(\mathrm{C,C})}_{2,2,1,1}(\omega_S) \tag{29}$$

where we have included dipolar (D) and CSA (C) relaxation. We will exemplify the properties of the T_1 relaxation of the ^{15}N in a N-H spin system for two different motional models. The first model describes restricted rotational diffusion in a cone (sometimes referred to as “wobbling in a cone”) which is characterized by two parameters, namely the

diffusion constant D_w and the opening angle θ. The second model is a two-site jump model with jump-rate constants $k_{12} = k_{21}$ or a correlation time $\tau_c = 1/(2\ k_{12})$ and an angle γ_0 between the two orientations.

Figure 4a shows the powder-orientation dependence of the longitudinal relaxation-rate constant for a two-site jump model with a correlation time of $\tau_c = 1$ ns and a jump angle of $\gamma_0 = 30°$. The relaxation-rate constants range in value from 0.244 to 0.543 s^{-1}, which is roughly a factor of 2.2 between the minimum and the maximum value. One can clearly see the dependence of R_1 on both Euler angles α_{MR} and β_{MR} since the plane where the exchange process takes place requires two angles to orient in the rotor frame. The dependence of R_1 on the crystallite orientation for a restricted rotational diffusion in a cone model with a diffusion constant of $D_w = 2{\cdot}10^6$ s^{-1} and an opening angle $\theta = 30°$ is shown in Figure 4b. In this case the relaxation-rate constant depends only on the powder angle β_{MR} and is independent of α_{MR} since the cone where the diffusion takes place is axially symmetric and requires only a single angle to orient in the rotor frame. The relaxation rate constants cover a range from 0.10 to 0.14 s^{-1}, which is roughly a factor of 1.4. Therefore, relaxation in solids is always characterized by a multi-exponential decay but the distribution of relaxation-rate constants covers usually only a range of a factor of about two. Due to the limited signal-to-noise ratio of experimental data, such a multi-exponential decay is difficult to characterize precisely and almost always mono-exponential fits of experimental data are used. There are several possibilities to characterize the distribution of relaxation-rate constants obtained from Redfield calculations by a single mono-exponential decay time. One can either use the powder average of the rate constants, i.e.,

$$R_1 = \frac{1}{4\pi} \int_0^{2\pi} d\alpha \int_0^{\pi} R_1(\alpha, \beta) \sin\beta \, d\beta \qquad (30)$$

or one can calculate a powder average of the magnetization decays and carry out a mono-exponential fit of the decay of the powder, which corresponds to a common evaluation procedure of experimental data. Note that averaging the rate constants is not rigorous and only works because of the narrow distribution of relaxation times as a function of the crystallite orientations.

Figure 5 show the decays obtained from the true powder-averaged decays as well as the one characterized by the averaged rate constants and the one obtained from a mono-exponential fit of the powder-averaged decay with a cut off value of 5% of the initial intensity for the two models shown above. Significant differences between the three curves are only visible for very long times when the signal has decayed to less than 1% of its initial value indicating that the mono-exponential approximation is reasonable for data with limited signal-to-noise ratio. A more detailed comparison of the relaxation-rate constants obtained by the two methods can be found below.

If we characterize the relaxation-rate constant by a single mono-exponential decay constant, we can also think about using a model-free approach where we have no dependence on the crystallite orientation since the correlation function is a single exponential decay. For many

physical motional models, the model parameters can be recalculated in terms of the model-free parameters τ_c and S^2. For the two-site jump model with equal populations $p_1 = p_2 = 0.5$, the correlation time is given by $\tau_c = 1/(2\ k_{12})$ and the order parameter by $S^2 = ¼(3\cos^2\theta+1)$ where θ is the angle between the main tensor axis at the two positions. For the restricted rotational diffusion in a cone model, the correlation time is a complex function of the opening angle θ of the cone and the diffusion constant D_w [60,68] while the order parameter is given by $S^2 = (½\cos\theta(1+\cos\theta))^2$. Using these relations, we can compare the relaxation-rate constants obtained from the physical models with the equivalent rate constants obtained by a model-free approach. This allows us to compare the two approaches and see whether a model-free approach in solids is appropriate or not. For this comparison we use a simplified model where we consider only dipolar coupling and no CSA tensor. For the two-site jump model we vary the correlation time τ_c between 1 μs and 1 ps and the jump angle θ between 0° and 90° corresponding to an order parameter S^2 between 0.25 and 1.

Figure 6 shows that there are only small differences of less than 5% between the averaged rate constants or the mono-exponential fit and the rate constants obtained from the model-free approach. Taking into account the experimental inaccuracies due to limited signal-to-noise ratio of typical solid-state NMR experiments for larger systems, data evaluation using the model-free approach seems perfectly legitimate. The situation is slightly different for the restricted rotational diffusion in a cone model (Figure 7) where differences up to 25% can be observed between the rate constants obtained by the model-free approach and the averaged rate constants or the mono-exponential fit. However, the biggest errors are observed in the range of relatively long correlation times in the order of 10 ns to μs. For shorter correlation times, the differences are on the order of 5-10%, which makes the characterization of relaxation-rate constants using the model-free approach reasonable even for a motional model like restricted rotational diffusion in a cone.

3 Determination of Motional Parameters

3.1 Challenges for Measuring Relaxation Parameters in Solids

Relaxation-rate constants are very widely used in solution-state NMR to characterize dynamics [24,25], but less in solid-state NMR. Compared to solution-state NMR, both the measurement and the analysis of longitudinal and especially transverse relaxation parameters in solid-state NMR under MAS are challenging for a number of theoretical and experimental reasons:

(i) The decay of polarization and coherences in solids comprises two parts, a part that is due to coherent time evolution under an orientation- and MAS time-dependent Hamiltonian, i.e., induced by the presence of non-averaged anisotropic interactions, in particular dipolar couplings, and a part that is incoherent, i.e., induced by dynamic processes. Measuring selectively the latter, incoherent part – which reflects dynamics – is complicated by the presence of the former, coherent decay. This represents a major experimental obstacle to measuring transverse relaxation rates but is to a lesser extent also an issue when measuring longitudinal relaxation-rate constants, where coherent mechanisms lead to spin diffusion (see Section 3.2). In this manuscript we reserve the term relaxation for the incoherent part of

the decay that is due to dynamics characterized by stochastic processes. Section 3.3.1 discusses experimental difficulties of measuring transverse relaxation rates.

(ii) The validity of Redfield theory is not *a priori* granted for transverse relaxation parameters. This is due to the fact that in the derivation of Redfield theory (see Section 2.1.1) one makes the explicit assumption that the change in the density operator is negligible on the time scale of the stochastic process, which is equivalent to assuming that the relaxation-rate constant is much smaller than the rate of the dynamic process. In the absence of fast overall tumbling, this assumption may not hold, as we will show below. In Section 3.3.5 we explore how well Redfield theory is justified for a number of selected examples using numerical simulations based on the stochastic Liouville equation approach [69-71].

(iii) Relaxation of a spin can be due to stochastic fluctuations of dipolar couplings and CSA tensors, and in addition also due to isotropic chemical-shift fluctuations (often referred to as “chemical exchange”). In solution-state NMR, the overall tumbling (on a nanosecond time scale) averages dipolar couplings and CSA tensors, such that fluctuations of the anisotropic interactions on time scales of microseconds to milliseconds do not have any impact on relaxation. Therefore, in solution state one can make a clear distinction between (a) “relaxation” in the sense of Redfield, that is due to fluctuations of anisotropic interactions by Brownian tumbling and (fast) local motions since local motions on time scales slower than the overall tumbling are unobservable, and (b) (slow) chemical exchange in the sense of isotropic chemical-shift fluctuations. In contrast to that, slow motions on time scales of micro-to-milliseconds average isotropic interactions as well as anisotropic interactions in solid-state NMR and need to be taken into account when discussing line broadening and coherence decay.

(iv) As a further complication, we need to consider interference effects between different time-dependent processes. In MAS solid-state NMR the sample rotation leads to a periodic deterministic modulation of anisotropic interactions (dipolar couplings, CSA tensor, quadrupolar couplings). In a first-order average Hamiltonian approximation [55,72], MAS averages out the effects of these interactions in the spectrum. A dynamic process can be seen as an additional time-dependent process, which is stochastic in nature. As a third time-dependent process, RF irradiation during relaxation periods, such as in $T_{1\varrho}$ or CPMG [73,74] experiments needs also to be considered. If the dynamic process occurs on a time scale that is close to the time scale of the MAS rotation or the nutation frequency of the RF field or the modulation frequency, interference effects may arise. Both the MAS frequency and the RF-field amplitudes are typically on time scales of several tens of kilohertz. Therefore, we expect to see such interference effects if we are dealing with dynamic processes on microsecond time scales that are mostly relevant for transverse relaxation. For example the averaging of anisotropic interactions by MAS can partly be cancelled by dynamic processes [75,76]. Interference between MAS and RF irradiation is extensively used in solid-state NMR to generate effective Hamiltonians during selected time periods of experiments [77-80]. Such recoupling processes may be altered by a stochastic dynamics on the same time scale [81,82]. We will highlight the effects of such interference effects in Sections 3.3.3 and 3.3.5.

As pointed out above, line width (i.e., decay of coherence) in liquid-state NMR is very well understood and measurements of transverse relaxation data are straightforward. The main source of line broadening besides relaxation processes are B_0-field inhomogeneities or susceptibility effects that can be averaged by a simple Hahn-echo sequence [83] if we neglect transport processes like diffusion. In solid-state NMR the situation is more complex since there are additional factors that induce a decay of both polarizations and coherences that is not always easy to distinguish from relaxation-induced decays. In a static solid samples, the large anisotropic interactions lead to powder patterns that are tens of kilohertz large. Under MAS, the Hamiltonian describing these interactions becomes time dependent with integer multiples of the rotation frequency. Under rotor-synchronized detection conditions, we can use average Hamiltonian theory [55,72] to characterize the effective Hamiltonian under MAS through a series of time-independent average Hamiltonians of increasing order:

$$\begin{aligned}\bar{\mathscr{H}}^{(1)} &= \frac{1}{\tau_r}\int_0^{\tau_r} dt_1 \mathscr{H}(t_1)\\ \bar{\mathscr{H}}^{(2)} &= \frac{-i}{2\tau_r}\int_0^{\tau_r} dt_2 \int_0^{t_2} dt_1 \left[\mathscr{H}(t_2), \mathscr{H}(t_1)\right]\\ \bar{\mathscr{H}}^{(3)} &= \frac{-1}{6\tau_r}\int_0^{\tau_r} dt_3 \int_0^{t_3} dt_2 \int_0^{t_2} dt_1 \left(\left[\mathscr{H}(t_3), \left[\mathscr{H}(t_2), \mathscr{H}(t_1)\right]\right] + \left[\left[\mathscr{H}(t_3), \mathscr{H}(t_2)\right], \mathscr{H}(t_1)\right]\right)\end{aligned} \quad (31)$$

To understand the behavior of NMR spectra under MAS, we can use the classification of Hamiltonians introduced by Maricq and Waugh [75] into “inhomogeneous” and “homogeneous”. Inhomogeneous Hamiltonians are characterized by the fact that all terms in the Hamiltonian commute (e.g., only anisotropic chemical shifts and heteronuclear dipolar couplings or a single homonuclear dipolar coupling) leading to sharp spectra even at moderate spinning frequencies since the spectrum is fully characterized by the first-order average Hamiltonian. This is a consequence of the fact that all commutators are zero and, therefore, all higher orders of the average Hamiltonian expansion are also zero. If we release the restriction of rotor-synchronized detection, we observe a side-band manifold but for MAS frequencies approaching the magnitude of the interactions, we obtain almost perfect averaging represented by solution-state like spectra. In the case of a homogeneous Hamiltonian (e.g., a homonuclear dipolar coupling and a heteronuclear dipolar coupling or a CSA tensor or multiple homonuclear dipolar couplings), the higher-order terms are not zero leading to a residual line broadening under MAS. Assuming that the second-order average Hamiltonian is the dominating term, the residual line width scales with $1/\nu_r$ and even at the fastest MAS frequencies available today (ν_r = 130 kHz) there is still significant line broadening observable (see Figure 8).

Particularly in protonated systems where one has multiple strong homonuclear dipolar couplings, proton as well as $^{13}C/^{15}N$ coherences will decay due to the evolution under the terms of the second-order average Hamiltonian. Therefore, the apparent decay rates of spin coherences are not only reflecting relaxation, but they contain also a large contribution from coherent dephasing under the second-order average Hamiltonian term. These terms cannot be refocused easily, which makes it in practice difficult to obtain quantitative information

about dynamics from the measurement of coherence decay rates. The same Hamiltonian will lead also to a polarization-transfer process between ^{1}H or ^{13}C/^{15}N spins which is called spin diffusion [84-86] that can lead to changes in apparent T_1 times.

The above considerations point to two possible ways of reducing the effect of coherent contributions and thus providing access to quantitative relaxation-rate constants. The first one is the chemical dilution of the strong ^{1}H-^{1}H dipolar network by using deuterated samples. The deuterium spin (^{2}H) has a roughly six-fold lower gyromagnetic ratio compared to protons, thus significantly reducing dipolar dephasing. Deuteration and partial re-protonation is, therefore, an important approach for dynamics studies but also for studies of structure and interaction [87-93]. The second route to quantitative relaxation measurements comes from the realization that the second-order average Hamiltonian term scales with the inverse of the MAS frequency. Thus, the use of the highest possible MAS frequencies (currently 130 kHz) reduces coherent contributions to longitudinal or transverse decays. In practice, fast MAS is not sufficient to eliminate coherent contributions in all situations and the two approaches, deuteration and fast MAS, need to be combined to obtain quantitative data. We will discuss the requirements in more detail in the next two Sections that deal with longitudinal and transverse relaxation.

3.2 Longitudinal Relaxation Parameters in Solid-State NMR

Longitudinal relaxation times of low-γ nuclei are relatively easy to measure and evaluate compared to transverse relaxation times. This is due to the fact that only a single coherent mechanism, namely spin diffusion, can lead to a coherent time evolution of the S_z operator under MAS. Spin diffusion under MAS is mediated by second-order cross terms between two homonuclear dipolar couplings or a cross term between a homonuclear and a heteronuclear dipolar coupling [85] (for more details see Section 3.1). Spin diffusion leads to polarization transfer that can often be described by a kinetic rate equation [84] which leads to a coupling of the relaxation decays of different spins [94]. We can exemplify this with a simple example of two spins i and j that relax with different rate constants R_{1i} and R_{1j}. Without spin diffusion, the two spins will relax with their respective longitudinal relaxation-rate constants. If we include spin diffusion, we have to add a spin-diffusion rate constant k_{ij} and the decays of the two spins become coupled and are now described by a system of coupled differential equations

$$\frac{d}{dt}\begin{pmatrix}\langle I_{iz}\rangle\\ \langle I_{jz}\rangle\end{pmatrix} = -\begin{pmatrix}R_{1i}+k_{ij} & -k_{ij}\\ -k_{ij} & R_{1j}+k_{ij}\end{pmatrix}\begin{pmatrix}\langle I_{iz}\rangle\\ \langle I_{jz}\rangle\end{pmatrix} \quad (32)$$

The general solution is always a bi-exponential decay with the effective relaxation-rate constants

$$R_{\text{leff}} = \frac{R_{1i}+R_{1j}}{2} + k_{ij} \pm \sqrt{k_{ij}^2 + \left(\frac{R_{1i}-R_{1j}}{2}\right)^2} \quad (33)$$

If the spin-diffusion rate constant k_{ij} is small compared to the difference of the relaxation-rate constants, the two spins will relax with $R_{1i}+k_{ij}$ and $R_{1j}+k_{ij}$, respectively. If the spin-diffusion process is fast compared to the difference of the longitudinal relaxation-rate constants, we will observe the same effective relaxation for both spins which is described by a bi-exponential decay with rate constants $(R_{1i}+R_{1j})/2$ and $(R_{1i}+R_{1j})/2+2k_{ij}$. In the intermediate regime, the behavior is more complex. These results for a model two-spin system can be generalized to multi-spin systems and show that it is important for measuring accurate longitudinal relaxation-rate constants to have spin-diffusion rate constants that are small compared to the relaxation-rate constants and also to the differences of the relaxation rate constants that one wants to observe. Figure 9 shows numerical simulations of the difference of the effective relaxation rate constant R_{1i}^{eff} (obtained from a mono-exponential fit of the bi-exponential decay) and the correct rate constant R_{1i} as a function of the difference of the two relaxation-rate constants R_{1i} and R_{1j} and the spin-diffusion rate constant k_{ij} (see Eqs. (32) and (33)).

The role of spin diffusion in the measurement of ^{15}N R_1 rate constants has been addressed experimentally and through simulations [94-96]. The ^{15}N-^{15}N proton-driven spin diffusion rate constant has been estimated in a protonated protein at 10 kHz MAS to approximately 0.025 s^{-1}. At ambient temperature, backbone ^{15}N sites have typical R_1 rate constants of the order of 0.01 to 0.5 s^{-1} [96-100]; rate constants for side chain NH_2 groups (Asn, Gln) and Trp NHε have been reported of the order of 0.15 to 1 s^{-1} [101]; NH_3^+ groups may have significantly higher rate constants. As the spin-diffusion rate constants are only slightly smaller than backbone R_1 rate constants, one may thus expect that spin diffusion has a noticeable effect on the measured rate constants. Indeed, Chevelkov *et al* have reported a significant difference between R_1 rate constants measured at 13-24 kHz MAS frequency in a sample of protonated SH3, and a highly deuterated sample in which spin diffusion is strongly suppressed. These finding suggest that for protonated protein samples, MAS frequencies on the order of 20 kHz are not sufficient to quench the effect of spin diffusion to below detection levels. MAS frequencies in excess of 40-50 kHz in protonated systems, or deuteration (allowing for lower MAS frequencies) seem to provide accurate values.

It is noteworthy that the importance of spin diffusion depends, of course, on the absolute numbers of the relaxation-rate constants, and these change with temperature. For example, at very low temperatures, R_1 rate constants may become very small, such that at low temperature the spin diffusion may be the dominant factor governing the apparent relaxation rate constants. At high temperature, where R_1 rate constants are higher, spin diffusion may have a small or negligible effect, i.e. the actual relaxation-rate constant may be measured accurately. In contrast to relaxation, the spin-diffusion rates are not expected to vary much with temperature. This is important to keep in mind when measuring R_1 relaxation over a wide range of temperatures: in such a case one may go through a “transition” between a regime where spin diffusion is dominant (at low temperature) to a regime where it is negligible. The apparent relaxation rate would thus show some discontinuity, which one may erroneously interpret as distinct motional modes with different activation energies.

For ^{13}C the situation is more challenging than for ^{15}N, as spin-diffusion rate constants are higher. For example, for protonated alanine spinning below 20 kHz MAS, the ^{13}C relaxation

rate constants of carbonyl, C^{α} and methyl-^{13}C are essentially the same (about 1.5 to 2.5 s^{-1}) [102]. When increasing the MAS frequency to 60 kHz the respective rates differ between each other by almost a factor 50, showing that spin diffusion is strongly reduced (although the rates still may not necessarily reflect the actual relaxation rate constants). It was proposed that ~60 kHz MAS frequency may suffice to provide site-specific R_1 relaxation rate constants [102]. However, a recent study challenged this view, and showed that for $^{13}C^{\alpha}$ sites fast MAS alone is insufficient, and even deuteration and >50 kHz MAS (in a fully ^{13}C-labeled protein) is insufficient to suppress the effect of spin diffusion on $^{13}C^{\alpha}$ R_1 relaxation-rate constants. Only the combination of partial deuteration, sparse ^{13}C labeling and > 55 kHz MAS provided relaxation-rate constants that are *bona fide* without significant contributions from spin-diffusion effects [87].

The second questions related to experimental measurements of longitudinal relaxation-rate constants, is the inability to saturate the protons efficiently during the relaxation delay [52,103]. Such saturation is commonly used in liquid-state NMR to simplify the system of coupled differential equations in order to measure the real T_1 time. All longitudinal normal modes are coupled by cross relaxation [103] and for a heteronuclear I-S (e.g., ^1H-^{15}N) two-spin system we find the following system of coupled differential equations that describe the time evolution of the polarization:

$$\frac{d}{dt}\begin{pmatrix}\langle I_z\rangle\\ \langle S_z\rangle\\ \langle 2I_zS_z\rangle\end{pmatrix}=-\begin{pmatrix}\Gamma_{I_z,I_z} & \Gamma_{I_z,S_z} & \Gamma_{I_z,2I_zS_z}\\ \Gamma_{I_z,S_z} & \Gamma_{S_z,S_z} & \Gamma_{S_z,2I_zS_z}\\ \Gamma_{I_z,2I_zS_z} & \Gamma_{S_z,2I_zS_z} & \Gamma_{2I_zS_z,2I_zS_z}\end{pmatrix}\begin{pmatrix}\langle I_z\rangle-\langle I_z^{\mathrm{eq}}\rangle\\ \langle S_z\rangle-\langle S_z^{\mathrm{eq}}\rangle\\ \langle 2I_zS_z\rangle\end{pmatrix} \quad (34)$$

In principle, the time evolution of any of the coupled operators will be described by a tri-exponential function where the effective time constants and the weights of the three exponentials depend on all six relaxation-rate constants. By saturating the I spins (protons) by continuous on-resonance radio-frequency fields, we ensure that $\langle I_z\rangle(t) = \langle 2I_zS_z\rangle(t) = 0$ and the differential equation simplifies to

$$\frac{d}{dt}S_z=\Gamma_{I_z,S_z}\langle I_z^{\mathrm{eq}}\rangle-\Gamma_{S_z,S_z}\langle S_z-S_z^{\mathrm{eq}}\rangle \quad (35)$$

and the decay of the magnetization becomes mono-exponential with the decay time $\Gamma_{S_z,S_z} = 1/T_{1S}$. Since typical longitudinal relaxation-rate constants of ^{15}N and ^{13}C are in the order of seconds, high-power proton irradiation of several seconds would be required in order to saturate the protons in solids. This is experimentally impossible with current probe designs and to our knowledge all measurements of longitudinal relaxation-rate constants in solid proteins have been done without proton saturation during the relaxation delay [96,98,99,104-106]. This is justified by the action of proton spin diffusion in solids that leads to an effect that is very similar to proton saturation. If the proton spin diffusion is fast, the apparent T_1 of the proton (and of the two-spin term) become very short (see above) and we can assume that the proton polarization and the two-spin polarization is always very

close to the equilibrium value. Under these conditions we can make similar assumptions as in the case of the saturation of the protons and obtain

$$\frac{d}{dt}S_z = -\Gamma_{S_z,S_z}\left\langle S_z - S_z^{\mathrm{eq}}\right\rangle \quad (36)$$

which describes a mono-exponential decay towards the equilibrium value for the S_z magnetization. This is also illustrated in Figure 10 where we have plotted the analytical solutions for an inversion-recovery experiment on the S spin as a function of the I-spin relaxation-rate constant. In these simulations we have neglected the cross-correlated cross relaxation to the two-spin term. One can clearly see that for sufficiently large spin-diffusion rate constants on the protons, the mono-exponential decay of the ^{15}N spin is recovered without the need to apply proton saturation during the relaxation delay.

3.2.1 T_1 Relaxation—We have already seen in Section 2.2.2 that T_1 relaxation is most sensitive to motions with correlation times in the ns region since the spectral-density functions are sampled at sums and differences of the Larmor frequency which is typically in the 50-1000 MHz region. In a heteronuclear two-spin system the functional form of T_1 relaxation times are given by Eq. (29) which simplifies under the assumption of a simple single-time scale model-free approach to

$$\frac{1}{T_1} = R_1 = \Gamma_{S_z,S_z} = \left(\frac{\delta_{\mathrm{D}}}{4}\right)^2 \left(J(\omega_I - \omega_S) + 3J(\omega_S) + 6J(\omega_I + \omega_S)\right) + \delta_{CSA}^2 \frac{3}{4} J(\omega_S) \quad (37)$$

where the spectral-density function is given by

$$J(\omega) = \frac{2}{5}\left(1 - S^2\right)\frac{\tau_{\mathrm{c}}}{1 + (\omega\tau_{\mathrm{c}})^2} \quad (38)$$

and the anisotropy of the dipolar coupling is defined by $\delta_{\mathrm{D}} = -2\frac{\mu_0}{4\pi}\frac{\gamma_I\gamma_S\hbar}{r_{IS}^3}$ while the anisotropy of the chemical-shielding tensor is $\delta_{\mathrm{CSA}} = -\gamma B_0(\sigma_{zz} - \sigma_{\mathrm{iso}})$. Here, we assume an axially-symmetric CSA tensor, e.g., the asymmetry is $\eta = 0$.

Figure 11 clearly shows that the T_1 auto-relaxation rate constant shows a maximum for a correlation time around 1 ns, which comes from the dependence of T_1 on the spectral-density function at the Larmor frequency. Unless the time scale of motion is close to this maximum, T_1 rate constants depend only weakly on S^2. Since the overall shape of the dependence on τ_{c} and S^2 does not change as a function of the static magnetic field, even measurements at multiple B_0 fields will lead to a high correlation between the two parameters. The solution to this problem is the independent measurement of transverse relaxation parameters, which depend on the spectral density at different frequencies than T_1 (see Section 3.3) and/or the direct measurement of motionally averaged dipolar couplings, which directly provide information about the order parameters (see Section 3.4). As

discussed in Section 3.5, the inclusion of dipolar-coupling measurements greatly improves the accuracy of such fits.

3.2.2 Heteronuclear Cross Relaxation (NOE)—The heteronuclear cross relaxation-rate constant Γ_{I_Z,S_Z}, i.e. the transfer of polarization from ^{1}H to ^{15}N or ^{13}C is, in the form of the steady-state NOE, a commonly measured parameter in liquid-state NMR. Saturating the I spins before the start of the experiment will lead to a change in the steady-state value of the S spins which is given by

$$\left\langle S_z^{SS}\right\rangle = \left\langle S_z^{\mathrm{eq}}\right\rangle \left(1+\frac{\Gamma_{I_z,S_z}\left\langle I_z^{\mathrm{eq}}\right\rangle}{\Gamma_{S_z,S_z}\left\langle S_z^{\mathrm{eq}}\right\rangle}\right) = \left\langle S_z^{\mathrm{eq}}\right\rangle (1+\eta) \quad (39)$$

with the cross-relaxation rate constant given by

$$\Gamma_{I_z,S_z} = \left(\frac{\delta_{\mathrm{D}}}{4}\right)^2 \left(-J\left(\omega_I-\omega_S\right)+6J\left(\omega_I+\omega_S\right)\right). \quad (40)$$

If the T_1 times of the S-spin are known, the cross-relaxation rate constant can be back calculated from the steady state NOE value η.

Figure 12a) and b) shows a plot of the steady state NOE η as a function of the order parameter and the correlation time which shows that the NOE does not give any additional information about the order parameter compared to the T_1 time. For the case of methyl groups, this correlation of longitudinal ^{13}C relaxation and heteronuclear NOE has been experimentally reported recently [107]. This correlation is a consequence of the fact that the dependence on the order parameter in the model-free approach is the same for all relaxation parameters.

Measuring the longitudinal heteronuclear cross-relaxation rate constant in the form of a steady-state NOE is straightforward but often impractical because of the low sensitivity and long relaxation times of ^{13}C/^{15}N coherences in the absence of cross polarization as an initial step of the pulse sequence. A different way to measure the NOE is in the form of a transient NOE by inverting the protons before the acquisition of the ^{13}C/^{15}N spectra [97,107]. A direct measurement of the cross-relaxation rate constant as a polarization-transfer step is difficult due to the proton spin diffusion which is in many cases much faster than the heteronuclear transfer step (see Figure 12c) and d)).

3.2.3 Longitudinal Cross-Correlated Cross Relaxation—In principle, one can also measure the longitudinal dipolar/CSA cross-correlated cross-relaxation rate constant

$$\Gamma_{S_z,2I_zS_z} = \frac{3}{4}\delta_{\mathrm{D}}\delta_{\mathrm{CSA}}J^{(IS,S)}\left(\omega_S\right) \quad (41)$$

where the spectral density function is now a cross-correlated spectral density function defined as

$$J^{(IS,S)}(\omega) = P_2(\cos\theta)\frac{2}{5}\left(1 - S^2\right)\frac{\tau_c}{1+(\omega\tau_c)^2}. \quad (42)$$

Here the θ describes the angle between the main axes of the CSA tensor and the dipolar-coupling tensor and P_2 is the second-order Legendre polynomial. Measuring the cross-correlated cross-relaxation rate constant requires the measurement of polarization transfer from the one-spin S_z term to the two-spin $2I_zS_z$ term (Figure 13). Such a transfer step can only be measured quantitatively if the proton spin-diffusion process is much slower than the transfer process. This condition is generally not fulfilled, and, to the best of our knowledge, such measurements have not yet been reported on the literature.

3.3 Transverse Relaxation Parameters in Solid-State NMR

We have analyzed in the previous section how longitudinal relaxation parameters depend on amplitudes and time scales of motions. Longitudinal relaxation parameters are proportional to the spectral density at integer multiples of the Larmor frequency of the involved nuclei (see Eq. (29)), i.e., they probe motions occurring on the time scale of nanoseconds, but they are hardly sensitive to motions on longer time scales (see Figure 11 to Figure 13). In this section we consider transverse relaxation-rate constants. We investigate the dependence of different transverse relaxation parameters on the time scale and amplitude of motion, and discuss the challenges of measuring such relaxation rates quantitatively. We show that the primary experimental challenge is to disentangle decay of coherences due to relaxation from coherence decay that is due to incompletely averaged anisotropic interactions (in particular dipolar dephasing). We also need to review the validity of Redfield theory for transverse relaxation-rate constants, as the “weak-collision” assumption underlying the derivation of this theory, i.e. the assumption that the motion is very fast compared to the change of the density operator (see Section 3.3.5) may not be valid in the regime of time scales that transverse relaxation parameters are sensitive to. In addition, we have assumed in Eq. (26) that we can average over the sample rotation if the stochastic motion is much faster than the sample rotation. For slow motions and fast MAS, this approximation might not be valid and has to be discussed in more detail.

3.3.1 T_2 Relaxation in Solids—Transverse relaxation, i.e. the decay of single-quantum coherence (S^+) under free precession in the absence of decoupling or spin lock, due to dipolar couplings and CSA tensors in static solids is characterized by

$$\frac{1}{T_2} = R_2 = \Gamma_{S^+,S^+} = \frac{1}{12}J^{(D,D)}_{2,2,0,0}(0) + \frac{1}{48}J^{(D,D)}_{2,2,0,0}(\omega_I - \omega_S) + \frac{1}{8}J^{(D,D)}_{2,2,1,1}(\omega_I) + \frac{1}{16}J^{(D,D)}_{2,2,1,1}(\omega_S) + \frac{1}{8}J^{(D,D)}_{2,2,2,2}(\omega_I + \omega_S) + \frac{1}{4}J^{(C,C)}_{2,2,0,0}(0) + \frac{1}{4}J^{(C,C)}_{2,2,1,1}(\omega_S) \quad (43)$$

It is sensitive to the $J(0)$ term of the spectral-density function, and, therefore, it provides access to slow motions. It is interesting to note here also the limits of Redfield theory. Equation (43) predicts that due to the dependence on the $J(0)$ term the T_2 rate constant increases monotonously as the time scale of the motion becomes slower. This leads to the unphysical situation that infinitely slow motion leads to infinitely fast relaxation. This contradiction can be understood remembering the assumption that was made in Redfield's derivation, which is that the time scale of the motion is much faster than the change of the density operator. Therefore, any "slow" motions in static solids lead to a breakdown of the Redfield treatment for transverse relaxation and other treatments to describe relaxation have to be used [108]. As shown below, in a rotating sample the $J(0)$ terms are replaced by terms at the MAS frequency, which at least in part resolves this situation. We will address the validity of Redfield theory under MAS in Section 3.3.5. This is much less of a problem in liquid-state NMR where fast rotational tumbling masks slow motions that modulate the anisotropic interactions. However, even in liquid-state NMR, the Redfield treatment has to be amended if slow motions lead to line broadening due to a modulation of the isotropic chemical shift ("chemical-exchange" broadening) [24].

As pointed already out in Section 2.2.1, magic-angle spinning leads to an additional modulation of the correlation function that leads to a sampling of the spectral-density function at frequencies that are offset by one or two times the spinning frequency Since the Larmor frequency is typically at least three orders of magnitude larger than the spinning frequency, these offsets are ignored for all terms except for the $J(0)$ term. Therefore, under MAS the usual form of Eq. (43) is given by [63]

$$\begin{aligned}\frac{1}{T_2}=R_2=\Gamma_{S^+,S^+}= \quad & \tfrac{1}{18}J^{(\mathrm{D,D})}_{2,2,0,0}(\omega_\mathrm{r})+\tfrac{1}{36}J^{(\mathrm{D,D})}_{2,2,0,0}(2\omega_\mathrm{r})+\tfrac{1}{48}J^{(\mathrm{D,D})}_{2,2,0,0}(\omega_I-\omega_S)+\tfrac{1}{8}J^{(\mathrm{D,D})}_{2,2,1,1}(\omega_I)+\\ & \tfrac{1}{16}J^{(\mathrm{D,D})}_{2,2,1,1}(\omega_S)+\tfrac{1}{8}J^{(\mathrm{D,D})}_{2,2,2,2}(\omega_I+\omega_S)+ \quad .\\ & \tfrac{1}{6}J^{(\mathrm{C,C})}_{2,2,0,0}(\omega_\mathrm{r})+\tfrac{1}{12}J^{(\mathrm{C,C})}_{2,2,0,0}(2\omega_\mathrm{r})+\tfrac{1}{4}J^{(\mathrm{C,C})}_{2,2,1,1}(\omega_S)\end{aligned} \tag{44}$$

Assuming again a single time-scale model-free spectral-density function of the form

$$J(\omega)=\frac{2}{5}\left(1-S^2\right)\frac{\tau_\mathrm{c}}{1+(\omega\tau_\mathrm{c})^2}, \tag{45}$$

we obtain a transverse relaxation-rate constant of the form

$$\begin{aligned}\frac{1}{T_2}=R_2=\Gamma_{S^+,S^+}= \quad & \left(\tfrac{\delta_\mathrm{D}}{4}\right)^2\left(\tfrac{4}{3}J(\omega_\mathrm{r})+\tfrac{2}{3}J(2\omega_\mathrm{r})+\tfrac{1}{2}J(\omega_I-\omega_S)+3J(\omega_I)+\right.\\ & \left.\tfrac{3}{2}J(\omega_S)+3J(\omega_I+\omega_S)\right)+\\ & \delta^2_{CSA}\left(\tfrac{1}{4}J(\omega_\mathrm{r})+\tfrac{1}{8}J(2\omega_\mathrm{r})+\tfrac{3}{8}J(\omega_S)\right)\end{aligned} \tag{46}$$

Equations for T_2 relaxation in the presence of a ^{1}H decoupling rf field have also been reported. In the presence of a continuous-wave decoupling RF field, the ω_r terms are then replaced by terms containing the difference between the rf-field strength and multiples of ω_r [109].

Figure 14 shows the calculated transverse relaxation-rate constant R_2 for a ^{15}N spin due to the dipolar interaction to a directly-bonded proton spin, and the ^{15}N CSA tensor, as derived from Eq. 46. These data show that transverse relaxation is sensitive to motion occurring on time scales of nanoseconds to milliseconds, and has a maximum in the microsecond time scale, depending on the MAS frequency. There is some qualitative similarity with longitudinal relaxation rate constants, which, however, have their maximum on a nanosecond time scale. The reason for this difference is the dependence on the spectral density at the MAS frequency in the case for R_2, or on the spectral density at the Larmor frequencies, in the case of R_1. Although both R_1 and R_2 are in principle modulated by the MAS frequency, the change of R_1 with MAS frequency can be safely neglected, because the relevant frequencies for R_1 (Larmor frequencies) are very large compared to the MAS frequency.

Accessing the R_2 relaxation-rate constant experimentally is a challenge. This is because the decay of spin coherence in solids can be due to stochastic processes (dynamics), but it can also arise from coherent dephasing arising from the presence of additional spins (in particular ^{1}H due to their large gyromagnetic ratio), as described in detail in Section 3.1. As shown in Figure 8, the line width, or (equivalently) the transverse relaxation-rate constant in the presence of multiple dipolar couplings contains a large contribution from coherent dephasing from the second-order average-Hamiltonian term. This makes it in practice difficult to interpret experimentally observed coherence decay rate constants, which contain both the actual relaxation and the effect of dipolar dephasing (the observed decay time constant in the FID is often referred to as T_2^*, to distinguish it from the actual transverse relaxation time constant $T_2 = 1/R_2$). Another important quantity in this context is the T_2' decay-time constant which is the decay of transverse magnetization under a spin-echo sequence (τ - 180° - τ). The spin-echo sequence will refocus isotropic chemical shifts, heteronuclear J couplings and also partially the second-order coherent contributions to the transverse decay rate. As discussed in Section 3.1, the coherent contribution to dephasing depends on the strength of the dipolar interactions, as well as the MAS frequency, suggesting that dipolar dephasing is potentially less problematic for ^{15}N than for ^{1}H or ^{13}C, and that deuteration and high MAS frequencies may help reducing this contribution.

It is instructive to examine whether fast MAS combined with deuteration is sufficient to obtain ^{15}N T_2' time constants that are free from dipolar dephasing. We investigate this question by analyzing experimental ^{15}N relaxation data from the microcrystalline protein ubiquitin. The ^{15}N nucleus is particularly attractive for such studies because its relaxation properties can be described to a good approximation by considering only the H-N dipole and the ^{15}N CSA tensor, and the dipolar dephasing contribution is smaller than for ^{1}H or ^{13}C. For the case of ubiquitin, dynamics have been studied extensively [44,98,110,111], such that it is known relatively well what the actual transverse relaxation rate constants (i.e. without coherent contributions) are. Figure 15 shows different ^{15}N relaxation-rate constants: data

shown in black denote the predicted $R_{1\varrho}$ rate constants, which are calculated based on dynamical amplitudes and time scales that have been determined from an extensive set of experimental data (dipolar order parameters, T_1 times, cross-correlated relaxation) [110]. They agree quite well with the experimental $R_{1\varrho}$ rate constants shown in red. These rate constants serve thus as a proxy for the "true" transverse relaxation-rate constants expected for each residue assuming that the dynamics are characterized well by the model. They were determined using Eq. (52) based on a correlation function using the extended model-free approach. As a comparison, experimental R_2' data obtained with a highly deuterated sample are shown in blue and green, where the blue data set was collected without proton decoupling, and the green data set employs 3.1 kHz WALTZ decoupling. In the sample all non-exchangeable sites are deuterated at >97%, and exchangeable sites (amides, NH_2, OH) are deuterated at 80%. This labeling leaves ^{1}H spins overall only in ~5% of all hydrogen sites in the protein. Interestingly, even in this very highly-deuterated sample, and at high MAS frequency (57 kHz), the measured R_2' rate constants are much higher than the predicted ones (black and red lines). The most likely explanation for this observation is that even under these favorable experimental conditions, R_2' rate constants do not properly reflect the dynamics of ^{15}N sites, but that a significant fraction of the observed rate is due to dipolar dephasing. Interestingly, the experimental R_2' relaxation-rate constants certainly contain some dynamic information. For example, increased R_2' for residues 23, 27 and 55 are, at least in part, due to conformational exchange [44]. However, the data in Figure 15 clearly show the large "background" from coherent contributions, hampering quantitative analysis.

Several routes have been proposed to circumvent this inherent difficulty to obtain quantitative measures of transverse relaxation. One approach is to measure the difference between two transverse relaxation-rate constants. As long as both rate constants are equally impacted by dipolar dephasing, their difference can be quantitatively analyzed in terms of dynamics. A first example is the measurement of the transverse relaxation of the two multiplet components of a ^{15}N[^{1}H] doublet (i.e., measuring the relaxation decay of $2N_xH^{\alpha}$ and $2N_xH^{\beta}$). These two components decay with rates of $R_2'+\Gamma^{CSA/D}$ and $R_2'-\Gamma^{CSA/D}$, i.e., their difference corresponds to the CSA-dipole cross-correlated cross relaxation rate constant (CCR) [112]. This CCR rate is proportional to the spectral density at $J(n\,\omega_r)$, where $n = \pm 1,2$ (see below) and, therefore, provides insights into dynamics on time scales longer than nanoseconds. A second example is the measurement of the decay of zero- and double-quantum coherences [44]. We will discuss these cross-correlated relaxation rate constants in more detail in Section 3.3.2.

A second approach is to identify relaxation-rate constants, which do not suffer from dipolar dephasing. It has been shown previously that under suitable experimental conditions (partial deuteration and fast MAS) the ^{15}N $R_{1\varrho}$ relaxation-rate constant can be quantitatively analyzed in this context [113],[114]. The data set shown in red in Figure 15 shows experimentally determined $R_{1\varrho}$ relaxation-rate constants. The close match between these experimental $R_{1\varrho}$ rate constants (red) and the predicted ones (black) suggests that one can indeed measure ^{15}N $R_{1\varrho}$ rate constants without significant contributions from dipolar dephasing. $T_{1\varrho}$ relaxation will be discussed in more detail in Section 3.3.3.

In principle, a third possible route is to employ even higher MAS frequencies, possibly combined with deuteration, to suppress coherent contributions, such that R'_2 (i.e. the decay in a spin-echo sequence) would be accessible. However, currently available MAS frequencies (on the order of 100 kHz) and deuteration do not suffice to suppress coherent contributions to the transverse decay of ^{15}N spins.

3.3.2 CSA/D and CSA/CSA Cross-Correlated Cross Relaxation—Cross-correlated cross relaxation, i.e., relaxation that arises from interference between two different interactions is one possibility towards obtaining quantitative transverse relaxation data. In this section we review two recently proposed approaches, namely relaxation due to correlation of a dipolar and a CSA interaction, and cross-correlated relaxation due to interference of two chemical-shift tensors. In principle, additional cross-correlated relaxation rates could be exploited to study dynamics, such as dipole-dipole cross-correlated relaxation, which have been used in solution state [115-119] but, to our knowledge, this has not yet been implemented experimentally.

CSA/dipole interference: The two components of a *J*-coupled doublet, for example the $2N_xH^{\alpha}$ and $2N_xH^{\beta}$ components in a scalar-coupled ^{1}H-^{15}N spin pair, may show different line widths. The physical origin of this apparent asymmetry of the doublet is the interference between two anisotropic interactions, namely the H-N dipolar coupling and the ^{15}N CSA tensor. We can distinguish different mechanisms that lead to the observed asymmetry, namely (i) a coherent mechanism that does not depend on dynamics, and (ii) an incoherent mechanism, which is due to dynamics, i.e. it depends on the amplitude and time scale of a motional process that reorients the two involved interactions.

Let us first discuss the coherent mechanisms leading to doublet asymmetry. Consider the case of a static sample (no MAS) and a rigid heteronuclear I-S spin pair and assume we observe coherences of the S spin. The local field at the location of the S spin that is due to the dipolar interaction of the I spin will have the same or opposite sign as the local field due to the S spin CSA depending on the spin state of the I spin. In the case that the I spin is in the α state (spin up) the two fields add up, while the two fields partially cancel if the I spin is in the β state (spin down). In the case of a non-spinning sample, the multiplet component belonging to the I-spin α state would, therefore, show a broad powder pattern, while the other multiplet component would show a narrower powder pattern (Figure 16). Under MAS the different line width of the two components is retained as an asymmetry of the intensity of the two respective center bands. For spinning frequencies exceeding the typical strength of the heteronuclear dipolar coupling, the two lines will show the same intensity.

In addition to this coherent interference between the S spin CSA tensor and the heteronuclear dipolar coupling, there is also a coherent interference effect between the homonuclear dipolar coupling between two S spins with the S spin CSA tensor. Since the two contributions to the Hamiltonian (CSA, homonuclear dipolar coupling) do not commute, the second-order average Hamiltonian (see Section 3.1) will be non-zero and lead to a line broadening that is different for the two multiplet lines. This coherent mechanism of differential line broadening has long been recognized [120-123]. It is reduced with increasing MAS frequency, because it is coherent in nature and the result of a second-order

average Hamiltonian term. This effect is only important for systems with homonuclear J couplings (e.g., samples which are fully ^{13}C labeled) and does not affect ^{15}N measurements. Since ^{13}C-^{13}C homonuclear dipolar couplings are typically small ($\delta_{CC}/(2\pi) \approx 4.5$ kHz) this effect can be neglected at spinning frequencies above 20 kHz even in fully-labeled samples. In the further discussion we will neglect these two coherent mechanisms of doublet asymmetry, and focus on the incoherent part.

To discuss the incoherent contributions to the line widths, we consider the situation where a H-N spin pair undergoes re-orientational dynamics. In this case, interference of the ^{15}N CSA and H-N dipolar coupling induces differential relaxation of the N-[H^{α}] and N-[H^{β}] doublet components [115,116]. The differential relaxation of the two components arises because the relaxation of one component is given by the sum of the two relaxation contributions, i.e. the ^{15}N CSA and the ^{1}H-^{15}N dipolar coupling, whereas the relaxation of the other component is given by their difference. This effect, which is known in solution-state NMR as “transverse-relaxation optimized spectroscopy” (TROSY) [124] effect has first been reported in solids by Chevelkov and Reif [112,125]. For solution-state NMR, these cross-correlated relaxation effects can be fully described within the framework of Redfield theory, and they have been extensively reviewed [115,116,126]. Due to the absence of overall tumbling, the dependence of the CSA/D CCR on the motional parameters in MAS solid-state NMR is different from what is observed in solution, and we investigate the properties of the differential relaxation in the following briefly. The reader is also referred to a comprehensive computational study of these effects [127].

The CSA/dipolar cross-correlated relaxation-rate constant within the framework of Redfield theory is given by:

$$\Gamma_{I^+,I^+S_z} = \delta_D \delta_{CSA} \left(\frac{3}{8} J^{(IS,S)}(\omega_I) + \frac{1}{6} J^{(IS,S)}(2\omega_r) + \frac{2}{6} J^{(IS,S)}(\omega_r) \right) \quad (47)$$

where the cross-correlated spectral-density function $J^{(IS,S)}(\omega)$ is defined as in Eq. (42) and $P_2(\cos\theta)$ is the second-order Legendre polynomial of the angle between the principal axes of the dipolar-coupling tensor and the S-spin CSA tensor, and δ_D and δ_{CSA} are the anisotropies of the two tensors. Here we have assumed that the CSA tensor is axially symmetric. Note that in previous studies the two terms depending on $J(\omega_r)$ have been replaced by $J(0)$ [98,128]. This way of neglecting the MAS frequency is not rigorous, as discussed in section 2.2.1, but as long as the motion is much faster than the MAS frequency the resulting errors are negligible.

In Figure 17 we investigate the CSA/dipole cross-correlated relaxation using numerical simulations of a jump model with two discrete states (Figure 17a). The ^{15}N spectra reveal differential line broadening of the two doublet components, and this line broadening is dependent on the time scale (and amplitude) of the exchange process (Figure 17b). In Figure 17c we show the cross-correlated relaxation rate constant Γ_{I^+,I^+S_z}, which for simplicity we will call here $\Gamma^{CSA/D}$, as a function of the time constant of motion, for different MAS frequencies, while Figure 17d shows additionally the dependence on the amplitude of

motion. This relaxation-rate constant can be determined from the difference of the spin-echo coherence-decay rate constants of the two doublet components $R_2'(N_xI^{\alpha})= R_2'\Gamma^{CSA/D}$ and $R_2'(N_xI^{\beta}) = R_2'\text{-}\Gamma^{CSA/D}$, where R_2' denotes the spin-echo decay time constant of the decoupled line due to incoherent as well as coherent contributions. For typical experimental signal-to-noise ratios, the differential relaxation can be detected if it exceeds approximately 1 s^{-1}; dashed lines in Figure 17 indicate that this implies that motions on a time scale from several nanoseconds to about 1 ms can be detected.

The experimental measurement of this cross-correlation effect typically involves measuring the spin-echo decay-rate constant of the two components of the scalar-coupled doublet. Experimentally it may be difficult to resolve the two components, because it requires that the ^{15}N doublet can be measured in the absence of ^{1}H decoupling. Only the use of deuteration schemes have allowed resolving $^{15}N\text{-}[^{1}H^{\alpha}]/^{15}N\text{-}[^{1}H^{\beta}]$ doublets [112]. Fast MAS helps in addition to increase resolution, and the longer coherence life times (smaller R_2') that result from fast MAS and deuteration increase sensitivity and facilitate spin-state selective transfers that allow separating the two components in two sub spectra. Experimentally, CSA/D cross-correlated relaxation-rate constants have been measured in SH3 [112,129] and later in ubiquitin [98], and these rate constants have been used for quantifying backbone dynamics [98,110,128]. The TROSY effect in solids can also be exploited for increasing sensitivity in NMR spectra for residues undergoing slow motion. It has been shown that several residues in the protein SH3 show greatly improved signal-to-noise ratio in spin-state selective polarization-transfer experiments (based on selection of the slowly-relaxing doublet component) as compared to CP transfer and scalar decoupling [130]. This idea is the same as the TROSY-type correlation experiments applied in solution state to study slowly tumbling (i.e., large) molecules.

Differential relaxation due to interference of two chemical-shift tensors: As a second example of differential relaxation we investigate the differential decay of zero-quantum (I^+S^- and I^-S^+) and double-quantum (I^+S^+ and I^-S^-) coherences. We first consider the relaxation of double- and zero-quantum terms due to the dipolar coupling between the two spins and the two CSA tensors. This leads to relaxation-rate constants given by:

$$\begin{aligned}\Gamma_{\mathrm{DQ}}= \quad & \delta_{\mathrm{D}}^2\left(\tfrac{3}{2}J(\omega_N)+6J(\omega_H+\omega_N)+\tfrac{3}{2}J(\omega_H)\right)+\\ & \delta_{\mathrm{CSA,N}}^2\left(\tfrac{3}{8}J(\omega_N)+\tfrac{2}{12}J(2\omega_{\mathrm{r}})+\tfrac{4}{12}J(\omega_{\mathrm{r}})\right)+\\ & \delta_{\mathrm{CSA,H}}^2\left(\tfrac{3}{8}J(\omega_N)+\tfrac{2}{12}J(2\omega_{\mathrm{r}})+\tfrac{4}{12}J(\omega_{\mathrm{r}})\right)+\\ & \delta_{\mathrm{CSA,H}}\delta_{\mathrm{CSA,N}}\left(\tfrac{2}{6}J^{I,S}(2\omega_{\mathrm{r}})+\tfrac{4}{6}J^{I,S}(\omega_{\mathrm{r}})\right)\end{aligned} \tag{48}$$

and

$$\begin{aligned}\Gamma_{\mathrm{ZQ}}= \quad & \delta_{\mathrm{D}}^2\left(\tfrac{3}{2}J\left(\omega_N\right)+J\left(\omega_H+\omega_N\right)+\tfrac{3}{2}J\left(\omega_H\right)\right)+\\ & \delta_{\mathrm{CSA,N}}^2\left(\tfrac{3}{8}J\left(\omega_N\right)+\tfrac{2}{12}J\left(2\omega_{\mathrm{r}}\right)+\tfrac{4}{12}J\left(\omega_{\mathrm{r}}\right)\right)+\\ & \delta_{\mathrm{CSA,H}}^2\left(\tfrac{3}{8}J\left(\omega_N\right)+\tfrac{2}{12}J\left(2\omega_{\mathrm{r}}\right)+\tfrac{4}{12}J\left(\omega_{\mathrm{r}}\right)\right)-\\ & \delta_{\mathrm{CSA,H}}\delta_{\mathrm{CSA,N}}\left(\tfrac{2}{6}J^{I,S}\left(2\omega_{\mathrm{r}}\right)+\tfrac{4}{6}J^{I,S}\left(\omega_{\mathrm{r}}\right)\right)\end{aligned} \tag{49}$$

where the cross-correlated spectral-density function $J^{(I,S)}(\omega)$ is defined in analogy to Eq. (42). The difference between zero-quantum and double-quantum relaxation due to dipolar and CSA interactions is obtained from these equations as

$$\begin{aligned}\Delta R_{\mathrm{MQ}}=\Gamma_{\mathrm{DQ}}-\Gamma_{\mathrm{ZQ}}= \quad & \delta_{\mathrm{D}}^2\left(6J\left(\omega_H+\omega_N\right)-J\left(\omega_H-\omega_N\right)\right)+\\ & 2\delta_{\mathrm{CSA},H}\delta_{\mathrm{CSA},N}\left(\tfrac{2}{6}J^{I,S}\left(2\omega_{\mathrm{r}}\right)+\tfrac{4}{6}J^{I,S}\left(\omega_{\mathrm{r}}\right)\right)\end{aligned} \tag{50}$$

Here the first term is a heteronuclear NOE term (see Eq. (40)), which turns out to be very small (below about 0.3 s^{-1} for H-N, see Figure 12) and can safely be neglected. The second term is a cross-correlated cross-relaxation term between the two CSA tensors.

In addition to the CSA and dipolar-coupling contribution, we also need to consider the effect of isotropic chemical-shift fluctuations on the zero- and double-quantum relaxation-rate constants. In the presence of conformational exchange that modulates the isotropic chemical shift of the two nuclei by $\Delta\omega_{\mathrm{I}}$ and $\Delta\omega_{\mathrm{S}}$, the chemical-shift modulation of the zero-quantum coherence is $\left|\Delta\omega_{\mathrm{ZQ}}\right|=\left|\Delta\omega_{\mathrm{I}}-\Delta\omega_{\mathrm{S}}\right|$ and the corresponding chemical-shift difference for the double-quantum term is $\left|\Delta\omega_{\mathrm{DQ}}\right|=\left|\Delta\omega_{\mathrm{I}}+\Delta\omega_{\mathrm{S}}\right|$. The differential MQ relaxation rate constant in the case of a two-site exchange is given by [131]:

$$\begin{aligned}\Delta R_{\mathrm{MQ}} \quad = & \tfrac{1}{\sqrt{8}}\left\{k_{\mathrm{ex}}^2-\Delta\omega_{\mathrm{ZQ}}^2+\left[\left(k_{\mathrm{ex}}^2+\Delta\omega_{\mathrm{ZQ}}^2\right)^2-16\Delta\omega_{\mathrm{ZQ}}^2k_{\mathrm{ex}}^2p_Ap_B\right]^{\frac{1}{2}}\right\}^{\frac{1}{2}}\\ & -\tfrac{1}{\sqrt{8}}\left\{k_{\mathrm{ex}}^2-\Delta\omega_{\mathrm{DQ}}^2+\left[\left(k_{\mathrm{ex}}^2+\Delta\omega_{\mathrm{DQ}}^2\right)^2-16\Delta\omega_{\mathrm{DQ}}^2k_{\mathrm{ex}}^2p_Ap_B\right]^{\frac{1}{2}}\right\}^{\frac{1}{2}}\end{aligned} \tag{51}$$

Here, p_{A} and p_{B} are the relative populations of the two states, and k_{ex} is the exchange rate constant defined by ($k_{\mathrm{ex}}=k_{\mathrm{AB}}+k_{\mathrm{BA}}=k_{\mathrm{BA}}(1+p_{\mathrm{B}}/p_{\mathrm{A}})$), where k_{AB} and k_{BA} are forward and backward rate constants.

In the above discussion we have considered only the two isotropic chemical shifts, the two CSA tensors and the dipolar interaction between the two spins involved in the MQ coherence, but neglected the relaxation of any of the two spins due to dipolar interactions to remote spins. This contribution can also lead to differential MQ relaxation [132]. Experimentally, the remote-spin contribution is best suppressed by extensive deuteration of the sample [44].

Summing up, differential relaxation of zero- and double-quantum coherences can arise from four contributions: (i) correlated fluctuation of two CSA tensors via the cross-correlated relaxation term in Eq. (50), (ii) correlated fluctuation of the two isotropic chemical shifts shown in Eq. (51), (iii) fluctuation of the dipolar coupling, via the heteronuclear NOE term in Eq. (50) which is often negligibly small, and (iv) dipolar relaxation by external spins which we will not consider further.

In Figure 18, we investigate differential relaxation of ^{1}H-^{15}N ZQ and DQ coherences by means of numerical simulations. The conformational exchange in our model occurs between two distinct states, similar to the model shown in Figure 17a. For this simulation, we assume that the CSA tensors of ^{1}H and ^{15}N have different orientations in the two exchanging states but each tensor retains its anisotropy δ_{CSA} in the two states. (Note that for these calculations one could of course also use the Redfield-theory Eq. (50) for the CSA/CSA contribution, and Eq. (51) for the isotropic CS interference. Indeed Eq. (51) is exactly identical to the result of numerical simulations [44]; however, in principle the Redfield approach is not strictly valid in the slow motional regime and we will compare numerical and Redfield-theory results for the CSA/CSA term in section 3.3.5.) Figure 18a investigates the case where the two states have identical *isotropic* chemical shifts, but the CSA tensors both change in the exchange process. In this case, differential relaxation is found ($\Delta R_{\mathrm{MQ}} \neq 0$) whenever the dynamic process is on a time scale from nanoseconds to about 1 millisecond. Largest ΔR_{MQ} values are found for microsecond motions while motions occurring on picosecond time scales, or slower than milliseconds do not lead to significant cross-correlated relaxation. This dependence is similar to the CSA/D cross-correlated relaxation described above. One can show that differential relaxation is only found if *both* CSA tensors are modulated, as expected for a cross-correlated relaxation (see also the $J^{I,S}$ terms in Eq. (50)). Furthermore, the sign of ΔR_{MQ} depends on the relative angle of the fluctuations of the two tensors, reflected by the product $\delta_{\mathrm{CSA,H}}\delta_{\mathrm{CSA,N}}$ [44,131]. Figure 18b shows that, just like for the CSA/D cross-correlated relaxation, the relaxation rate constant on the “slow branch” is MAS dependent, i.e. the maximum depends also on the MAS frequency. This is expected because of the dependence on the spectral-density terms at the MAS frequency, and qualitatively, it can be understood by the fact that a MAS frequency that is high compared to the motion leads to efficient averaging of the anisotropic interactions.

In these simulations we have assumed that the two states have identical ^{1}H and ^{15}N chemical shifts in the two exchanging states. In panel (c) we consider the differential ZQ/DQ relaxation induced by correlated fluctuations of the two isotropic chemical shifts. Chemical-shift fluctuations induce differential relaxation whenever the exchange-rate constant is in the range of microseconds to a few milliseconds, depending on the chemical-shift differences, the exchange rate constant, and the populations of the involved states. Of note, only fluctuation of both chemical shifts lead to differential relaxation (i.e. fluctuation of only one chemical shift does not lead to differential relaxation). The sign of ΔR_{MQ} depends on the relative signs of the chemical-shift fluctuations of the two nuclei. This can be readily seen from Eq. (51). Finally, panel (d) shows the general case, in which a dynamic process alters both the isotropic and anisotropic chemical shifts.

In summary, correlated fluctuation of isotropic and anisotropic chemical shifts can be detected through the different relaxation behavior of ZQ and DQ coherences. A MAS dependence of ΔR_{MQ} arises if the differential relaxation is due to CSA fluctuations, and if the motion is on the "slow branch", i.e., in the microsecond to millisecond time scale. The quantitative measurement of differential relaxation relies on the assumption that coherent contributions impact both the ZQ and DQ relaxation to similar extent. Differential ZQ/DQ relaxation has been studied recently using highly deuterated ubiquitin in the solid state [44].

3.3.3 Relaxation in the Presence of a Spin-Lock Field: $T_{1\varrho}$ Measurements—As outlined above, the challenge of accessing quantitative transverse relaxation parameters is separation of incoherent relaxation effects due to stochastic processes from signal decay that arises from coherent evolution under incompletely averaged anisotropic interactions. The observables introduced in the previous sections circumvent this problem by measuring the difference between two decay parameters assuming that the coherent dephasing contributes similarly to both quantities.

Alternatively, one may identify conditions where the coherent contributions to a particular transverse relaxation-rate constant are sufficiently suppressed, such that they become negligible compared to the incoherent part. As coherent dephasing is due to incomplete averaging of anisotropic interactions, in the sense of second- or higher-order terms in the average-Hamiltonian expansion (see Section 3.1), this contribution is reduced by (i) eliminating some of the interactions (e.g., by deuteration) and/or (ii) by increasing the MAS frequency. As discussed in Section 3.3.1 (Figure 14) even combining high levels of deuteration and the fastest MAS frequencies available today is insufficient to suppress coherent contributions to R_2' rate constants. However, this may not be the case for relaxation under a spin-lock, i.e., $R_{1\varrho}$.

Lewandowski *et al* have shown that the coherent contributions are strongly reduced when measuring ^{15}N $T_{1\varrho}$ time constants, i.e., the decay of ^{15}N coherence in the presence of a spin-lock field at MAS frequencies of 40 kHz or higher [114]. It was estimated that the coherent dephasing contribution to ^{15}N $R_{1\varrho}$ rate constants are smaller than approximately 0.27 s^{-1} in protonated proteins at MAS frequencies exceeding 40 kHz. Thus, it becomes negligible compared to the actual ^{15}N $R_{1\varrho}$ relaxation-rate constants, which are typically in the order of >2 s^{-1} for the backbone amides of proteins. The coherent dephasing is reduced significantly by the presence of a spin-lock field, compared to free evolution and proton decoupling. This effect is not yet fully understood or explained.

Prior to the study of Lewandowski *et al* mentioned above, there have also been reports of measurements of ^{15}N $R_{1\varrho}$ relaxation-rate constants in highly-deuterated proteins at lower MAS frequency of about 10-20 kHz [113], and over the last years several other studies of $R_{1\varrho}$ rate constants have been reported under different conditions of sample deuteration, MAS frequency, and RF-field strengths [45,100,110,133,134]. The conditions under which coherent dephasing is sufficiently suppressed depends on the choice of the labeling scheme (in particular deuteration), the MAS frequency, and the RF field strength. The precise ranges of these three parameters that allow one to neglect coherent dephasing are not yet entirely clear, and need further experimental investigation.

For a quantitative description of the $T_{1\varrho}$ experiment we need to consider three time-dependent processes, (i) MAS, (ii) the RF-field amplitude of the spin lock and (iii) the stochastic process, which modulates the anisotropic interactions and leads to relaxation. In addition, we also need to consider that the dynamic process is sensitive to differences in the isotropic chemical shifts. We defer the latter effect to a paragraph later in this section.

The analytical equation describing $T_{1\varrho}$ relaxation of a spin due to the CSA and the heteronuclear dipolar coupling are given by

$$\frac{1}{T_{1\rho}(\Omega)} = R_{1\rho}(\Omega) = \cos^2(\theta_{\text{eff}})\frac{1}{T_1} + \sin^2(\theta_{\text{eff}})\frac{1}{T_{1\rho}(0)} \quad (52)$$

where the magnitude of the effective field $\omega_{\text{eff}} = \left(\omega_1^2 + \Omega^2\right)^{1/2}$ and the direction of the effective field are given by $\theta_{\text{eff}} = \arccos(\Omega/\omega_{\text{eff}})$. The analytical expression for T_1 can be found in Eq. (37) while the analytical expression for the on-resonance $T_{1\varrho}$ ($T_{1\rho}(0)$) is equivalent to the T_2 expression of Eq. (46) with the zero frequency replaced by the effective field strength. It is important to remember (see Section 2.2.1) that the frequencies sampled by the spectral-density functions have to be adjusted and corrected for the RF-field amplitude. These expressions can be written in a more compact way following Ref. [135]:

$$\frac{1}{T_{1\rho}} = R_{1\rho} = R_1 + \sin^2\theta_{\text{eff}}\left(R_{1\Delta} - \frac{1}{2}R_1\right) \quad (53)$$

where

$$R_{1\Delta} = \left(\frac{\delta_D}{4}\right)^2 \left(3J(\omega_s) + \frac{1}{3}J(\omega_{\text{eff}} - 2\omega_{\text{r}}) + \frac{2}{3}J(\omega_{\text{eff}} - \omega_{\text{r}}) + \frac{2}{3}J(\omega_{\text{eff}} - \omega_{\text{r}}) + \frac{1}{3}J(\omega_{\text{eff}} - 2\omega_{\text{r}})\right) + \delta_{CSA}^2 \left(\frac{1}{3}J(\omega_{\text{eff}} - 2\omega_{\text{r}}) + \frac{2}{3}J(\omega_{\text{eff}} - \omega_{\text{r}}) + \frac{2}{3}J(\omega_{\text{eff}} + \omega_{\text{r}}) + \frac{1}{3}J(\omega_{\text{eff}} + 2\omega_{\text{r}})\right) \quad (54)$$

Here, we have already made the assumption that the Larmor frequencies are much larger than the effective field and the MAS frequency, and that both are only considered for their contributions to the $J(0)$ term of T_2 relaxation. The term $R_{1\Delta}$ is sensitive to the spectral-density function at frequencies corresponding to sums and differences of the RF-field strength and MAS frequency. Thus, $R_{1\varrho}$ relaxation-rate constants depend on the MAS frequency and the rf-field amplitude. Note that such a MAS dependence is not seen for longitudinal relaxation-rate constants, because the relevant spectral densities are the sums and differences of the MAS frequency (tens of kilohertz) and the Larmor frequency (hundreds of megahertz). As the Larmor frequency is much larger than the MAS frequency, these terms are essentially independent of the MAS frequency. It should also be noted here, that the $T_{1\varrho}$ relaxation for homonuclear dipolar couplings has a different form and samples

the spectral-density function at different frequencies. An alternative formulation of the expression for $T_{1\varrho}$ under MAS has been reported [136].

Figure 19 shows calculated $R_{1\varrho}$ rate constants for a fixed MAS frequency and three different spin-lock RF field strengths. These simulations indicate that for RF-field amplitudes approaching the MAS frequency, the $R_{1\varrho}$ rate constant increases if the motion is in the microsecond regime, while for correlation times in the nanosecond time scale $R_{1\varrho}$ rate constants are unaltered. This dependence on the MAS frequency and RF-field strength comes from the spectral density terms sampling sums and differences of MAS frequency and rf-field amplitude (see Eq. (54)). It is similar to the MAS dependence of the cross-correlated relaxation rate constants discussed above (see Figure 17 and Figure 18). The dependence of the $R_{1\varrho}$ rate constant on MAS frequency and RF field strength has been exploited previously to study microsecond motion [45,133,137].

It is noteworthy that the three transverse relaxation parameters we have considered so far (CSA/D cross-correlated relaxation, CSA/CSA cross-correlated relaxation and $R_{1\varrho}$ relaxation) are all sensitive to similar frequencies of the spectral density, although there are some differences. This becomes evident when comparing Figure 17 and Figure 19. It is interesting to compare how for a given sample the measured relaxation-rate constants compare, given that they should in principle have some similarity. Figure 20 shows a comparison between two different rate constants measured on ubiquitin. Although there are differences, which might be due to the somewhat different sensitivity to the spectral density function, it is evident that the two measurements provide a similar picture of the motion in this protein.

We have so far only considered $R_{1\varrho}$ relaxation due to stochastic modulation of anisotropic interactions. In this last paragraph we consider the effect of isotropic chemical-shift fluctuations on $R_{1\varrho}$ relaxation-rate constants. The isotropic chemical-shift modulation is the basis of solution-state experiments that address conformational exchange processes on microsecond-to-millisecond time scales. In (isotropic) solution, the isotropic chemical-shift fluctuation is the only way of accessing dynamics on time scales longer than the overall tumbling correlation time (typically tens of nanoseconds). The effects of chemical-shift modulation in solution-state NMR are well described by the Bloch-McConnell formalism [138]. We use here numerical simulations to investigate common features as well as differences between the well-known solution-state case and the situation under MAS. Figure 21 shows the $R_{1\varrho}$ relaxation rate constant of a ^{15}N spin bound to a ^{1}H spin, which undergoes exchange between two states. In these simulations we assume that the two states differ by the orientations of the ^{1}H-^{15}N dipolar coupling and the ^{15}N CSA tensor, or by the isotropic ^{15}N chemical shift, or both. We first consider the case where the two states differ only by the isotropic chemical shift, while all anisotropic interactions remain unchanged by the dynamic process (Figure 21, solid black curve). In this case the heteronuclear dipolar coupling and CSA are perfectly averaged by MAS, and the situation is identical to the one in solution-state NMR. We observe an amplitude-dependent $R_{1\varrho}$ relaxation-rate constant (relaxation dispersion) in the low rf-field range that is due to the isotropic chemical-shift modulation fully described by the Bloch-McConnell formalism. The relaxation-dispersion

profile depends on (i) the relative populations of the involved states, (ii) the exchange kinetics, and (iii) the isotropic chemical-shift difference.

In the case where the two exchanging states differ also in the orientations of dipolar-coupling and CSA tensors, the situation becomes more complex: as the RF-field amplitude approaches the rotary-resonance conditions [139,140] ($\nu_1 = n\,\nu_r$ where $n = 1,2$), we observe an increased $R_{1\varrho}$ decay-rate constant [45,133,134]. This is expected, as the spectral density at the difference between MAS frequency and the RF-field amplitude is relevant for $R_{1\varrho}$ (see Eq. (54)). In the context of our exchange model, the shape of this relaxation-dispersion profile depends on (i) the populations of the involved states, (ii) the exchange kinetics and (iii) the strength of the involved interactions and the angle by which they are modulated along the exchange process. Note that in solution-state NMR overall tumbling averages anisotropic interactions to zero on a nanosecond time scale. Thus, microsecond fluctuations of bond orientations in isotropic solution are undetectable by solution-state NMR. This is not the case for liquid-crystalline solution and it has been shown that bond-vector orientation changes can be detected in such systems [141]. In the general case, both isotropic chemical-shift changes as well as bond-vector orientation changes are expected to occur in any motional process. The expected evolution of $R_{1\varrho}$ with the RF-field amplitude is thus the sum of the two limiting cases, a Bloch-McConnell-type of dispersion, and a dispersion in the vicinity of the rotary-resonance conditions. Solid-state $R_{1\varrho}$ relaxation-dispersion experiments have been shown to probe isotropic chemical-shift changes and bond-vector changes in proteins [45].

$T_{1\varrho}$ experiments in proteins have so far primarily been used with ^{15}N spins. The reasons for focusing on this nucleus is that its relaxation is well described by taking into account only the ^{15}N CSA tensor and the heteronuclear dipolar interaction to the directly-bonded proton. The case of ^{13}C $T_{1\varrho}$ relaxation in fully ^{13}C labeled proteins is more complicated. The evolution of homonuclear dipolar and scalar couplings during the spin-lock period renders quantitative analyses more difficult. Similar challenges have been addressed in solution-state NMR [2,142]. The solutions primarily involve selective labeling schemes or a restriction to the carbonyl ^{13}C nucleus. Since it is well-separated from other ^{13}C spins in terms of resonance frequency, the application of selective RF irradiation is straightforward. The stronger ^{1}H-^{13}C dipolar coupling also means that the second-order AHT term (Eq. (31)) is larger. Thus, it is more difficult to suppress coherent dephasing for the case of ^{13}C transverse relaxation, as compared to ^{15}N relaxation.

3.3.4 Carr-Purcell-Meiboom-Gill (CPMG) Relaxation Dispersion—We have seen in the previous section that fluctuation of the isotropic chemical shift leads to increased $R_{1\varrho}$ rate constants. Likewise, such fluctuations also lead to increased R_2' relaxation, i.e., enhanced coherence decay in a spin-echo experiment. This can be seen by considering the evolution of a spin in a spin-echo sequence. In the absence of conformational exchange, the spin accumulates a phase during the first delay τ, according to its chemical shift; the refocusing pulse and subsequent delay refocus this accumulated phase, resulting in full echo formation. In the presence of stochastic exchange of the molecule between two (or more) conformations, the phase that a spin accumulates depends on the time the molecule spends in each of the states, and their respective chemical shifts. As the exchange process is

stochastic, the trajectory that the molecule undergoes during each of the two delays differ, and therefore the phase accumulated during the first delay differs from the one in the second delay, such that the echo formed at the end of the second delay is incomplete. When considering the ensemble of molecules we study, each undergoing different stochastic exchange, the result is an increased apparent R_2' rate constant. This exchange-broadening can be reduced if the delays are reduced (such that the accumulated phase is smaller, which can be done by applying a train of closely-spaced refocusing pulses instead of a single refocusing pulse. This idea is at the basis of what is known as Carr-Purcell-Meiboom-Gill relaxation dispersion (RD) experiments [73,74]. Figure 22a shows the principle of such experiments; the coherence decay is measured in different experiments, where the repetition rate of the refocusing pulses is changed. In the presence of exchange the effective relaxation-rate constant varies with the CPMG frequency (Figure 22c), ($\nu_{CPMG} = 1/(4\tau)$) in a manner that depends on (i) the isotropic chemical-shift difference of the considered nucleus in the exchanging states, (ii) the exchange-rate constant and (iii) the relative populations of the exchanging states. Therefore, fitting CPMG RD profiles allows us to obtain these parameters, similarly to $R_{1\varrho}$ relaxation dispersion experiments [2,40,42].

In order to allow a quantitative analysis of the exchange process, one needs to assure that the dependence of the relaxation-rate constant on the CPMG frequency is solely due to exchange. This is not always the case, and eliminating or quantifying other contributions is one of the main challenges in CPMG experiments. For example, during the free-evolution delays, an initial in-phase operator N_x evolves under the scalar coupling to anti-phase $2H_zN_y$; although the subsequent π pulse and the delay will refocus this term, the effective relaxation rate is the weighted average of the relaxation rates of N_x and $2H_zN_y$, and the relative weight of these two coherences depends on the length of the delay. The relaxation of in-phase and anti-phase magnetization is generally different, and consequently, in experiments with different delays (i.e., CPMG frequencies) the relaxation rate is expected to differ *even without* the presence of conformational exchange. This hampers quantitative analysis of CPMG dispersion data. In solution-state NMR this issue has been solved either by ensuring that the time during which N_x and $2H_zN_y$ are present is constant and independent of the CPMG frequency [143], or by preventing the buildup of the anti-phase term by scalar decoupling. Using either implementation leads to CPMG RD measurements that are robust and reliable. In practice, such experiments are most often performed using a constant-time delay, while applying an increasing number of refocusing pulses (see Figure 22a). The CPMG frequency is then $\nu = n / (2T)$, where n is the number of applied pulses and T is the total relaxation delay.

In the solid state, the coherence decay in a spin-echo experiment (R_2') contains also contributions from dipolar dephasing, and the decay rate constant itself is not amenable to quantitative interpretation. However, in the context of studies of conformational exchange the absolute values of the R_2' rate constants are not relevant, and in solution-state NMR the "plateau" value of R_2' (at infinite ν_{CPMG}) is independent of conformational exchange and is usually not further interpreted. Thus, CPMG RD experiments may be applied to MAS NMR even though the R_2' rate constants contain coherent dephasing. However, in order to apply and quantitatively interpret CPMG RD data in MAS NMR a number of conditions need to be verified. (i) It must be assured that the coherent contributions to R_2' are independent of

ν_{CPMG} or that the dependence is precisely known. This basically means that the dipolar dephasing should be independent of ν_{CPMG} and that recoupling of anisotropic interactions by the train of π pulses can be excluded. (ii) From a practical perspective, the relaxation-rate constant should be sufficiently small such that a long total relaxation delay can be chosen. This is because the minimum CPMG frequency depends on the relaxation delay as $\nu_{min} = 1/(2T)$. Note that the duration of the pulses is generally short compared to the inter-pulse delay, and the relaxation during the pulses is generally neglected.

Figure 22(c)-(f) investigates the properties of ^{15}N CPMG RD experiments under MAS, using the pulse-sequence element in panel (b). In the first case we investigate an exchange process in a H-N two-spin system with two states that differ only by the isotropic ^{15}N chemical shift, while the orientations and anisotropies of the CSA and dipolar-coupling tensors are fixed. In this case MAS perfectly averages the static anisotropic interactions and the RD profile can be predicted using the Bloch-McConnell formalism (Figure 22c). In the case where the exchange process also alters the anisotropic interactions, the R_2' rate constants are increased (Figure 22d, e). This is expected, as fluctuation of CSA and dipolar-coupling tensors leads to relaxation (see Figure 14).

Additional protons render the situation somewhat more complex, as shown in panels (d) to (f). The presence of an additional proton spin increases the apparent R_2' relaxation rate constant. If this increase is uniform, i.e. independent of the CPMG frequency, such an increase does not have any effect of fitted exchange parameters. The increase is indeed only slightly ν_{CPMG}-dependent in the simulations, although the remaining coherent contributions may generally lead to inaccuracies. Numerical simulations (such as those shown in panel (f)) can be used to quantitatively investigate the impact of these contributions to the fitted parameters [44].

CPMG relaxation-dispersion MAS NMR has been used only recently, in an application to microcrystalline ubiquitin [44]. In this study, a highly deuterated protein sample was used, in order to reduce the effects of remote proton spins and increase ^{15}N coherence life times. Data were obtained at two different static magnetic field strengths, and fit using the Bloch-McConnell formalism as usually applied in solution-state NMR. By comparison with relaxation-dispersion measurements in solution state, it was found that the motions are slowed down by the crystalline environment (see Section 4).

3.3.5 The Validity of Redfield Theory in Solids—The discussion so far has mostly been based on the Redfield treatment of relaxation. As outlined in Section 2.1, an important assumption in the derivation of Redfield theory is that the motional process is very fast compared to the change of the density operator. For the motion on a microsecond time scale that we study with transverse relaxation-rate constants, this assumption is not *a priori* granted. It is, therefore, important to compare numerical simulations based on the stochastic Liouville approach [69-71] for the transverse relaxation-rate constants discussed (cross-correlated relaxation and $T_{1\varrho}$ relaxation), with their analytical results based on Redfield theory.

Figure 23 compares ^{15}N $R_{1\varrho}$ rate constants calculated with the analytical Redfield treatment (Figure 23a) and rate constants obtained by stochastic numerical simulations in the rotating frame (Figure 23b). For both simulations we assumed an identical two-site exchange model, similar to the simulations shown in Section 2.2.2. The comparison shows that on the “fast branch”, i.e. when the correlation time is 10^{-8} to 10^{-6} s, the two approaches result in essentially identical ^{15}N $R_{1\varrho}$ rate constants. For faster motions, there are significant differences that are due to the fact that the stochastic simulations are carried out in the rotating frame. As soon as the correlation times approach the magnitude of the inverse of the Larmor frequencies, this approach is no longer correct. Essentially, the spectral densities at multiples of the Larmor frequencies are not sampled by the stochastic Liouville simulation in the rotating frame. For slower motion (10^{-6} to $10^{-2.5}$ s), there is a clear difference between the two approaches with the Redfield method based data being larger. The source of this discrepancy is an interference between the stochastic time-dependent process and the MAS rotation, which are on the same time scale. For even longer correlation times, the agreement gets better again since the time scales of the deterministic and stochastic time dependence get separated again. Although the deviation is small, quantitative analyses of dynamics in this time regime need to take this into account.

Similar differences are found in comparisons of the CSA/D (Figure 24) and CSA/CSA (Figure 25) cross-correlated relaxation rate constants. Figure 26 shows a comparison of two slices for order parameters of 0.982 and 0.95, which illustrates again the differences between the Redfield and the stochastic Liouville approach.

These illustrations show that the relaxation-rate constants predicted by Redfield theory are generally incorrect in the microsecond to millisecond regime. This is expected from the assumptions made in the derivation of Redfield theory. We have not considered here relaxation in the presence of heteronuclear decoupling, which are sometimes used in protonated proteins. Approximate solutions to such experiments have been proposed [76,109].

Taken together, in this section we have presented transverse relaxation parameters and their dependence on dynamics, and also their sensitivity to factors that are unrelated to dynamics (in particular dipolar dephasing). Under experimental conditions reported so far, free-evolution decay rate constants (R_2) cannot be quantitatively analyzed, as the coherent contribution to decay is often dominant. We have presented three experimental parameters that are sensitive to dipolar and/or CSA fluctuations, and which can be quantitatively measured, namely CSA/D cross-correlated relaxation, CSA/CSA cross-correlated relaxation and $R_{1\varrho}$ relaxation. These relaxation rate constants are sensitive to the spectral density function at the MAS frequency (and, for $R_{1\varrho}$, the RF field strength). In the “slow end” of the sensitivity range of these parameters (microseconds), these relaxation rate constants are thus sensitive to the MAS frequency, and MAS-dependent measurements, or RF-field dependent measurements of $R_{1\varrho}$ can provide direct evidence for such slow motions. We also showed that isotropic chemical-shift fluctuations can be probed by $R_{1\varrho}$- or CPMG relaxation dispersion, or via the differential relaxation of ZQ and DQ coherences. Section 3.5 will investigate how transverse and longitudinal relaxation rate constants, together with the

amplitudes of motion obtained from dipolar-coupling derived order parameters (Section 3.4) can inform about physical parameters of the dynamics.

3.4 Direct Measurement of Motional Amplitudes from Incompletely-Averaged Anisotropic Interactions

Fluctuation of NMR interactions, in particular dipolar couplings, chemical-shift anisotropies, and quadrupolar couplings (only for spins with quantum numbers $I > 1/2$) lead to nuclear spin relaxation. The induced relaxation-rate constants depend on the strengths of the interactions, the amplitude of motion, and the time scale at which the fluctuation occurs, as discussed in the previous sections. In addition, the incomplete averaging of these interactions due to dynamics in solids provides another, complementary probe of molecular dynamics. Unlike relaxation, the averaged values of the anisotropic interactions do not explicitly depend on the time scale of motion. In this section we will discuss how motional processes lead to incomplete averaging of anisotropic interactions, and how information about the motional amplitude and their symmetry can be obtained from measurements of scaled anisotropic interactions.

The NMR interactions can be described by a Hamiltonian, which in the case of an interaction between two spins ($k \neq n$) has the following form in Cartesian notation:

$$\hat{\mathscr{H}} = \vec{\hat{I}}_k \cdot A^{(k,n)} \cdot \vec{\hat{I}}_n = \begin{pmatrix} \hat{I}_{kx} & \hat{I}_{ky} & \hat{I}_{kz} \end{pmatrix} \begin{pmatrix} a_{xx} & a_{xy} & a_{xz} \\ a_{yx} & a_{yy} & a_{yz} \\ a_{zx} & a_{zy} & a_{zz} \end{pmatrix} \begin{pmatrix} \hat{I}_{nx} \\ \hat{I}_{ny} \\ \hat{I}_{nz} \end{pmatrix} \quad (55)$$

Such a Hamiltonian describes the interaction between two (nuclear or electron) spins, such as the scalar, the dipolar, or the hyperfine coupling. The quadrupolar coupling is described by the same type of Hamiltonian with $k = n$. The interaction of a spin with a classical magnetic field (Zeeman interaction, radio-frequency fields, chemical shift, or magnetic susceptibility) is described by a Hamiltonian, which has a similar form

$$\hat{\mathscr{H}} = \vec{\hat{I}}_k \cdot A^{(k,B)} \cdot \vec{B} = \begin{pmatrix} \hat{I}_{kx} & \hat{I}_{ky} & \hat{I}_{kz} \end{pmatrix} \begin{pmatrix} a_{xx} & a_{xy} & a_{xz} \\ a_{yx} & a_{yy} & a_{yz} \\ a_{zx} & a_{zy} & a_{zz} \end{pmatrix} \begin{pmatrix} B_x \\ B_y \\ B_z \end{pmatrix} \quad (56)$$

In all cases of NMR interactions, the matrix A describes the strength and orientation-dependence of the interaction. It is often convenient to decompose the general 3×3 matrix in three components,

$$A = A^{(0)} + A^{(1)} + A^{(2)} \quad (57)$$

where

Europe PMC Funders Author Manuscripts

Europe PMC Funders Author Manuscripts

$$A^{(0)}=\begin{pmatrix}\overline{a} & 0 & 0\\ 0 & \overline{a} & 0\\ 0 & 0 & \overline{a}\end{pmatrix} \quad (58)$$

with

$$\overline{a}=\frac{1}{3}Tr\,(A)=\frac{a_{xx}+a_{yy}+a_{zz}}{3} \quad (59)$$

This component is invariant under rotation, i.e., isotropic, and is referred to as rank-0 component of A. In the case of the chemical-shift interaction, this component is referred to as the isotropic chemical shift while in the case of the J coupling, it is referred to as the scalar coupling. For dipolar and quadrupolar coupling this component does not exist.

The traceless and symmetrized part of A, the component $A^{(2)}$, is given by

$$A^{(2)}=\begin{pmatrix}a_{xx}-\overline{a} & \frac{a_{xy}+a_{yx}}{2} & \frac{a_{xz}+a_{zx}}{2}\\ \frac{a_{xy}+a_{yx}}{2} & a_{yy}-\overline{a} & \frac{a_{yz}+a_{zy}}{2}\\ \frac{a_{xz}+a_{zx}}{2} & \frac{a_{yz}+a_{zy}}{2} & a_{zz}-\overline{a}\end{pmatrix} \quad (60)$$

and has the rotation properties of a rank-2 tensor. In the present section we focus on this component of the interaction tensors in particular for the cases of the chemical-shift, the dipolar and the quadrupolar interactions. The remaining component, $A^{(1)}$, is traceless and antisymmetric. It has rank-1 tensor properties, and it is usually not discussed in NMR since it is not visible in high-field NMR spectra. However, it can contribute to relaxation phenomena and while it has been measured in selected cases [144], its magnitude is often not known and it is difficult to quantify its contribution.

The Cartesian rank-2 tensor is diagonal in the principal-axis system of the interaction:

$$A=\begin{pmatrix}A_{xx} & 0 & 0\\ 0 & A_{yy} & 0\\ 0 & 0 & A_{zz}\end{pmatrix}=\delta_{\mathrm{A}}\frac{1}{2}\begin{pmatrix}-1-\eta_{\mathrm{A}} & 0 & 0\\ 0 & -1+\eta_{\mathrm{A}} & 0\\ 0 & 0 & 2\end{pmatrix}. \quad (61)$$

Here, A_{xx}, A_{yy} and A_{zz} are the diagonal elements of the tensor A in the principal axis system and δ_{A} is the anisotropy and $\eta_A = (A_{yy} - A_{xx}) / A_{zz}$ is the asymmetry of the interaction. The asymmetry assumes values $0 \le \eta_A \le 1$, implying that $|A_{yy}| \le |A_{xx}| \le |A_{zz}|$. These definitions follow the conventions proposed by Mehring [55].

In the case of a dipolar coupling, i.e. the direct through-space interaction between two spins n and k, the magnitude of the anisotropy is determined by the nature of the involved nuclei and their relative distance, i.e.,

$$\delta_{\mathrm{D}} = -2\frac{\mu_0}{4\pi}\frac{\gamma_k\gamma_n\hbar}{r_{nk}^3}. \quad (62)$$

The magnitude of the dipolar coupling depends only on the distance between the two spins and is axially symmetric, i.e., $\eta_{\mathrm{D}} = 0$. The dipolar coupling is, therefore, described by an axially-symmetric tensor and is traceless, i.e., it is averaged to zero in isotropic solution. The anisotropy of the dipolar coupling tensor, δ_{D}, is unambiguously defined by Eq. (62), and we will use this definition throughout. For a ^{1}H-^{15}N spin pair separated by 1.02 Å, the tensor anisotropy is $\delta_{\mathrm{D}}/2\pi$ = 22.954 kHz. Sometimes the term dipolar-coupling constant is used, which corresponds to the splitting observed in a static powder spectrum, which is for a heteronuclear spin pair $\delta_{\mathrm{D}}/4\pi$.

As already discussed in the Introduction, the J coupling has, in principle, all three components (rank-0, rank-1 and rank-2 tensor components). However, the rank-2 part of the dipolar coupling is typically small for light elements and for practical purposes absorbed into the dipolar coupling. There is not much information available about the antisymmetric part of the J coupling and usually only the isotropic part of the J coupling is considered in the form of the scalar coupling.

The quadrupolar coupling exists only for spins with $I > 1/2$, such as deuterium. It arises from the interaction of the quadrupole moment of the spin (Q) with the electric field gradient. The source of the electric field gradient is the non-spherical distribution of the electron density around the nucleus. The anisotropy of the quadrupolar-coupling tensor is

$$\delta_{\mathrm{Q}} = \frac{e^2qQ}{2I\,(2I-1)\,\hbar} \quad (63).$$

Unlike the dipolar-coupling tensor, quadrupolar-coupling tensors are generally not axially symmetric, i.e. $\eta \neq 0$. The electric-field gradient tensor is traceless, implying that in solution the nuclear quadrupole interaction has an average of zero and, therefore, no isotropic component.

The chemical shift is due to the magnetic field induced by the electrons surrounding a nucleus. Unlike the dipolar and quadrupolar coupling interactions, the rank-0 component of the chemical-shift tensor does not vanish, i.e. the chemical-shift tensor has a non-zero isotropic average. Fluctuation of this isotropic component is not the focus of this section; we recall here that we have discussed in Section 1 the cases of fast/slow exchange with respect to the isotropic chemical shift, and in Section 3.3 we investigated how isotropic chemical-shift fluctuation on a time scale commensurate with the magnitude (in Hertz) of the fluctuation leads to line broadening, and how it can be measured by CPMG relaxation dispersion, $R_{1\varrho}$ relaxation dispersion, or differential ZQ/DQ relaxation.

The rank-2 component is referred to as chemical-shift anisotropy (CSA). It is generally asymmetric, i.e. $\eta_{\mathrm{CSA}} \neq 0$. For certain sites, such as the backbone ^{15}N spin, it can be

approximated well by an axially-symmetric tensor, i.e., $\eta_{CSA} = 0$. Determining CSA tensors from *ab initio* quantum-chemical calculations currently remains challenging [145]. This means that the rigid-limit CSA tensors are generally not known to high precision, making it difficult to interpret measured CSA parameters in terms of dynamics.

It is instructive to visualize the rank-2 tensors in terms of graphical representations, to get an intuitive understanding for the motional averaging of anisotropic interactions. Figure 27a shows such representations for a symmetric second-rank tensor (i.e. $\eta = 0$), such as a dipolar-coupling tensor or an axially symmetric CSA tensor. The anisotropic nature of this interaction is readily visible because the function along different spatial directions takes different values. This space-dependence is described by the second-order Legendre polynomial $P_2(\cos\theta) = (3\cos^2\theta - 1)/2$, where θ is the angle between the z axis of the tensor (i.e., the internuclear vector for a dipolar interaction) and the static magnetic field B_0. In the representation of Figure 27, cyan portions correspond to orientations in which the value of the interaction (e.g. the dipolar coupling) is positive, whereas red portions correspond to orientations with a negative values of the interaction. In Figure 27a the internuclear vector would thus point along the vertical axis. If we assume that the B_0 field is along the same axis, the spin pair would have a large and positive dipolar coupling.

When motion is present, different states are inter-converting, and these states generally differ in terms of the orientation of the interaction and possibly the magnitude of the tensor anisotropy δ_D, but we neglect this here for simplicity. For example, consider the dipolar coupling between two spins, which would only change in terms of its orientation. If the inter-conversion between these states is fast compared to the interaction strength – we will illustrate the time scale considerations further below – the resulting measurable interaction tensor corresponds to the average over all sampled orientations. Figure 27B shows this averaging process for the case of the dipolar-coupling tensor of a system undergoing a two-site exchange process. The plot shows the resulting tensor of the averaging process for a range of different relative populations between the two states which differ by an angle of 90°. Figure 27C shows the tensors resulting from dynamic averaging in a three-site exchange process. One can see in this example that if only one state is populated, i.e., in the absence of motion (the tensors in the corners of the triangle), the dipolar-coupling tensor is axially symmetric and corresponds to the rigid-limit value. Whenever there is dynamic averaging between different conformers, the anisotropy of the averaged tensor will be smaller than the static value. Furthermore, in the general case the averaged tensor will become asymmetric, even though each of the rigid-limit tensors is axially symmetric.

Such a simple graphical representation of the dynamic averaging process indicates that the averaged interaction tensors directly report on the amplitude of the underlying motion. Thus, if one can measure experimentally the averaged tensor, and if one knows the anisotropy and asymmetry of the tensors in the static case, one can get direct insight into the amplitude of the motion underlying the averaging process. Often only the anisotropy of the interaction is quantified, as it is generally easier to measure, and the reduction of the tensor anisotropy is reported as the order parameter S,

$$S=\delta_{\mathrm{exp}}/\delta_{\mathrm{rigid}}. \quad (64)$$

Note that the order parameter S is obtained here, not S^2, which is obtained from relaxation measurements; this is because a product of interactions enters in the relaxation equations, and the scaling of the interactions thus enters as a product (see Eq. (23)). Measuring motional amplitudes through motionally-averaged anisotropic interactions, therefore, requires (i) that the interaction tensor can be measured with a high accuracy and precision and (ii) that the rigid-limit values of the tensors are known. In this context, the dipolar coupling between directly bonded nuclei is particularly attractive, because the rigid-limit dipolar-coupling tensor can be readily computed from the vibrationally-averaged bond length, and the gyromagnetic ratios of the involved nuclei. However, also CSA and quadrupolar tensors can provide rich information about motional amplitudes.

Measurements of anisotropic interactions under MAS can be done with different approaches. If the magic-angle spinning frequency is small compared to the magnitude of the anisotropy of the interaction, the spinning side-band manifold can be used to characterize the anisotropic interaction tensor directly. This is mainly the case for quadrupolar couplings which are often much larger than typical spinning frequencies. For dipolar-coupling and CSA interactions, measuring anisotropic interactions under MAS often requires a recoupling sequence [77-80], which reintroduces the interaction that is otherwise averaged by MAS in first order on the time scale of τ_r. The recoupling can be seen as an interference between two time-dependent processes, the sample rotation and the pulse sequence. If molecular motion is present, this stochastic dynamic process is a third time dependence; it leads to an averaging of the anisotropic interactions (which is the desired information), and it may also interfere with the MAS averaging and the recoupling sequences. We investigate in the following the effect of dynamics on the apparent recoupling behavior one can observe. This is best done using numerical simulations (performed here with GAMMA [146]), which take into account (i) magic-angle sample spinning, (ii) a recoupling sequence, and (iii) a dynamic process, here modeled as a jump between discrete sites. Interferences between these three different processes are used to illustrate the time scales over which dynamic averaging occurs. For these simulations, a widely used heteronuclear dipolar-recoupling technique, the Rotational Echo DOuble Resonance (REDOR) recoupling sequence is used [147]. In REDOR, a train of rotor-synchronized π pulses is applied twice per rotor period, in order to counteract the averaging of the dipolar coupling by MAS. The outcome of this experiment is a (normalized) signal amplitude which is modulated over the course of a recoupling period with a frequency that reflects the tensor anisotropy and to some extent also the tensor asymmetry, as shown further below. In our simulations, the MAS and the inversion pulses, as well as the dynamic process are explicitly taken into account; the dynamics are modeled using an explicit two- and three-site jump model, similar to the numerical simulations in the previous sections about relaxation.

Figure 28 shows REDOR curves for a system undergoing a symmetric three-site exchange process, occurring on a range of time scales from 10 ns to 1 s. In the case that the exchange process is very slow (top left panel) the REDOR oscillation is fast, reflecting a large tensor

Europe PMC Funders Author Manuscripts

anisotropy (i.e. a strong dipolar coupling). This large and non-averaged dipolar coupling is expected for slow dynamics, because in the limiting case of infinitely slow motion the system behaves like a fully rigid system with the full (symmetric) dipolar coupling. On the other end of the time scale, if the motion is very fast, the resulting REDOR oscillation is slow. As the motional model used here is a symmetric three-site jump model ($\theta = 70.5°$, $\varphi = 120°$) with equal populations, the scaling of the dipolar coupling is a factor $P_2(\cos\theta) = -1/3$ in the fast-exchange limit, and the time evolution is thus simply scaled by a factor of 1/3 as compared to the rigid-limit case. In between these two limiting cases, fast and slow motion, one can see a transition area. Figure 28 shows that this “coalescence” regime occurs when the rate of the dynamic process is about $k = 100\ s^{-1}$ to $5000\ s^{-1}$. In this “transition” regime, the REDOR curve appears “damped”. The range of rate constants at which this intermediate regime is reached directly depends on the interaction strength, as well as some pulse-sequence related factors that translate into a “scaling factor” of the interaction measured by the sequence [148,149]. Thus, for a smaller interaction strength the interaction is averaged up to longer time scales. Experimental approaches to characterizing this intermediate regime have been discussed [150,151].

Note that the averaging process of anisotropic interactions revealed by Figure 28 is analogous to the averaging of isotropic chemical shifts, which is a more widely known phenomenon in NMR: the separation between “fast exchange”, characterized by the observation of a single averaged chemical-shift value and “slow exchange”, in which case individual peaks for the involved states are observed, depends on the chemical-shift difference. Fast exchange is defined as $k \gg \Delta\Omega$, while for slow exchange $k \ll \Delta\Omega$, and in the intermediate regime line broadening is observed. Similarly, the REDOR curves in the slow exchange regime can be seen as a superposition of individual REDOR recoupling curves. In our examples, the different exchanging states were assumed to have identical (rigid-limit) tensor parameters; thus a single recoupling behavior is observed. In the “fast exchange” regime, one also sees a single recoupling curve, which represents the averaged dipolar coupling tensor. These findings are thus analogous to chemical-shift averaging. The situation is complicated by the fact that in a powder sample different crystallites have different values of the dipolar coupling. Therefore, we see a superposition of curves where different crystallites can be in different exchange regimes.

In the above example we have studied the case of a three-fold symmetric exchange process with equal populations. In such a case of C_3 symmetry (or in cases of higher symmetry) and equal populations the resulting averaged tensor is itself axially symmetric, just as the rigid-limit tensors are axially symmetric. We now consider the more general case of a lower symmetry. Figure 29 shows the case of a two-site jump model. Similar to the case described above, we find fast, intermediate and slow exchange regimes, but in the fast-exchange limit we get a recoupling curve that does not look like a typical REDOR curve. This is due to the fact that the averaged dipolar coupling is no longer axially symmetric. One can also see the asymmetry of the interaction arising from the motion by inspection of the corresponding tensors, shown in Figure 27. It was found there that motion generally leads to asymmetric tensors, unless the motion has three-fold (C_3) or higher symmetry and equal populations.

In the overwhelming majority of cases reported in the literature on dipolar-coupling measurements, the asymmetry of the averaged dipolar-coupling tensor is ignored, and only the scaling of the anisotropy is considered. The reason for this is that while the anisotropy is rather straightforward to measure (reflected by the oscillation frequency in the time domain, or a splitting observed in the frequency domain), the effects of tensor asymmetry are more subtle. The asymmetry is primarily manifest as a distortion of the recoupling curve. This is illustrated for the case of REDOR recoupling using a two-site jump model in Figure 29. However, in many recoupling sequences, a damping or distortion of the recoupling can also arise from experimental imperfections, remote spins or relaxation during the recoupling sequence [149,152,153]. In most experiments, the recoupling curves (or Fourier transforms thereof) need to be fitted with empirical parameters such as a zero-frequency component or a damping, thus masking asymmetry effect. One notable exception is the REDOR experiment that has a built-in normalization, which eliminates the need to use ad hoc empirical fit parameters. In a recent application, REDOR has been applied to characterize non-symmetric side-chain motions [154].

3.4.1 Experimental measurement of anisotropic interactions—The amplitudes of motion (reflected in order parameters, S, and tensor asymmetry η) can be obtained by comparing the dynamically-averaged anisotropic interaction to the respective rigid-limit value. The accuracy to which motional amplitudes can be obtained depends thus on the accuracy with which the tensor parameters can be obtained experimentally, and the precision of knowledge of the rigid-limit tensor. Accuracy is in fact quite critical, if one wants to interpret motional amplitudes quantitatively or combine them with relaxation data, as illustrated by a simple calculation: consider the case of N-H backbone order parameters in a protein. Typically, amide sites have a squared order parameter, S^2, of approximately 0.85, or an order parameter $S = 0.921$. If the measurement of the dipolar coupling has a systematic error of −5% (or if the uncertainty of the rigid-limit value is of this order of magnitude) one would calculate an order parameter of $S = 0.875$ (or, more relevant when combining with relaxation data, $S^2 = 0.766$). When viewed on an absolute scale of amplitude ($1\text{-}S^2$), this difference is substantial ($1\text{-}S^2 = 0.234$ instead of 0.15), which shows that for *absolute* interpretation of motional amplitudes, and also for joint analyses with relaxation data, one needs to know precisely the rigid-limit value, and one needs experimental approaches that have an accuracy better than 1-2%. We review some common measurement schemes below.

CSA tensors can be measured in solid-state NMR by Herzfeld-Berger analysis of the spinning sideband manifold under slow MAS conditions [155,156], single-crystal measurements [157] or static measurements. However, due to limited resolution under these conditions, and difficulties in obtaining single crystals, these approaches are not generally applicable to proteins. As CSA tensors are relatively small (generally a few kHz), the spinning sideband manifold rapidly disappears when reaching MAS frequencies required for high resolution. Thus, the use of recoupling sequences is required under MAS. Among the currently most-often used approaches are symmetry-based [158] recoupling sequences, such as the C-type-based ROCSA (Recoupling Of CSA) experiment [159] ,which has been used for measuring CSA tensors in several proteins [99,106,156,159,160], and R-type sequences [161]. As is generally the case for recoupling sequences, the precision and accuracy with

which tensor parameters are obtained are impacted by experimental imperfections such as RF-field inhomogeneity or phase transients. Even if CSA tensors can be obtained accurately, the interpretation in terms of dynamic amplitudes is challenged by the fact that the rigid-limit tensor parameters are generally not precisely known. CSA tensors vary from site to site due to differences in local structure, and, for example, hydrogen bonding, particularly for ^{15}N and ^{13}C' sites. Therefore, it is currently difficult to obtain quantitative order parameters from CSA measurements.

Compared to CSA tensors, quadrupolar-coupling tensors are large (about 200 kHz for ^{2}H), and therefore the spinning sideband manifold is readily visible even at MAS frequencies beyond 10-20 kHz. Spinning sidebands can be fitted to extract tensor parameters, which has been reported for proteins [22]. An experimental challenge comes from the fact that the sideband manifold is very large, and exciting it uniformly requires very large RF field strengths (which are generally not available). If uniform excitation cannot be assured, the sideband intensities are skewed, somehow challenging the precision of fits. New ^{2}H excitation and cross-polarization methods may at least partly solve this problem [162,163]. As with the CSA tensors, it is generally difficult to obtain the rigid-limit quadrupolar-coupling tensor parameters, as they depend on the local electron density. This makes absolute quantitative statements about the motional amplitudes difficult.

Dipolar couplings are in this respect more straightforward to interpret, as the rigid-limit coupling tensor is symmetric (see above) and its anisotropy can be readily computed from the type and distance of the involved nuclei, which, for directly bonded nuclei, is generally known to good accuracy. Measuring dipolar-coupling tensors under MAS requires the use of recoupling techniques. A number of approaches have been proposed for measurement of dipolar couplings. They all consist of a rotor-synchronized pulse sequence that counteracts the MAS averaging. The most commonly used approaches are cross-polarization (CP) buildup measurements [164,165], Lee-Goldburg CP [111,166], phase-inverted CP [167,168], DIPSHIFT experiments [169,170], R-sequences [153,158,171,172], homonuclear SPC5 [173], T-MREV [174], or variants of REDOR [147] and TEDOR recoupling [106,175]. Systematic errors of dipolar-coupling measurements often are a challenge, and may arise from: (i) Experimental imperfections of the pulse sequence, in particular RF-field inhomogeneities or missetting of the applied RF-field amplitude. Besides these, the effects of phase transients can also play an important role; phase-transient compensated pulses might be a way to avoid such effects for some of the pulse sequences [176,177]. (ii) Artifacts that are due to other interactions than the one to be measured. Particularly, the measurement of a dipolar coupling between directly bonded nuclei may be impacted by the recoupling of the coupling to other spins. The potential systematic errors due to experimental imperfection have been investigated in a number of studies, such as in references [149,152,153,168], and we do not review all the different sequences here. In our view, the REDOR sequence appears to be among the most robust experiments for measuring heteronuclear dipolar couplings (as long as fairly isolated X-H spin systems are prepared, e.g. by deuteration), and we use this sequence here to exemplify the effects of RF field inhomogeneities.

Figure 30 shows the effects of RF-field amplitude missetting on ^{1}H and ^{15}N RF channels on the apparent (measured) dipolar-coupling tensor anisotropy. Panel (a) shows the pulse

sequence used for measuring H-N dipolar couplings in deuterated amide-protonated proteins. Panel (b) shows a typical RF inhomogeneity profile of a contemporary MAS probe. RF field distributions of the order of 5-10% across the sample volume are generally observed. The observed recoupling curves will, therefore, always be a sum over recoupling curves from different parts of the sample, with different effective recoupling behavior. In addition to this distribution of fields, one also needs to consider the impact that a misadjusted RF-field amplitude has on the recoupling curve. Panels (c) and (d) investigate the effect of RF missetting for the ^{1}H RF field on the measured dipolar coupling, while panel (e) considers the effect of ^{15}N RF missetting (which is very small). Missetting of the ^{1}H RF field by about 10% can lead to an underestimation of the dipolar coupling by about 5%. Note that for other recoupling sequences the errors can be substantially larger. Accurate measurement of dipolar couplings, thus, requires, in addition to choosing a pulse sequence that is as robust as possible, that the RF fields are carefully adjusted, and possibly that RF field inhomogeneities are taken into account when fitting the data. Furthermore, the effects of CSAs and remote spins need to be considered, and these generally vary between different recoupling sequences; CSA effects in some sequences are negligibly small, e.g. in REDOR, or they can be explicitly measured and accounted for in fits of the dipolar coupling [172].

Figure 31 shows experimentally determined ^{1}H-^{15}N dipolar-coupling derived order parameters (plotted here as S^2) in microcrystalline ubiquitin as a function of the amino acid residue. The order parameter profile shown in black was obtained by careful calibration of the RF field strength of the ^{1}H and ^{15}N π pulses; furthermore, when analyzing these data, the previously measured RF field distribution in the coil was taken into account explicitly by applying a scaling factor [110]. Data sets shown in red and blue were recorded with slightly miscalibrated RF field strengths. One can see that as a result, the order parameters are underestimated; this is in agreement with numerical simulations and experimental investigations shown in Figure 30 (c) and (d). Interestingly, the systematic underestimation is, to a good approximation, a uniform scaling factor, as the close agreement between the three data sets after best-fit scaling shows (Figure 31b). This indicates that the relative order parameters between different sites can be obtained very reproducibly, even if the RF field is not very accurately set. With correct setting of the RF field strength one can obtain absolute order parameters. Interestingly, these order parameters are very similar to order parameters determined by relaxation-based solution-state NMR methods, panel (c), indicating that the sub-microsecond motion in solution and crystals is similar; we will further address this question in Section 4.

To summarize this section, the measurement of dynamically-averaged anisotropic interactions (dipolar couplings, CSAs and quadrupolar couplings) provides direct insight into the amplitude of motions. The time scale over which motions are averaged depends on the interaction strength (and some experimental details), and typically the averaging is over time scales shorter than microseconds. Averaged anisotropic interactions provide information about the amplitude and, if the asymmetry can be measured, also about the geometry of the motion. For a quantitative analysis the rigid-limit tensor parameters have to be known, which is most easily available for dipolar couplings. Dynamically-averaged anisotropic interactions are complementary to relaxation data. While the former provide

rather straightforward information about amplitudes, the latter are sensitive to both amplitudes and time scales. A combined use of both observables is thus an attractive route to jointly characterizing rates and amplitudes. The following section illustrates such combined approaches.

3.5 Combination of Averaged Anisotropic Interactions and Relaxation Data to Obtain Information About Motion

The ultimate goal of dynamics studies is an atomic description of the motion of a molecule. In the ideal case, one would like to know all the three-dimensional structures that are inter-converting, as well as their relative populations and the height of the energy barriers between them. Obviously, no experimental technique can currently provide such information directly and we always need to use simplified approaches that characterize approximately the conformational space sampled by a given group of atoms. The best model to choose depends on the type of motion that is expected, which in turn depends primarily on the time scale of the considered motion, and, therefore, on the energy barrier between the involved states. Motions occurring on time scales shorter than microseconds connect states separated by rather low energy barriers. Often these states have similar relative populations, and differ mostly in local bond orientations (bond libration motions). Therefore, most commonly such motions are described with a parameter that describes the effective motional amplitude, and a parameter that describes the time scale of motion. A common model is restricted rotational diffusion (wobbling in a cone). Its advantage is that an (approximate) analytical equation is available for this model [60,101,178-180], and the difference between the different spectral densities $J_0(\omega)$, $J_{\pm1}(\omega)$, $J_{\pm2}(\omega)$ can be accounted for [181] (see Section 2.2.1). Other models have also been used for this purpose, such as Gaussian-Angle Fluctuation (GAF) models [100]. Alternatively to these explicit geometrical models, the “model-free” approach is commonly used. It makes the assumption that the different spectral density functions are all equal, which is incorrect but seems to have essentially no consequences for the analysis (see Section 2.2.1). This approach is based on an assumption about the functional form of the correlation function (exponentially decaying correlation function) rather than a geometrical model, and can be expanded in a straightforward manner to include more than one exponentially decaying component. This is of advantage when modeling several dynamics processes on different time scales from experimental data. We will use this model here to investigate how available experimental data (relaxation data and dipolar-coupling derived order parameters) can be used in a joint fit of amplitudes and time scales of motions.

Figure 32 recapitulates the functional dependence of ^{15}N relaxation rate constants as a function of the motional parameters in the “model-free” approach (S^2 and τ). Calculations for different static magnetic fields are shown, and in the case of $R_{1\varrho}$, also different RF-field amplitudes are considered. Combining several measurements, i.e., R_1 and $R_{1\varrho}$ measurements at different fields might be a way to obtain the amplitudes and time scales of the underlying motion. Is such a fit possible – in other words, is the solution one obtains unique and unambiguous, or is it ill-defined? This question has been addressed in detail and by different means by a few recent studies [110,154,178,180,182], and we aim to summarise the main conclusions in Figure 32g and h. To this end, we assume a certain motional model, i.e. we assume an N-H site that undergoes motion described by an order parameter ($S^2 = 0.85$) and a

time scale of either 100 ps (panel g) or 50 ns (panel h). No matter if the motion is on a picosecond or nanosecond time scale, if only longitudinal relaxation-rate constants obtained at different B_0 field are combined, the amplitude of motion is very poorly defined. This is due to the fact that R_1 relaxation-rate constants have only a weak dependence on the B_0 field, and combining several measurements does not provide a strong constraint on the fitted value of S^2. The obvious solution is to combine such data with other data that have a very different dependence on S^2 and τ. This can be achieved by adding transverse relaxation parameters, such as ^{15}N $R_{1\varrho}$, or cross-correlated relaxation-rate constants, discussed in Section 3.4. In Figure 32 we explore the use of ^{15}N $R_{1\varrho}$ rate constants. Figure 32g shows that in the case that the motion is fast (sub-nanosecond), the ^{15}N $R_{1\varrho}$ measurement hardly provides any additional information. This is because when the motion is fast the absolute value of the relaxation rate constant is far below the experimental error, or the contributions of coherent dephasing to $R_{1\varrho}$. Only if the motion is slow (nanosecond-to-microsecond regime), the transverse relaxation rate constant allows restraining the parameter space. In practice, however, one can expect that there is always fast local motion, such that combining R_1 and $R_{1\varrho}$ measurements to extract order parameters and time scales of motion generally fails (see below). Another possibility is to use relaxation parameters from other nuclei, e.g. carbonyl-^{13}C or $^{13}C^{\alpha}$, which are sensitive to different frequencies of the spectral-density function. Such an approach has been proposed recently [178]; it depends on specific assumptions about the backbone motion, such as rigidity of the peptide plane limiting motions to those affecting ^{15}N and ^{13}CO equally. Another approach is to measure directly the dipolar-coupling derived order parameter, and use it in a combined fit with relaxation data [98,128,178].

Several recent studies investigated the outcome of model-free analyses of experimental or *in-silico* data of protein backbone motion [99,110,178,180,183]. These studies suggest that fits of relaxation data alone, without fixing the order parameter to an independently determined dipolar-coupling derived order parameter leads to systematically overestimated values of S^2, and erroneous detection of nanosecond motion. Figure 33 demonstrates for a case study of ubiquitin, in which 6 different relaxation data sets were fitted with or without dipolar-coupling based S^2 values, that inclusion of dipolar-coupling derived order parameter is essential to obtain physically meaningful dynamics parameters.

In practice, the simple model we have considered so far, namely that the motion can be described by a single motional process, is likely to be too simplistic. The relaxation-rate constants considered are sensitive to motions occurring on time scales from picoseconds to several milliseconds (see Figure 32), and it seems likely that more motional modes have to be included. Two-time scale model-free fits have been employed previously [98,110,128,178,180], and even three-time scale models have been fitted, and there seemed to be evidence that such a complex model is statistically justified [101]. Of course, such multi-parameter models are a challenge in terms of uniqueness of the solution; furthermore, some of the motional components may have extremely low motional amplitude, if they occur on the time scale to which the relaxation-rate constant is most sensitive. When it comes to fitting very low-amplitude motional modes, one also needs to consider the potential influence of systematic errors on the raw data, e.g., residual spin diffusion or dipolar

dephasing, or failure of the Redfield theory to accurately describe the relaxation-rate constants outside the regime of this theory.

In the above discussion, we have only considered spin relaxation arising through fluctuation of dipolar couplings and CSA tensors. In principle, the fluctuation of the chemical shift can also be exploited to gain information about motion on longer time scales (microseconds to milliseconds). In this time scale, coherence decay (transverse relaxation) can be induced by fluctuations of any of these parameters, i.e. isotropic or anisotropic chemical shifts, and dipolar couplings (see Figure 32 and the discussion about relaxation dispersion in Section 3.3.3). Fitting dynamics over time scales from picoseconds to milliseconds will require a combined use of Redfield-theory based equations, and approaches used for analyzing, e.g., relaxation-dispersion data (see Section 3.3.3). Such an analysis may be complicated by the fact that slower motions may be diffusion-like, i.e. may be described by an order parameter, but microsecond motion may also involve higher-energy barriers, and involve few distinct states. Global models that attempt to describe motions on a wide range of time scales will need to model such complex motions, and deal with the problem of over-fitting which is often incurred.

4 Selected Examples of Recent Applications: How do Protein Motions in Crystals Differ from those in Solution?

In this last section, we show a few selected examples in which MAS solid-state NMR has been used to characterize protein dynamics. There is a growing number of interesting dynamics studies that address proteins of increasing complexity and biological interest, such as membrane proteins [104,184,185] and amyloid fibrils [106,186,187]. For reasons of limited space we focus here only on one particular aspect of biomolecular dynamics. We want to review how protein dynamics in crystals differ from the dynamics in solution. Does the crystalline lattice limit the motional freedom of proteins, or change the relative populations of states? Or is the water-rich environment of a crystal (filled to about 50% with water) essentially identical to free solution, where protein motions are concerned? As crystalline preparations are the most extensively studied ones by solid-state NMR, a coherent picture is emerging now about protein motion in crystals, in particular for model systems such as SH3, GB1 and ubiquitin.

When comparing protein dynamics in solution and solids, one needs to remember the methodological differences; in particular, relaxation-derived order parameters in solution report only on motions faster than the overall-tumbling correlation time (typically a few nanoseconds). In contrast, solid-state relaxation-rate constants probe internal motion over much wider time scales, as overall tumbling is absent; likewise, dipolar-coupling order parameters also probe motions from pico- to microseconds. In the light of these differences it is interesting to note that order parameters of SH3 and ubiquitin in solution and crystals are very similar. Figure 34 shows experimental S^2 values for chicken α-spectrin SH3 and ubiquitin obtained in the solid state as well as in solution; furthermore, simulated order parameters, derived from MD simulations of a representative portion of a crystal lattice, and a molecule in solution, respectively, are shown. Overall, the absolute amplitude of motion

appears to be very similar for most of the residues. Small exceptions could be identified. For example, the loop around residues 7-11 in ubiquitin shows somewhat larger amplitudes in solution; likewise, residue Q62 in ubiquitin, also located in a loop region, appears more mobile in solution than in the crystal. In SH3, curiously, residue Asn38 becomes more mobile in the crystal than in solution, as seen by MD simulations [182] (residue not in the experimental data of Figure 34a). This residue seems to co-exist in two conformations in the crystal, stabilized by intermolecular interactions, and exchanges between them; in contrast, in solution it is only in one conformation, which explains why it has less mobility in solution than in the crystal. Taken together, these data suggest that the backbone motion on sub-microsecond time scales is very similar in solution and crystals, with a handful of exceptions located primarily in loop regions. Qualitatively, this picture has also been seen in other proteins, such as thioredoxin [99] and GB1 [179,180].

There is further support for the conclusion that the crystal lattice has rather limited impact on fast motions. Figure 35 shows two examples that suggest that side-chain motions also behave similarly in solution and in crystals. Figure 35a presents a comparison between ^{13}C R_1 relaxation rate constants of $^{13}CHD_2$-labeled Val/Leu methyl groups in the protein chicken α-spectrin SH3 in solution and in a crystal. For this comparison, the overall-tumbling contribution to the solution-state rate constants has been subtracted. The R_1 rate constants are clearly highly correlated, showing that the pico- to nanosecond motions probed by this rate constant are hardly affected by the crystalline environment. Another investigation of side chain dynamics has been reported for the protein ubiquitin, shown in Figure 35b-e. Here we look at H-C (asymmetric) dipolar couplings of Val residues, labeled with $^{13}CHD_2$ in an otherwise deuterated background. While three out of the four valines show a rather large, and essentially symmetric dipolar coupling tensor, Val 70 has a lower tensor anisotropy, and non-zero asymmetry. These data show that Val 70 samples different rotamer states, while the other valines populate primarily one rotamer state. Interestingly, solution-state NMR comes to the same conclusions [188], and even the relative rotamer populations are in good agreement with the crystal data (see panel d), suggesting that side chain motions (at least for these particular methyl-bearing side chains) behave similarly in solution and crystals.

Another view of the impact of the crystalline environment on protein motion comes from comparisons of a given protein in different crystal packing arrangements. Recently, Ma *et al.* have studied dynamics of ubiquitin in three different crystal forms (crystallizing in different space groups) [189]. Figure 36 compares (panels a and b) observables that are primarily sensitive to sub-microsecond motions. These observables (^{15}N R_1 rate constants and dipolar order parameters) are, overall, similar. Exceptions, for which the dynamics are clearly different between the different crystal forms, are found in the loop (residues 7-11) and for residue Q62; in these two regions of the protein the amplitudes of motion differ, pointing to hindered motion through crystal contacts. Interestingly, this finding mirrors the picture provided by the comparison between solution and crystal data (Figure 34): also there, differences in motions were found for exactly the same regions, while the majority of the protein had very similar motional parameters. MD simulations on different crystal forms of ubiquitin support this view [183,189]. The picture that emerges from the various comparisons above is, therefore, that the crystalline environment does not detectably alter

the dynamics on sub-microsecond time scales, except for a few residues located in loop regions.

In the light of this view, it appears somewhat surprising that $R_{1\varrho}$ rate constants in different crystals are rather different, at least for the cases reported for ubiquitin, as shown in Figure 36c and d. In fact, one of the studied crystals has a systematically higher level of $R_{1\varrho}$ that is to reasonable approximation uniform across the sequence. This offset can be explained by a global motional process of the molecule, i.e. residual overall “rocking” motion. Such a rocking motion predicts also that X-ray diffraction resolution should be lower, and that the Wilson B-factor (reflecting the precision with which the atomic positions can be determined) is higher. These predictions are indeed found experimentally found (Figure 36e). The rocking motion should also lead to slightly lower order parameters, and also this observation is experimentally found (see panel b). Additional support for such overall “rocking” motion in the crystal comes from MD simulations of the different crystals, which detects significant overall residual motion for cubic-PEG-ub [189]. It may be that such overall motion, found here in one particular crystal form, is a general contribution to resolution of solid-state NMR spectra. Further cases need to be studied to draw broad conclusions about the generality of rocking motion in crystals, and also higher-order assemblies.

Finally, we turn to slower motional processes, of microseconds or slower. In Section 3.3 we have discussed methods that allow study of conformational exchange processes on these time scales. In particular, we have discussed differential ZQ/DQ relaxation, CPMG relaxation-dispersion and $R_{1\varrho}$ relaxation dispersion measurements that provide complementary views on exchange dynamics. For the case of ubiquitin, all these experiments have been performed. The picture emerging from these data shows that there is an exchange process in a well-defined region, enclosing the loop of residues D52-T55 (which forms a so-called type-II β-turn structure in microcrystals), as well as the neighboring helix. The exchange process is thought to correspond to a flip of peptide plane D52/G53, and some rearrangement of hydrogen bonds and side chain orientations, as discussed before [44,190,191]. The fitted exchange rate is about 3000 s^{-1}, and the relative populations are approximately 90:10. Interestingly, in the solution state the exchange process is clearly different [190,192]. Although the same residues show exchange, the populations and kinetics are different. At the temperature at which large relaxation-dispersion profiles were seen in solid-state NMR experiments (300 K), the corresponding solution-state dispersion profiles are completely flat, and only at temperatures more than 20 K lower can one observe the exchange process, which is about one order of magnitude faster than in crystals even at this low temperature. Thus, we have here a clear impact of the crystal packing on the dynamics. This apparently slower dynamics in the crystal can be understood by steric clashes of side chains, which hamper the transition between the two involved conformations, as indicated in Figure 37. Furthermore, the order of the two conformations seems to be reversed: the state that has the higher population in the microcrystal seems to correspond to the lower-populated state in solution and vice versa (see Figure 37). Taken together, these data show unambiguously that microsecond exchange processes between distinct states are altered by crystal packing. Differences in slow motion have also been observed for another protein, SH3 [27].

To summarize, we have provided a short review of some recently reported studies that provide insight into the impact of the crystalline environment on protein dynamics. The picture emerging from the cases reported here (SH3, ubiquitin, and also GB1) is the following. Fast dynamics, on picosecond time scales, generally correspond to very local motions, arising primarily from local bond librations. Residues in densely packed structures (secondary structures, hydrophobic core) often are in this category. As one may expect, such motions are hardly impacted by crystal packing, because they are only sensitive to the very local environment. The comparison of sub-microsecond motions discussed above seems to confirm this view: most residues in secondary structures, as well as methyl-bearing side chains, which are mostly in the hydrophobic core, have basically the same motional amplitudes in solution and crystal. Some effect of steric hindrance is seen in loop regions. Again, this seems physically reasonable, as loops often undergo larger-amplitude motions that involve several residues. When going to even longer time scales (microseconds) the available data from ubiquitin suggests that the crystalline environment slows down the motion considerably. Again, given the more concerted nature of such slow motions this is not surprising. One may thus draw a first conclusion and say that the more a particular motion is collective, the more likely it is to be impacted by packing interactions. Although this finding seems physically reasonable, further studies on additional systems will be needed to evaluate the generality of the findings on these first few model protein systems.

5 Conclusions

We have hopefully provided here an overview of the theory relevant to the measurement of molecular dynamics by magic-angle solid-state NMR. From a theoretical standpoint, MAS NMR provides a wealth of information about dynamics, arguably significantly more that its solution-state counterpart. This is because MAS-NMR-derived relaxation parameters are sensitive to a wider range of time scales than those from solution studies, and averaging of both isotropic and anisotropic interactions can be used to characterize dynamics. The fact that there is no molecular tumbling in the solid state therefore means that one can potentially study motion in great detail. On the other hand, it is exactly this presence of multiple interactions that represents a challenge for quantitative measurements of dynamic parameters. We have discussed the challenges of discriminating dynamics-related parameters from other contributions in detail for the case of transverse relaxation-rate constants.

Continuous improvement in MAS NMR hardware, in particular faster sample spinning, in sample preparation and isotope labeling, as well as in new experimental approaches, and the interplay between these different advances, is nowadays rapidly providing new avenues for studying (bio-)molecular motion at increasing levels of detail. Given the new areas of application of MAS NMR to challenging biological systems one can expect to witness a growing importance of this technique in elucidating the role of dynamics in molecular function.

Acknowledgements

This work was financially supported by the European Research Council by a Starting Grant to P. S. (ERC-Stg-2012-311318-ProtDyn2Function), the Swiss National Science Foundation (Grants 200020_124611 and

200020_134681) and the ETH Zürich (Grant ETH-04 09-3). We thank all our colleagues who have been involved in our research reported here, as well as colleagues for fruitful discussions, in particular Nikolai Skrynnikov, Bernd Reif, Alexey Krushelnitsky, Kay Saalwächter, René Verel, Beat H. Meier, Martin Tollinger, Peixiang Ma, Albert A. Smith and Nils-Alexander Lakomek.

Glossary

AHT	average-Hamiltonian theory
CCR	cross-correlated relaxation
CEST	chemical-exchange saturation transfer
CODEX	centerband-only detection of exchange
CPMG	Carr-Purcell-Meiboom-Gill
CSA	chemical-shift anisotropy
DQ	double quantum
EXSY	exchange spectroscopy
GAF	Gaussian axial fluctuations
MAS	magic-angle spinning
MPD	methyl-pentane-diol
MQ	multiple quantum
NMR	nuclear-magnetic resonance
NOE	nuclear Overhauser effect
PEG	poly-ethylene-glycol
RD	relaxation dispersion
REDOR	Rotary Echo Double Resonance
RF	radio frequency
ROCSA	Recoupling of CSA
TROSY	transverse-relaxation optimized spectroscopy
ZQ	zero quantum

References

[1]. Mittermaier AK, Kay LE. Observing biological dynamics at atomic resolution using NMR. Trends in Biochemical Sciences. 2009; 34:601–611. DOI: 10.1016/j.tibs.2009.07.004 [PubMed: 19846313]

[2]. Palmer AG, Massi F. Characterization of the dynamics of biomacromolecules using rotating-frame spin relaxation NMR spectroscopy. Chem Rev. 2006; 106:1700–1719. DOI: 10.1021/Cr0404287 [PubMed: 16683750]

Europe PMC Funders Author Manuscripts

[3]. Palmer AG. NMR characterization of the dynamics of biomacromolecules. Chem Rev. 2004; 104:3623–3640. DOI: 10.1021/Cr030413t [PubMed: 15303831]

[4]. Torchia DA. NMR studies of dynamic biomolecular conformational ensembles. Prog Nucl Mag Res Sp. 2015; 84-85:14–32. DOI: 10.1016/j.pnmrs.2014.11.001

[5]. Ishima R, Torchia DA. Protein dynamics from NMR. Nat Struct Biol. 2000; 7:740–743. DOI: 10.1038/78963 [PubMed: 10966641]

[6]. Zeeb M, Balbach J. Protein folding studied by real-time NMR spectroscopy. Methods. 2004; 34:65–74. DOI: 10.1016/j.ymeth.2004.03.014 [PubMed: 15283916]

[7]. Fürtig B, Buck J, Manoharan V, Bermel W, Jäschke A, Wenter P, Pitsch S, Schwalbe H. Time-resolved NMR studies of RNA folding. Biopolymers. 2007; 86:360–383. DOI: 10.1002/bip.20761 [PubMed: 17595685]

[8]. Schanda P, Forge V, Brutscher B. Protein folding and unfolding studied at atomic resolution by fast two-dimensional NMR spectroscopy. P Natl Acad Sci Usa. 2007; 104:11257–11262. DOI: 10.1073/Pnas.0702069104

[9]. Castellani F, van Rossum B, Diehl A, Schubert M, Rehbein K, Oschkinat H. Structure of a protein determined by solid-state magic-angle-spinning NMR spectroscopy. Nature. 2002; 420:98–102. DOI: 10.1038/nature01070 [PubMed: 12422222]

[10]. Wasmer C, Lange A, Van Melckebeke H, Siemer AB, Riek R, Meier BH. Amyloid fibrils of the HET-s(218-289) prion form a beta solenoid with a triangular hydrophobic core. Science. 2008; 319:1523–1526. DOI: 10.1126/science.1151839 [PubMed: 18339938]

[11]. Loquet A, Sgourakis NG, Gupta R, Giller K, Riedel D, Goosmann C, Griesinger C, Kolbe M, Baker D, Becker S, Lange A. Atomic model of the type III secretion system needle. Nature. 2012; 486:276–279. DOI: 10.1038/nature11079 [PubMed: 22699623]

[12]. Wang S, Ladizhansky V. Progress in Nuclear Magnetic Resonance Spectroscopy. Prog Nucl Mag Res Sp. 2014; 82:1–26. DOI: 10.1016/j.pnmrs.2014.07.001

[13]. Shahid SA, Bardiaux B, Franks WT, Krabben L, Habeck M, van Rossum B-J, Linke D. Membrane-protein structure determination by solid-state NMR spectroscopy of microcrystals. Nat Meth. 2012; 9:1212–1217. DOI: 10.1038/nmeth.2248

[14]. Comellas G, Rienstra CM. Protein structure determination by magic-angle spinning solid-state NMR, and insights into the formation, structure, and stability of amyloid fibrils. Annual Review of Biophysics. 2013; 42:515–536. DOI: 10.1146/annurev-biophys-083012-130356

[15]. Sun S, Siglin A, Williams JC, Polenova T. Solid-state and solution NMR studies of the CAP-Gly domain of mammalian dynactin and its interaction with microtubules. J Am Chem Soc. 2009; 131:10113–10126. DOI: 10.1021/ja902003u [PubMed: 19580321]

[16]. Schanda P, Triboulet S, Laguri C, Bougault CM, Ayala I, Callon M, Arthur M, Simorre J-P. Atomic model of a cell-wall cross-linking enzyme in complex with an intact bacterial peptidoglycan. J Am Chem Soc. 2014; 136:17852–17860. DOI: 10.1021/ja5105987 [PubMed: 25429710]

[17]. Renault M, Boxtel R. Tommassen-van, Bos MP, Post JA, Tommassen J, Baldus M. Cellular solid-state nuclear magnetic resonance spectroscopy. P Natl Acad Sci Usa. 2012; 109:4863–4868. DOI: 10.1073/pnas.1116478109

[18]. Gall CM, Cross TA, DiVerdi JA, Opella SJ. Protein dynamics by solid-state NMR: aromatic rings of the coat protein in fd bacteriophage. P Natl Acad Sci Usa. 1982; 79:101–105.

[19]. Torchia DA. Solid state NMR studies of protein internal dynamics. Annual Review of Biophysics and Bioengineering. 1984; 13:125–144. DOI: 10.1146/annurev.bb.13.060184.001013

[20]. Siminovitch DJ. Solid-state NMR studies of proteins: the view from static 2H NMR experiments. Biochem. Cell Biol. 1998; 76:411–422. [PubMed: 9923710]

[21]. Seelig J. Deuterium magnetic resonance: theory and application to lipid membranes. Q. Rev. Biophys. 1977; 10:353–418. [PubMed: 335428]

[22]. Hologne M, Chen Z, Reif B. Characterization of dynamic processes using deuterium in uniformly H-2, C-13, N-15 enriched peptides by MAS solid-state NMR. J Magn Reson. 2006; 179:20–28. DOI: 10.1016/j.jmr.2005.10.014 [PubMed: 16289962]

[23]. Hansen MR, Graf R, Spiess HW. Solid-State NMR in Macromolecular Systems: Insights on How Molecular Entities Move. Accounts of Chemical Research. 2013; 46:1996–2007. DOI: 10.1021/ar300338b [PubMed: 23480021]

[24]. Cavanagh, J.; Fairbrother, W.; Palmer, AG.; Skelton, N. Protein NMR spectroscopy: Principles and practice. 1996.

[25]. Luginbühl P, Wüthrich K. Semi-classical nuclear spin relaxation theory revisited for use with biological macromolecules. Prog Nucl Mag Res Sp. 2002; 40:199–247. DOI: 10.1016/S0079-6565(01)00043-7

[26]. Krushelnitsky A, Reichert D. Solid-state NMR and protein dynamics. Prog Nucl Mag Res Sp. 2005; 47:1–25. DOI: 10.1016/j.pnmrs.2005.04.001

[27]. Krushelnitsky A, Reichert D, Saalwächter K. Solid-State NMR Approaches to Internal Dynamics of Proteins: From Picoseconds to Microseconds and Seconds. Accounts of Chemical Research. 2013; 46:2028–2036. DOI: 10.1021/ar300292p [PubMed: 23875699]

[28]. Lewandowski JR. Advances in solid-state relaxation methodology for probing site-specific protein dynamics. Acc. Chem. Res. 2013; 46:2018–2027. DOI: 10.1021/ar300334g [PubMed: 23621579]

[29]. Lewandowski J, Emsley L. Relaxation Studies of Solid Biopolymers. Encyclopedia of Magnetic Resonance (EMR) online, Encyclopedia of Magnetic Resonance. 2010:1–9.

[30]. Ma P, Schanda P. Conformational Exchange Processes in Biological Systems: Detection by Solid-State NMR. eMagRes. 2015; 4:699–708. DOI: 10.1002/9780470034590.emrstm1418

[31]. Tomaselli M, Yarger JL, Augustine MP, Pines A. Scalar and anisotropic J interactions in undoped InP: A triple-resonance NMR study. Phys Rev B. 1998

[32]. Meier BH, Ernst RR. Elucidation of chemical exchange networks by two-dimensional NMR spectroscopy: the heptamethylbenzenonium ion. J Am Chem Soc. 1979; 101:6441–6442. DOI: 10.1021/ja00515a053

[33]. Vallurupalli P, Bouvignies G, Kay LE. Studying “invisible” excited protein states in slow exchange with a major state conformation. J Am Chem Soc. 2012; 134:8148–8161. DOI: 10.1021/ja3001419 [PubMed: 22554188]

[34]. Fawzi NL, Ying J, Ghirlando R, Torchia DA, Clore GM. Atomic resolution dynamics on the surface of amyloid protofibrils probed by solution NMR. Nature. 2011; 480:268–272. DOI: 10.1038/nature10577 [PubMed: 22037310]

[35]. Palmer AG III. Chemical exchange in biomacromolecules: Past, present, and future. J Magn Reson. 2014; doi: 10.1016/j.jmr.2014.01.008

[36]. deAzevedo ER, Hu WG, Bonagamba ATJ, Schmidt-Rohr K. Centerband-Only Detection of Exchange: Efficient Analysis of Dynamics in Solids by NMR. J Am Chem Soc. 1999; 121:8411–8412.

[37]. Krushelnitsky A, deAzevedo E, Linser R, Reif B, Saalwaechter K, Reichert D. Direct Observation of Millisecond to Second Motions in Proteins by Dipolar CODEX NMR Spectroscopy. J Am Chem Soc. 2009; 131:12097–12099. DOI: 10.1021/ja9038888 [PubMed: 19673476]

[38]. deAzevedo E, Hu WG, Bonagamba TJ, Schmidt-Rohr K. Principles of center-band-only detection of exchange in solid-state nuclear magnetic resonance, and extension to four-time centerband-only detection of exchange. J Chem Phys. 2000; 112:8988.

[39]. Li W, McDermott A. Investigation of slow molecular dynamics using R-CODEX. J Magn Reson. 2012; 222:74–80. DOI: 10.1016/j.jmr.2012.05.019 [PubMed: 22824462]

[40]. Mulder FA, Mittermaier A, Hon B, Dahlquist FW, Kay LE. Studying excited states of proteins by NMR spectroscopy. Nat Struct Biol. 2001; 8:932–935. DOI: 10.1038/nsb1101-932 [PubMed: 11685237]

[41]. Sekhar A, Kay LE. NMR paves the way for atomic level descriptions of sparsely populated, transiently formed biomolecular conformers. P Natl Acad Sci U.S.a. 2013; 110:12867–12874. DOI: 10.1073/pnas.1305688110

[42]. Neudecker P, Lundstrom P, Kay LE. Relaxation Dispersion NMR Spectroscopy as a Tool for Detailed Studies of Protein Folding. Biophys J. 2009; 96:2045–2054. DOI: 10.1016/j.bpj.2008.12.3907 [PubMed: 19289032]

[43]. Bruschweiler S, Schanda P, Kloiber K, Brutscher B, Kontaxis G, Konrat R, Tollinger M. Direct Observation of the Dynamic Process Underlying Allosteric Signal Transmission. J Am Chem Soc. 2009; 131:3063–3068. DOI: 10.1021/Ja809947w [PubMed: 19203263]

[44]. Tollinger M, Sivertsen AC, Meier BH, Ernst M, Schanda P. Site-Resolved Measurement of Microsecond-to-Millisecond Conformational-Exchange Processes in Proteins by Solid-State NMR Spectroscopy. J Am Chem Soc. 2012; 134:14800–14807. DOI: 10.1021/ja303591y [PubMed: 22908968]

[45]. Ma P, Haller JD, Zajakala J, Macek P, Sivertsen AC, Willbold D, Boisbouvier J, Schanda P. Probing transient conformational states of proteins by solid-state $R_{1\varrho}$ relaxation-dispersion NMR spectroscopy. Angew Chem Int. Ed. Engl. 2014; 53:4312–4317. DOI: 10.1002/anie.201311275 [PubMed: 24644028]

[46]. Redfield AG. On the theory of relaxation processes. IBM J. Res. Devel. 1957; 1:19–31.

[47]. Redfield AG. Intramolecular dipolar relaxation in multi-spin systems. Adv. Magn. Reson. 1966; 1:1–32.

[48]. Wangsness RK, Bloch F. The Dynamical Theory of Nuclear Induction. Phys. Rev. 1953; 89:728–739.

[49]. Abragam, A. The principles of Nuclear Magnetism. Oxford University Press; 1961.

[50]. Cavanagh, J.; Fairbrother, WJ.; Palmer, I. Arthur G; Skelton, NJ.; Rance, M. Protein NMR Spectroscopy. Academic Press; Burlington, San Diego, London: 2010.

[51]. McConnell, J. The theory of nuclear magnetic relaxation in liquids. Cambridge University Press; 2009.

[52]. Kowalewski, J.; Maler, L. Nuclear Spin Relaxation in Liquids: Theory, Experiments and Applications. CRC Press; 2006.

[53]. Goldman M. Formal theory of spin--lattice relaxation. J Magn Reson. 2001; 149:160–187. DOI: 10.1006/jmre.2000.2239 [PubMed: 11318616]

[54]. Brink, DM.; Satchler, GR. Angular Momentum. Oxford University Press on Demand; 1993.

[55]. Mehring, M. Principles of high-resolution NMR in solids. Springer Verlag; Berlin, New York: 1983.

[56]. Werbelow LG. NMR dynamic frequency shifts and the quadrupolar interaction. J Chem Phys. 1979

[57]. Werbelow, LG. Dynamic Frequency Shift. John Wiley & Sons, Ltd; Chichester, UK: 2007.

[58]. Wittebort RJ, Szabo A. Theory of NMR relaxation in macromolecules: Restricted diffusion and jump models for multiple internal rotations in amino acid side chains. J Chem Phys. 1978; 69:1722.

[59]. Torchia DA, Szabo A. Spin-Lattice Relaxation in Solids. J Magn Reson. 1982; 49:107–121.

[60]. Lipari G, Szabo A. Pade approximants to correlation functions for restricted rotational diffusion. J Chem Phys. 1981

[61]. Lipari G, Szabo A. Model-free approach to the interpretation of nuclear magnetic-resonance relaxation in macromolecules: 1. Theory and range of validity. J Am Chem Soc. 1982; 104:4546–4559.

[62]. Lipari G, Szabo A. Model-free approach to the interpretation of nuclear magnetic resonance relaxation in macromolecules. 2. Analysis of experimental results. J Am Chem Soc. 1982; 104:4559–4570.

[63]. Haeberlen U, Waugh JS. Spin-lattice relaxation in periodically perturbed systems. Phys. Rev. 1969; 185:420.

[64]. Redfield AG. Magnetic Resonance Saturation and Rotary Saturation in Solids. Phys. Rev. 1955; 98:1787–1809.

[65]. Bull TE. Relaxation in the rotating frame in liquids. Prog Nucl Mag Res Sp. 1992; 24:377–410.

[66]. Palke WE, Gerig J. Relaxation in the presence of an rf field. Concepts Magn. Reson. 1997; 9:347–353.

[67]. Desvaux H, Berthault P. Study of dynamic processes in liquids using off-resonance rf irradiation. Prog Nucl Mag Res Sp. 1992; 35:295–340.

[68]. Lipari G, Szabo A. Effect of librational motion on fluorescence depolarization and nuclear magnetic resonance relaxation in macromolecules and membranes. Biophysj. 1980; 30:489–506. DOI: 10.1016/S0006-3495(80)85109-5

[69]. Abergel D, Palmer AG. On the use of the stochastic Liouville equation in nuclear magnetic resonance: Application to $R_{1\varrho}$ relaxation in the presence of exchange. Concepts Magn. Reson. 2003; 19A:134–148. DOI: 10.1002/cmr.a.10091

[70]. Vega, AJ.; Fiat, D. Relaxation theory and the stochastic Liouville equation. Journal of Magnetic Resonance (1969). 1975.

[71]. Kubo R. Stochastic liouville equations. J. Math. Phys. 1963; 4:174–183.

[72]. Haeberlen, U. High resolution NMR in solids : selective averaging. Academic Press; New York: 1976.

[73]. Carr HY, Purcell EM. Effects of Diffusion on Free Precession in Nuclear Magnetic Resonance Experiments. Phys. Rev. 1954; 94:630–638.

[74]. Meiboom S, Gill D. Modified Spin-Echo Method for Measuring Nuclear Relaxation Times. Rev. Sci. Instrum. 1958; 29:688–691.

[75]. Maricq MM, Waugh JS. NMR in rotating solids. J Chem Phys. 1979; 70:3300–3316. DOI: 10.1063/1.437915

[76]. Suwelack D, Rothwell WP, Waugh JS. Slow molecular motion detected in the NMR spectra of rotating solids. J Chem Phys. 1980; 73:2559.

[77]. Bennett, AE.; Griffin, RG.; Vega, S. Recoupling of homo- and heteronuclear dipolar interactions in rotating solids. NMR Basic Principles and Progress. 1994.

[78]. Dusold S, Sebald A. Dipolar recoupling under magic-angle spinning conditions. Ann. Rep. NMR Spectr. 2000; 41:185–264.

[79]. Nielsen NC, Strassø LA, Nielsen AB. Dipolar recoupling. Top Curr Chem. 2012; 306:1–45. DOI: 10.1007/128_2011_129 [PubMed: 21516391]

[80]. Scholz I, van Beek JD, Ernst M. Operator-based Floquet theory in solid-state NMR. Solid State Nucl Mag. 2010; 37:39–59. DOI: 10.1016/j.ssnmr.2010.04.003

[81]. Long JR, Sun BQ, Bowen A, Griffin RG. Molecular Dynamics and Magic Angle Spinning NMR. J Am Chem Soc. 1994; 116:11950–11956. DOI: 10.1021/ja00105a039

[82]. Reichert D. NMR Studies of Dynamic Processes in Organic Solids. ChemInform. 2007; 38doi: 10.1002/chin.200711275

[83]. Hahn EL. Spin Echoes. Phys. Rev. 1950; 80:580–594.

[84]. Ernst, M.; Meier, BH. Spin diffusion in solids. In: Ando, I., editor. Solid State NMR of Polymers, Studies in Physical and Theoretical Chemistry. 1998. p. 83-121.

[85]. Grommek A, Meier BH, Ernst M. Distance information from proton-driven spin diffusion under MAS. Chem Phys Lett. 2006

[86]. Bloembergen N. On the interaction of nuclear spins in a crystalline lattice. Physica. 1949; 15:386–426.

[87]. Asami S, Porter JR, Lange OF, Reif B. Access to Cα Backbone Dynamics of Biological Solids by 13C T1Relaxation and Molecular Dynamics Simulation. J Am Chem Soc. 2015; 137:1094–1100. DOI: 10.1021/ja509367q [PubMed: 25564702]

[88]. Reif B. Ultra-high resolution in MAS solid-state NMR of perdeuterated proteins: implications for structure and dynamics. J Magn Reson. 2012; 216:1–12. DOI: 10.1016/j.jmr.2011.12.017 [PubMed: 22280934]

[89]. Chevelkov V, Rehbein K, Diehl A, Reif B. Ultrahigh resolution in proton solid-state NMR spectroscopy at high levels of deuteration. Angew Chem Int. Ed. Engl. 2006; 45:3878–3881. DOI: 10.1002/anie.200600328 [PubMed: 16646097]

[90]. Zhou D, Shea J, Nieuwkoop A, Franks W, Wylie B, Mullen C, Sandoz D, Rienstra C. Solid-state protein-structure determination with proton-detected triple-resonance 3D magic-angle-spinning NMR spectroscopy. Angew Chem Int. Ed. Engl. 2007; 46:8380–8383. DOI: 10.1002/anie.200702905 [PubMed: 17907259]

[91]. Paulson E, Morcombe C, Gapenko V, Dancheck B, Byrd RA, Zilm KW. Sensitive high-resolution inverse detection NMR spectroscopy of proteins in the solid state. J Am Chem Soc. 2003; 125:15831–15836. [PubMed: 14677974]

[92]. Schanda P, Huber M, Verel R, Ernst M, Meier BH. Direct detection of (3h)J(NC') hydrogen-bond scalar couplings in proteins by solid-state NMR spectroscopy. Angew Chem Int. Ed. Engl. 2009; 48:9322–9325. DOI: 10.1002/anie.200904411 [PubMed: 19894242]

[93]. Knight MJ, Webber AL, Pell AJ, Guerry P, Barbet-Massin E, Bertini I, Felli IC, Gonnelli L, Pierattelli R, Emsley L, Lesage A, Herrmann T, Pintacuda G. Fast resonance assignment and fold determination of human superoxide dismutase by high-resolution proton-detected solid-state MAS NMR spectroscopy. Angew Chem Int. Ed. Engl. 2011; 50:11697–11701. DOI: 10.1002/anie.201106340 [PubMed: 21998020]

[94]. Giraud N, Blackledge M, Böckmann A, Emsley L. The influence of nitrogen-15 proton-driven spin diffusion on the measurement of nitrogen-15 longitudinal relaxation times. J Magn Reson. 2007; 184:51–61. [PubMed: 17030133]

[95]. Krushelnitsky A, Bräuniger T, Reichert D. 15N spin diffusion rate in solid-state NMR of totally enriched proteins: The magic angle spinning frequency effect. J Magn Reson. 2006; 182:339–342. DOI: 10.1016/j.jmr.2006.06.028 [PubMed: 16854606]

[96]. Chevelkov V, Diehl A, Reif B. Measurement of 15N-T1 relaxation rates in a perdeuterated protein by magic angle spinning solid-state nuclear magnetic resonance spectroscopy. J Chem Phys. 2008; 128:052316.doi: 10.1063/1.2819311 [PubMed: 18266433]

[97]. Giraud N, Sein J, Pintacuda G, Böckmann A, Lesage A, Blackledge M, Emsley L. Observation of heteronuclear overhauser effects confirms the N-15-H-1 dipolar relaxation mechanism in a crystalline protein. J Am Chem Soc. 2006; 128:12398–12399. [PubMed: 16984173]

[98]. Schanda P, Meier BH, Ernst M. Quantitative analysis of protein backbone dynamics in microcrystalline ubiquitin by solid-state NMR spectroscopy. J Am Chem Soc. 2010; 132:15957–15967. DOI: 10.1021/ja100726a [PubMed: 20977205]

[99]. Yang J, Tasayco M, Polenova T. Dynamics of Reassembled Thioredoxin Studied by Magic Angle Spinning NMR: Snapshots from Different Time Scales. J Am Chem Soc. 2009; 131:13690–13702. DOI: 10.1021/ja9037802 [PubMed: 19736935]

[100]. Knight MJ, Pell AJ, Bertini I, Felli IC, Gonnelli L, Pierattelli R, Herrmann T, Emsley L, Pintacuda G. Structure and backbone dynamics of a microcrystalline metalloprotein by solid-state NMR. P Natl Acad Sci U.S.a. 2012; doi: 10.1073/pnas.1204515109

[101]. Zinkevich T, Chevelkov V, Reif B, Saalwächter K, Krushelnitsky A. Internal protein dynamics on ps to μs timescales as studied by multi-frequency 15N solid-state NMR relaxation. J Biomol NMR. 2013; doi: 10.1007/s10858-013-9782-2

[102]. Lewandowski JR, Sein J, Sass HJ, Grzesiek S, Blackledge M, Emsley L. Measurement of site-specific 13C spin-lattice relaxation in a crystalline protein. J Am Chem Soc. 2010; 132:8252–8254. DOI: 10.1021/ja102744b [PubMed: 20507068]

[103]. Werbelow LG, Grant DM. Intramolecular dipolar relaxation in multi-spin systems. Adv. Magn. Reson. 1977; 9:189–275.

[104]. Ader C, Pongs O, Becker S, Baldus M. Protein dynamics detected in a membrane-embedded potassium channel using two-dimensional solid-state NMR spectroscopy. Biochim Biophys Acta. 2010; 1798:286–290. DOI: 10.1016/j.bbamem.2009.06.023 [PubMed: 19595989]

[105]. Giraud N, Böckmann A, Lesage A, Penin F, Blackledge M, Emsley L. Site-specific backbone dynamics from a crystalline protein by solid-state NMR spectroscopy. J Am Chem Soc. 2004; 126:11422–11423. [PubMed: 15366872]

[106]. Helmus J, Surewicz K, Surewicz W, Jaroniec C. Conformational flexibility of Y154Stop human prion protein amyloid fibrils probed by solid-state nuclear magnetic resonance spectroscopy. J Am Chem Soc. 2010; 132:2393–2403. DOI: 10.1021/ja909827v [PubMed: 20121096]

[107]. Amo JMLD, Agarwal V, Sarkar R, Porter J, Asami S, Rübbelke M, Fink U, Xue Y, Lange OF, Reif B. Site-specific analysis of heteronuclear Overhauser effects in microcrystalline proteins. J Biomol NMR. 2014; 59:241–249. DOI: 10.1007/s10858-014-9843-1 [PubMed: 24989039]

[108]. Moro G, Freed JH. Efficient computation of magnetic resonance spectra and related correlation functions from stochastic Liouville equations. J. Phys. Chem. B. 1980; 84:2837–2840. DOI: 10.1021/j100459a001

[109]. Rothwell WP, Waugh JS. Transverse relaxation of dipolar coupled spin systems under rf irradiation: detecting motions in solids. J Chem Phys. 1981; 74:2721–2732.

[110]. Haller JD, Schanda P. Amplitudes and time scales of picosecond-to-microsecond motion in proteins studied by solid-state NMR: a critical evaluation of experimental approaches and application to crystalline ubiquitin. J Biomol NMR. 2013; 57:263–280. DOI: 10.1007/s10858-013-9787-x [PubMed: 24105432]

[111]. Lorieau J, McDermott A. Conformational flexibility of a microcrystalline globular protein: Order parameters by solid-state NMR spectroscopy. J Am Chem Soc. 2006; 128:11505–11512. DOI: 10.1021/ja062443u [PubMed: 16939274]

[112]. Chevelkov V, Faelber K, Schrey A, Rehbein K, Diehl A, Reif B. Differential line broadening in MAS solid-state NMR due to dynamic interference. J Am Chem Soc. 2007; 129:10195–10200. DOI: 10.1021/ja072024c [PubMed: 17663552]

[113]. Krushelnitsky A, Zinkevich T, Reichert D, Chevelkov V, Reif B. Microsecond Time Scale Mobility in a Solid Protein As Studied by the 15N R1ϱSite-Specific NMR Relaxation Rates. J Am Chem Soc. 2010; 132:11850–11853. DOI: 10.1021/ja103582n [PubMed: 20690699]

[114]. Lewandowski JR, Sass HJ, Grzesiek S, Blackledge M, Emsley L. Site-specific measurement of slow motions in proteins. J Am Chem Soc. 2011; 133:16762–16765. DOI: 10.1021/ja206815h [PubMed: 21923156]

[115]. Brutscher B. Principles and applications of cross-correlated relaxation in biomolecules. Concepts Magn. Reson. 2000

[116]. Kumar A, Grace RCR, Madhu PK. Cross-correlations in NMR. Prog Nucl Mag Res Sp. 2000; 37:191–319.

[117]. Reif B, Diener A, Hennig M, Maurer M, Griesinger C. Cross-correlated relaxation for the measurement of angles between tensorial interactions. J Magn Reson. 2000; 143:45–68. DOI: 10.1006/jmre.1999.1980 [PubMed: 10698646]

[118]. Reif B, Hennig M, Griesinger C. Direct measurement of angles between bond vectors in high-resolution NMR. Science. 1997; 276:1230–1233. [PubMed: 9157875]

[119]. Pelupessy P, Chiarparin E, Ghose R, Bodenhausen G. Simultaneous determination of Ψ and Φ angles in proteins from measurements of cross-correlated relaxation effects. J Biomol NMR. 1999; 14:277–280. DOI: 10.1023/A:1008339928400

[120]. Harris RK, Packer KJ, Thayer AM. Slow magic-angle rotation 13 C NMR studies of solid phosphonium iodides. The interplay of dipolar, shielding, and indirect coupling tensors. J Magn Reson. 1985; 62:284–297.

[121]. Nakai T, McDowell CA. An analysis of NMR spinning sidebands of homonuclear two-spin systems using Floquet theory. Mol Phys. 1992; 77:569–584. DOI: 10.1080/00268979200102631

[122]. Duma L, Hediger S, Lesage A, Sakellariou D, Emsley L. Carbon-13 lineshapes in solid-state NMR of labeled compounds. Effects of coherent CSA-dipolar cross-correlation. J Magn Reson. 2003; 162:90–101. DOI: 10.1016/S1090-7807(02)00174-X [PubMed: 12762986]

[123]. Igumenova TI, McDermott AE. Improvement of resolution in solid state NMR spectra with J-decoupling: an analysis of lineshape contributions in uniformly 13C-enriched amino acids and proteins. J Magn Reson. 2003; 164:270–285. [PubMed: 14511595]

[124]. Pervushin K, Riek R, Wider G, Wüthrich K. Attenuated T2 relaxation by mutual cancellation of dipole-dipole coupling and chemical shift anisotropy indicates an avenue to NMR structures of very large biological macromolecules in solution. P Natl Acad Sci Usa. 1997; 94:12366–12371.

[125]. Chevelkov V, Reif B. TROSY effects in MAS solid-state NMR. Concepts in Magnetic Resonance Part A. 2008; 32A:143–156. DOI: 10.1002/Cmr.A.20106

[126]. Pervushin K. Impact of transverse relaxation optimized spectroscopy (TROSY) on NMR as a technique in structural biology. Q. Rev. Biophys. 2000; 33:161–197. [PubMed: 11131563]

[127]. Skrynnikov N. Asymmetric doublets in MAS NMR: coherent and incoherent mechanisms. Magn Reson Chem. 2007; 45:S161–S173. DOI: 10.1002/Mrc.2162 [PubMed: 18157846]

[128]. Chevelkov V, Fink U, Reif B. Quantitative analysis of backbone motion in proteins using MAS solid-state NMR spectroscopy. J Biomol NMR. 2009; 45:197–206. DOI: 10.1007/s10858-009-9348-5 [PubMed: 19629713]

[129]. Chevelkov V, Diehl A, Reif B. Quantitative measurement of differential N-15-H-alpha/beta T-2 relaxation rates in a perdeuterated protein by MAS solid-state NMR spectroscopy. Magn Reson Chem. 2007; 45:S156–S160. DOI: 10.1002/Mrc.2129 [PubMed: 18157805]

[130]. Linser R, Fink U, Reif B. Assignment of dynamic regions in biological solids enabled by spin-state selective NMR experiments. J Am Chem Soc. 2010; 132:8891–8893. DOI: 10.1021/ja102612m [PubMed: 20536176]

[131]. Wang C, Palmer A. Differential multiple quantum relaxation caused by chemical exchange outside the fast exchange limit. J Biomol NMR. 2002; 24:263–268. [PubMed: 12522313]

[132]. Kloiber K, Konrat R. Differential multiple-quantum relaxation arising from cross-correlated time-modulation of isotropic chemical shifts. J Biomol NMR. 2000; 18:33–42. [PubMed: 11061226]

[133]. Quinn CM, McDermott AE. Quantifying conformational dynamics using solid-state $R_{1\varrho}$ experiments. J Magn Reson. 2012; 222:1–7. DOI: 10.1016/j.jmr.2012.05.014 [PubMed: 22820004]

[134]. Quinn C, McDermott A. Monitoring conformational dynamics with solid-state $R_{1\varrho}$ experiments. J Biomol NMR. 2009; 45:5–8. DOI: 10.1007/s10858-009-9346-7 [PubMed: 19636799]

[135]. Kurbanov R, Zinkevich T, Krushelnitsky A. The nuclear magnetic resonance relaxation data analysis in solids: general $R_1/R_{1\varrho}$ equations and the model-free approach. J Chem Phys. 2011; 135:184104.doi: 10.1063/1.3658383 [PubMed: 22088049]

[136]. Ferreira TM, Ollila OHS, Pigliapochi R, Dabkowska AP, Topgaard D. Model-free estimation of the effective correlation time for C-H bond reorientation in amphiphilic bilayers: (1)H-(13)C solid-state NMR and MD simulations. J Chem Phys. 2015; 142:044905.doi: 10.1063/1.4906274 [PubMed: 25638007]

[137]. Krushelnitsky A, Zinkevich T, Reif B, Saalwächter K. Slow motions in micro-crystalline proteins as observed by MAS-dependent 15N rotating-frame NMR relaxation. J Magn Reson. 2014; 248:8–12. DOI: 10.1016/j.jmr.2014.09.007 [PubMed: 25282442]

[138]. McConnell HM. Reaction rates by nuclear magnetic resonance. J Chem Phys. 1958; 28:430.

[139]. Oas TG, Griffin RG, Levitt MH. Rotary resonance recoupling of dipolar interactions in solid-state nuclear magnetic resonance spectroscopy. J Chem Phys. 1988; 89:692.doi: 10.1063/1.455191

[140]. Levitt MH, Oas TG, Griffin RG. Rotary Resonance Recoupling in Heteronuclear Spin Pair Systems. Isr. J. Chem. 2013; 28:271–282. DOI: 10.1002/ijch.198800039

[141]. Vallurupalli P, Hansen D, Stollar E, Meirovitch E, Kay L. Measurement of bond vector orientations in invisible excited states of proteins. P Natl Acad Sci Usa. 2007; 104:18473–18477. DOI: 10.1073/pnas.0708296104

[142]. Mulder FAA, Akke M. Carbonyl ^{13}C transverse relaxation measurements to sample protein backbone dynamics. Magn Reson Chem. 2003; 41:853–865. DOI: 10.1002/mrc.1252

[143]. Loria J, Rance M, Palmer A. A relaxation-compensated Carr-Purcell-Meiboom-Gill sequence for characterizing chemical exchange by NMR spectroscopy. J Am Chem Soc. 1999; 121:2331–2332.

[144]. Paquin R, Pelupessy P, Duma L, Gervais C, Bodenhausen G. Determination of the antisymmetric part of the chemical shift anisotropy tensor via spin relaxation in nuclear magnetic resonance. J Chem Phys. 2010; 133:034506.doi: 10.1063/1.3445777 [PubMed: 20649336]

[145]. Saitô H, Ando I, Ramamoorthy A. Chemical shift tensor - the heart of NMR: Insights into biological aspects of proteins. Prog Nucl Mag Res Sp. 2010; 57:181–228. DOI: 10.1016/j.pnmrs.2010.04.005

[146]. Smith S, Levante T, Meier B, Ernst R. Computer simulations in magnetic resonance. An object-oriented programming approach. J Magn Reson. 1994; 106:75–105.

[147]. Gullion T. Introduction to rotational-echo, double-resonance NMR. Concepts Magn. Reson. 1998; 10:277–289.

[148]. Gullion T, Schaefer J. Detection of weak heteronuclear dipolar coupling by rotational-echo double-resonance nuclear-magnetic-resonance. Adv. Magn. Reson. 1988; 13:57–83.

[149]. Schanda P, Meier BH, Ernst M. Accurate measurement of one-bond H-X hetero-nuclear dipolar couplings in MAS solid-state NMR. J Magn Reson. 2011; 210:246–259. DOI: 10.1016/j.jmr.2011.03.015 [PubMed: 21482161]

[150]. Cobo MF, Achilles A, Reichert D, deAzevedo ER, Saalwächter K. Recoupled separated-local-field experiments and applications to study intermediate-regime molecular motions. J Magn Reson. 2012; 221:85–96. DOI: 10.1016/j.jmr.2012.05.003 [PubMed: 22750254]

[151]. Saalwächter K, Fischbach I. The Application of MAS Recoupling Methods in the Intermediate Motional Regime. J Magn Reson. 2002; 157:17–30. DOI: 10.1006/jmre.2002.2552 [PubMed: 12202129]

[152]. Lu X, Zhang H, Lu M, Vega AJ, Hou G, Polenova T. Results and discussion. Phys Chem Chem Phys. 2016; :1–10. DOI: 10.1039/C5CP07818K

[153]. Gansmüller A, Simorre J-P, Hediger S. Windowed R-PDLF recoupling: A flexible and reliable tool to characterize molecular dynamics. J Magn Reson. 2013; 234:154–164. DOI: 10.1016/j.jmr.2013.06.017 [PubMed: 23880256]

[154]. Schanda P, Huber M, Boisbouvier J, Meier BH, Ernst M. Solid-state NMR measurements of asymmetric dipolar couplings provide insight into protein side-chain motion. Angewandte Chemie (International Ed in English). 2011; 50:11005–11009. DOI: 10.1002/anie.201103944 [PubMed: 21915969]

[155]. Herzfeld J, Berger AE. Sideband intensities in NMR spectra of samples spinning at the magic angle. J Chem Phys. 1980; 73:6021–6030. DOI: 10.1063/1.440136

[156]. Wylie BJ, Franks W. Trent, Rienstra CM. Determinations of 15N chemical shift anisotropy magnitudes in a uniformly 15N,13C-labeled microcrystalline protein by three-dimensional magic-angle spinning nuclear magnetic resonance spectroscopy. J. Phys. Chem. B. 2006; 110:10926–10936. DOI: 10.1021/jp060507h [PubMed: 16771346]

[157]. Chekmenev EY, Zhang Q, Waddell KW, Mashuta MS, Wittebort RJ. 15N Chemical shielding in glycyl tripeptides: measurement by solid-state NMR and correlation with X-ray structure. J Am Chem Soc. 2004; 126:379–384. DOI: 10.1021/ja0370342 [PubMed: 14709105]

[158]. Levitt M. Symmetry-based pulse sequences in magic-angle spinning solid-state NMR. Encyclopedia of Nuclear Magnetic Resonance. 2002; 9:165–196.

[159]. Chan JCC, Tycko R. Recoupling of chemical shift anisotropies in solid-state NMR under high-speed magic-angle spinning and in uniformly [sup 13]C-labeled systems. J Chem Phys. 2003; 118:8378–8389. DOI: 10.1063/1.1565109

[160]. Wylie B, Franks W, Graesser D, Rienstra C. Site-specific 13C chemical shift anisotropy measurements in a uniformly 15N,13C-labeled microcrystalline protein by 3D magic-angle spinning NMR spectroscopy. J Am Chem Soc. 2005; 127:11946–11947. [PubMed: 16117526]

[161]. Hou G, Byeon I-JL, Ahn J, Gronenborn AM, Polenova T. Recoupling of chemical shift anisotropy by R-symmetry sequences in magic angle spinning NMR spectroscopy. J Chem Phys. 2012; 137:134201.doi: 10.1063/1.4754149 [PubMed: 23039592]

[162]. Wei D, Akbey U, Paaske B, Oschkinat H, Reif B, Bjerring M, Nielsen NC. Optimal 2H rf Pulses and 2H–13C Cross-Polarization Methods for Solid-State 2H MAS NMR of Perdeuterated Proteins. The Journal of Physical Chemistry Letters. 2011; 2:1289–1294. DOI: 10.1021/jz200511b [PubMed: 26295423]

[163]. Nielsen AB, Jain S, Ernst M, Meier BH, Nielsen NC. Adiabatic Rotor-Echo-Short-Pulse-Irradiation mediated cross-polarization. J Magn Reson. 2013; 237:147–151. DOI: 10.1016/j.jmr.2013.09.002 [PubMed: 24220613]

[164]. Wang Q, Lu X, Lafon O, Trébosc J, Deng F, Hu B, Chen Q, Amoureux J-P. Measurement of 13C–1H dipolar couplings in solids by using ultra-fast magic-angle spinning NMR spectroscopy with symmetry-based sequences. Phys Chem Chem Phys. 2011; 13:5967.doi: 10.1039/c0cp01907k [PubMed: 21336406]

[165]. Paluch P, Pawlak T, Amoureux J-P, Potrzebowski MJ. Simple and accurate determination of X-H distances under ultra-fast MAS NMR. J Magn Reson. 2013; 233C:56–63. DOI: 10.1016/j.jmr.2013.05.005 [PubMed: 23727588]

[166]. Hong M, Yao X, Jakes K, Huster D. Investigation of molecular motions by Lee-Goldburg cross-polarization NMR Spectroscopy. J. Phys. Chem. B. 2002; 106:7355–7364.

[167]. Dvinskikh S, Zimmermann H, Maliniak A, Sandstrom D. Heteronuclear dipolar recoupling in liquid crystals and solids by PISEMA-type pulse sequences. J Magn Reson. 2003; 164:165–170. DOI: 10.1016/S1090-7807(03)00180-0 [PubMed: 12932469]

[168]. Chevelkov V, Fink U, Reif B. Accurate Determination of Order Parameters from H-1,N-15 Dipolar Couplings in MAS Solid-State NMR Experiments. J Am Chem Soc. 2009; 131:14018–14022. DOI: 10.1021/ja902649u [PubMed: 19743845]

[169]. Munowitz MG, Griffin RG, Bodenhausen G, Huang TH. Two-dimensional rotational spin-echo nuclear magnetic resonance in solids: correlation of chemical shift and dipolar interactions. J Am Chem Soc. 1981; 103:2529–2533.

[170]. Munowitz MG, Griffin RG. Two-dimensional nuclear magnetic resonance in rotating solids: An analysis of line shapes in chemical shift-dipolar spectra. J Chem Phys. 1982

[171]. Zhao X, Sudmeier J, Bachovchin W, Levitt M. Measurement of NH bond lengths by fast magic-angle spinning solid-state NMR spectroscopy: A new method for the quantification of hydrogen bonds. J Am Chem Soc. 2001; 123:11097–11098. [PubMed: 11686729]

[172]. Hou G, Byeon I-JL, Ahn J, Gronenborn AM, Polenova T. 1H– 13C/ 1H– 15N Heteronuclear Dipolar Recoupling by R-Symmetry Sequences Under Fast Magic Angle Spinning for Dynamics Analysis of Biological and Organic Solids. J Am Chem Soc. 2011; 133:18646–18655. DOI: 10.1021/ja203771a [PubMed: 21995349]

[173]. Schneider R, Seidel K, Etzkorn M, Lange A, Becker S, Baldus M. Probing molecular motion by double-quantum (^{13}C,^{13}C) solid-state NMR spectroscopy: application to ubiquitin. J Am Chem Soc. 2010; 132:223–233. [PubMed: 20000710]

[174]. Rienstra C, Hohwy M, Mueller L, Jaroniec C, Reif B, Griffin R. Determination of multiple torsion-angle constraints in U-C-13,N-15-labeled peptides: 3D H-1-N-15-C-13-H-1 dipolar chemical shift NMR spectroscopy in rotating solids. J Am Chem Soc. 2002; 124:11908–11922. DOI: 10.1021/ja020802p [PubMed: 12358535]

[175]. Jaroniec C, Filip C, Griffin R. 3D TEDOR NMR Experiments for the Simultaneous Measurement of Multiple Carbon– Nitrogen Distances in Uniformly 13C, 15N-Labeled Solids. J Am Chem Soc. 2002

[176]. Tabuchi Y, Negoro M. Total compensation of pulse transients inside a resonantor. J Magn Reson. 2010; 204:327–332. [PubMed: 20378380]

[177]. Takeda K, Tabuchi Y, Negoro M. Active compensation of rf-pulse transients. J Magn Reson. 197:242–244. (n.d.). [PubMed: 19121594]

[178]. Lamley JM, Lougher MJ, Sass HJ, Rogowski M, Grzesiek S, Lewandowski JR. Unraveling the complexity of protein backbone dynamics with combined 13C and 15N solid--state NMR relaxation measurements. Phys Chem Chem Phys. 2015; doi: 10.1039/C5CP03484A

[179]. Franks W, Zhou D, Wylie B, Money B, Graesser D, Frericks H, Sahota G, Rienstra C. Magic-angle spinning solid-state NMR spectroscopy of the beta 1 immunoglobulin binding domain of protein G (GB1): N-15 and C-13 chemical shift assignments and conformational analysis. J Am Chem Soc. 2005; 127:12291–12305. DOI: 10.1021/ja044497e [PubMed: 16131207]

[180]. Mollica L, Baias M, Lewandowski JR, Wylie BJ, Sperling LJ, Rienstra CM, Emsley L, Blackledge M. Atomic-Resolution Structural Dynamics in Crystalline Proteins from NMR and Molecular Simulation. J. Phys. Chem. Lett. 2012; :3657–3662. DOI: 10.1021/jz3016233 [PubMed: 26291002]

[181]. Giraud N, Blackledge M, Goldman M, Böckmann A, Lesage A, Penin F, Emsley L. Quantitative analysis of backbone dynamics in a crystalline protein from nitrogen-15 spin-lattice relaxation. J Am Chem Soc. 2005; 127:18190–18201. DOI: 10.1021/ja055182h [PubMed: 16366572]

[182]. Chevelkov V, Xue Y, Linser R, Skrynnikov NR, Reif B. Comparison of Solid-State Dipolar Couplings and Solution Relaxation Data Provides Insight into Protein Backbone Dynamics. J Am Chem Soc. 2010; 132:5015–5017. DOI: 10.1021/ja100645k [PubMed: 20297847]

[183]. Xue Y, Skrynnikov NR. Ensemble MD simulations restrained via crystallographic data: accurate structure leads to accurate dynamics. Protein Sci. 2014; 23:488–507. DOI: 10.1002/pro.2433 [PubMed: 24452989]

[184]. Thomas L, Kahr J, Schmidt P, Krug U, Scheidt HA, Huster D. The dynamics of the G protein-coupled neuropeptide Y2 receptor in monounsaturated membranes investigated by solid-state NMR spectroscopy. J Biomol NMR. 2015; doi: 10.1007/s10858-014-9892-5

[185]. Good DB, Wang S, Ward ME, Struppe J, Brown LS, Lewandowski JR, Ladizhansky V. Conformational Dynamics of a Seven Transmembrane Helical Protein Anabaena Sensory Rhodopsin Probed by Solid-State NMR. J Am Chem Soc. 2014; 140205071110008. doi: 10.1021/ja411633w

[186]. Scheidt HA, Morgado I, Rothemund S, Huster D. Dynamics of amyloid β fibrils revealed by solid-state NMR. J Biol Chem. 2012; 287:2017–2021. DOI: 10.1074/jbc.M111.308619 [PubMed: 22130659]

[187]. Lange A, Gattin Z, Van Melckebeke H, Wasmer C, Soragni A, van Gunsteren WF, Meier BH. A combined solid-state NMR and MD characterization of the stability and dynamics of the HET-s(218-289) prion in its amyloid conformation. ChemBioChem. 2009; 10:1657–1665. DOI: 10.1002/cbic.200900019 [PubMed: 19504509]

[188]. Chou J, Case D, Bax A. Insights into the mobility of methyl-bearing side chains in proteins from (3)J(CC) and (3)J(CN) couplings. J Am Chem Soc. 2003; 125:8959–8966. DOI: 10.1021/ja029972s [PubMed: 12862493]

[189]. Ma P, Xue Y, Coquelle N, Haller JD, Yuwen T, Ayala I, Mikhailovskii O, Willbold D, Colletier J-P, Skrynnikov NR, Schanda P. Observing the overall rocking motion of a protein in a crystal. Nat Commun. 2015; 6:8361.doi: 10.1038/ncomms9361 [PubMed: 26436197]

[190]. Massi F, Grey M, Palmer AG. Microsecond timescale backbone conformational dynamics in ubiquitin studied with NMR R-1p relaxation experiments. Protein Sci. 2005; 14:735–742. DOI: 10.1110/ps.041139505 [PubMed: 15722448]

[191]. Salvi N, Ulzega S, Ferrage F, Bodenhausen G. Time scales of slow motions in ubiquitin explored by heteronuclear double resonance. J Am Chem Soc. 2012; 134:2481–2484. DOI: 10.1021/ja210238g [PubMed: 22206505]

[192]. Hansen DF, Feng H, Zhou Z, Bai Y, Kay LE. Selective characterization of microsecond motions in proteins by NMR relaxation. J Am Chem Soc. 2009; 131:16257–16265. DOI: 10.1021/ja906842s [PubMed: 19842628]

Europe PMC Funders Author Manuscripts

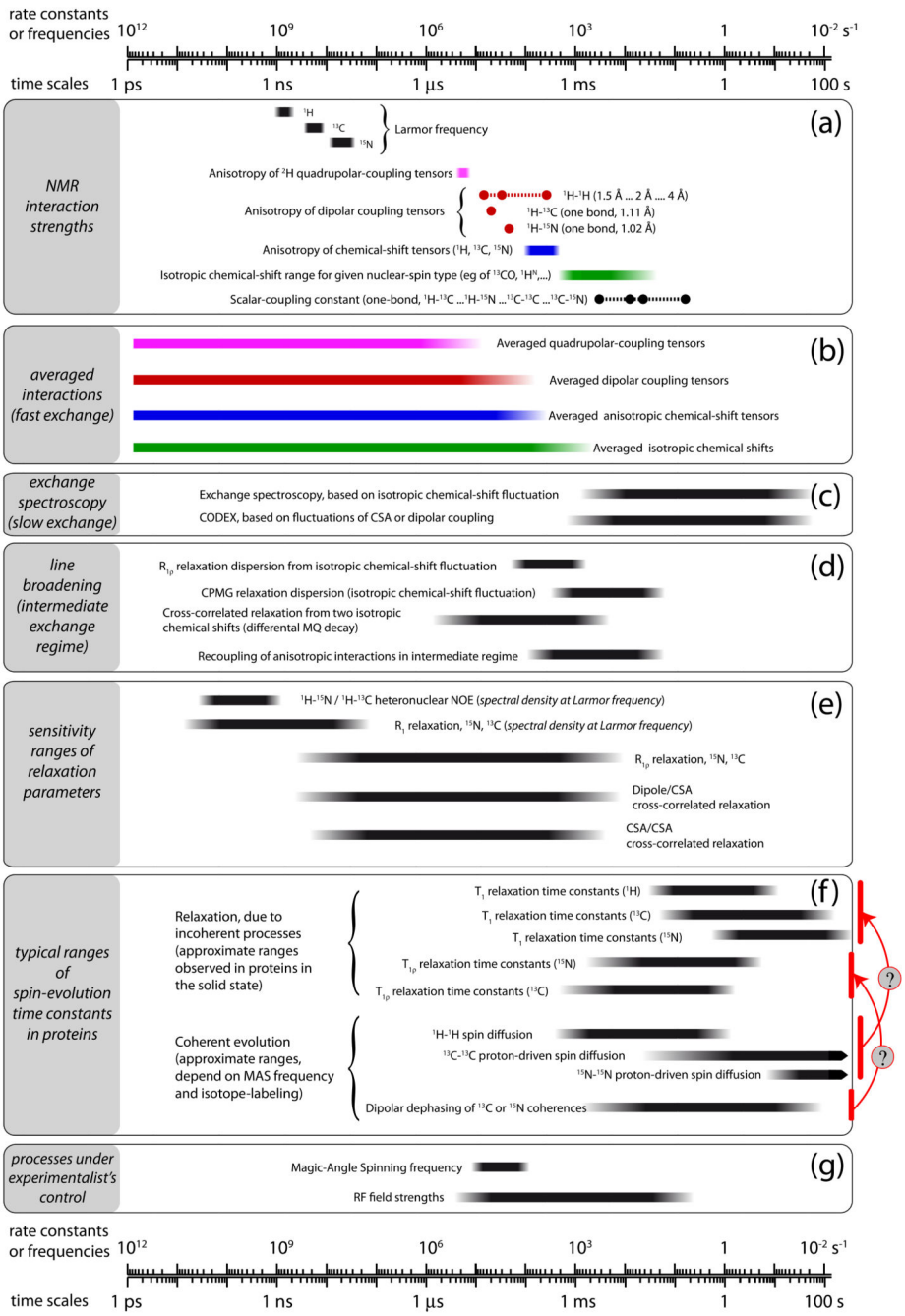

Figure 1.

Interactions in NMR spectroscopy, NMR observables probing molecular motion, and time-dependence of NMR parameters. (a) Interactions in NMR and their respective interaction strengths (in Hz), top of figure. (b) The time scales over which these interactions are averaged; for dynamics occurring on at a rate higher than the interaction strength (in Hz), the observed interaction strength is the average over the sample conformations (“fast” regime). (c) Methods for detecting dynamic process that are slow compared to the interaction strength (“slow” regime). (d) Methods for probing “intermediate” regime dynamics. (e) Time scales

probed by spin relaxation measurements (upper two: longitudinal relaxation; lower two: transverse relaxation). (f) Typical time scales of changes of the density operator; the evolution of the spin states can be due to either relaxation processes (due to stochastic motion), or due to deterministic processes (i.e. non-stochastic processes). In order to quantitatively measure relaxation parameters, one has to ensure that the coherent evolution is negligible compared to the dynamics-induced evolution (as marked with question marks here). (g) Time scales of magic-angle spinning and typical spin nutation frequencies under RF fields.

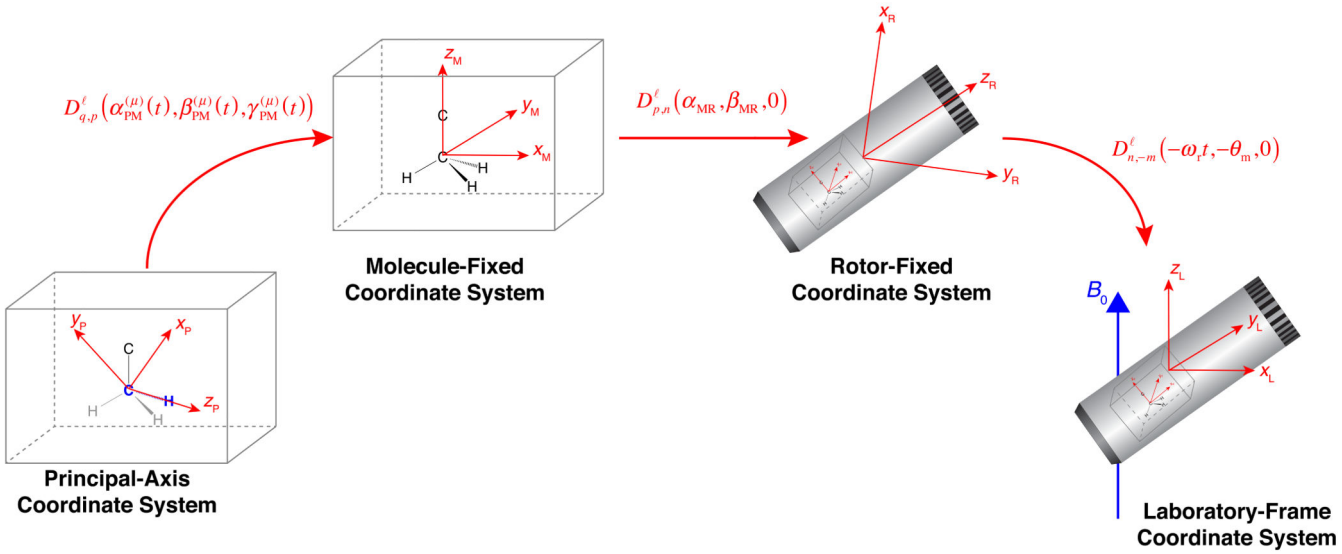

Figure 2.

Coordinate systems and rotations required for the transformation of the space tensor of an NMR interaction from the principal-axis system into the laboratory-frame coordinate system for the example of a C-H dipolar coupling in a CH_3 group.

Europe PMC Funders Author Manuscripts

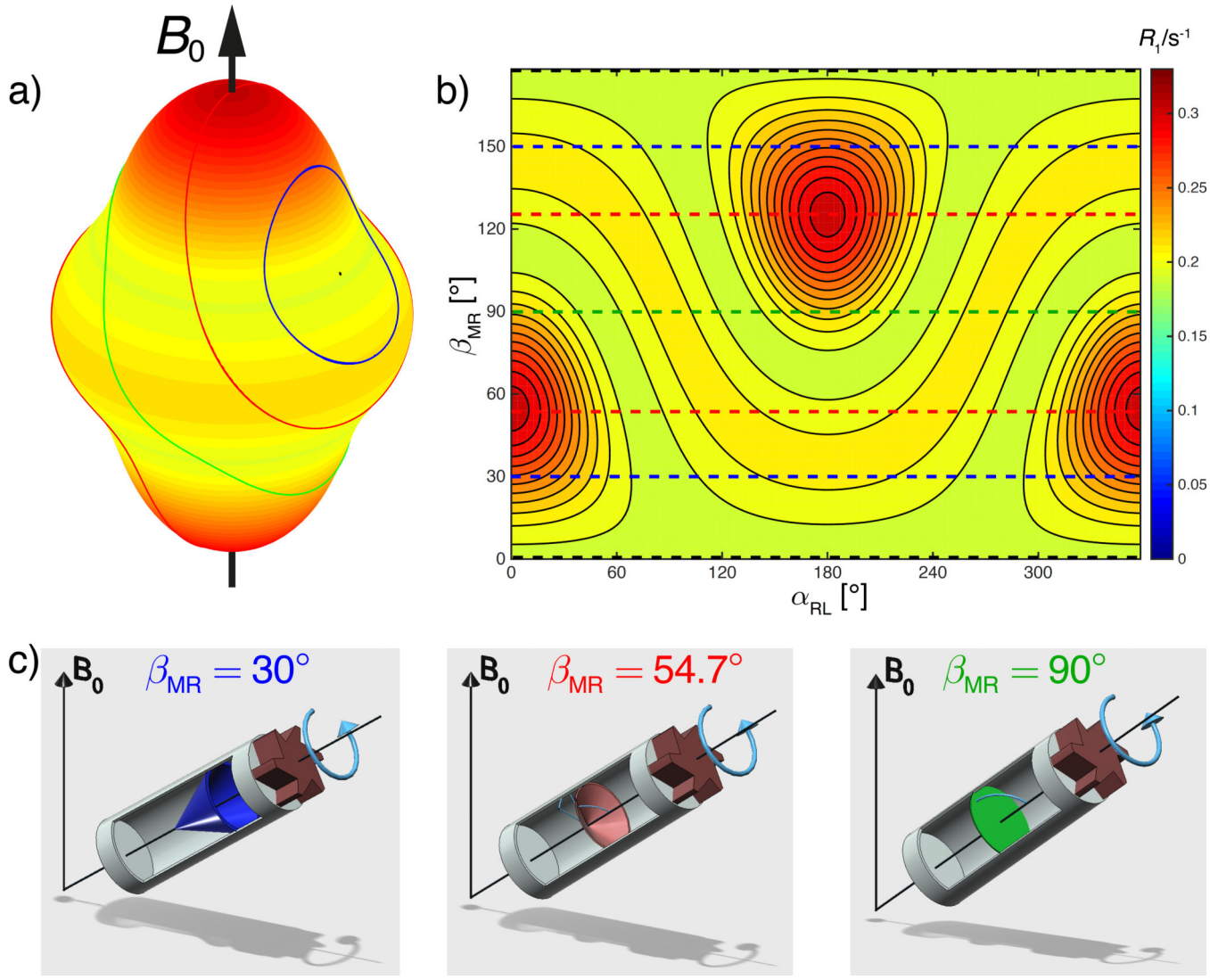

Figure 3.

a) Plot of the magnitude of the T_1 relaxation rate constants in a static solid as a function of the crystallite orientation for a model of restricted rotational diffusion (dipolar relaxation in a NH spin system, $\theta = 45°$, $D_w = 2.525\ 10^6$ s, 500 MHz). Plotted on top of the tensor are MAS trajectories (for different angles β_{MR}) that show the partial averaging of the T_1 relaxation-rate constants by MAS. b) The contour plot on the right-hand side shows the dependence of the relaxation-rate constant under MAS on the rotor angle $\alpha_{RL}(t) = -\omega_r t$ and β_{MR}. The trajectories are indicated by dashed lines. c) The lower three panels show as cones the trajectories along which a given tensor, aligned at an angle of β_{MR} (three different values, as indicated).

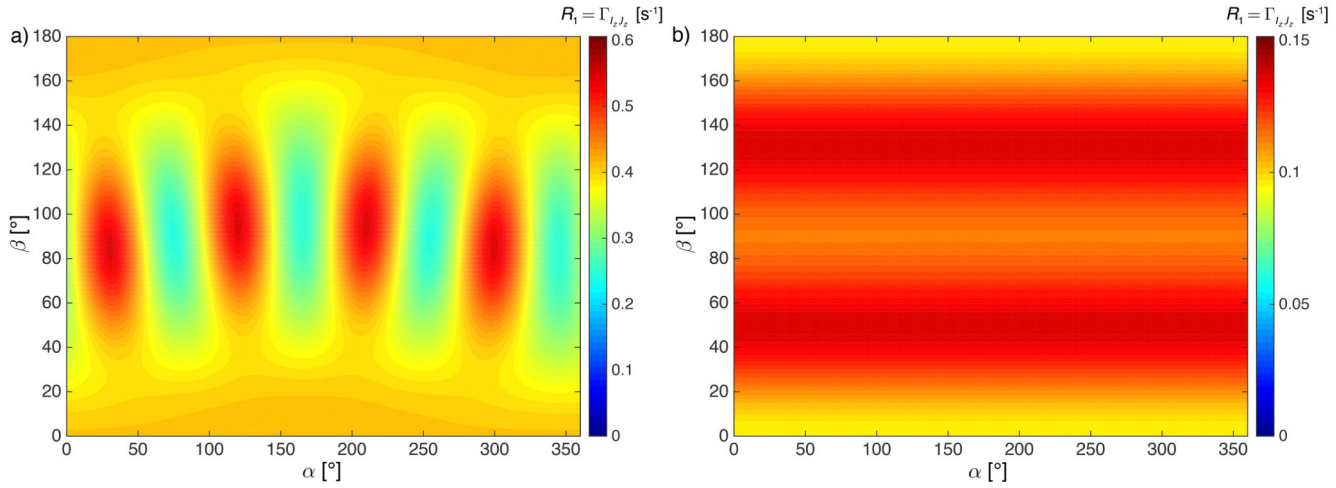

Figure 4.

R_1 as a function of α and β for a N-H spin system ($\delta_D/2\pi$ = 22954 Hz, $\delta_{CSA}/2\pi$ = 6867 Hz) at 600 MHz: a) two-site jump model (τ_c = 1 ns, γ_0 = 30°) and b) a restricted-rotational diffusion model ($D_w = 2\ 10^6\ s^{-1}$, θ = 30°).

Europe PMC Funders Author Manuscripts

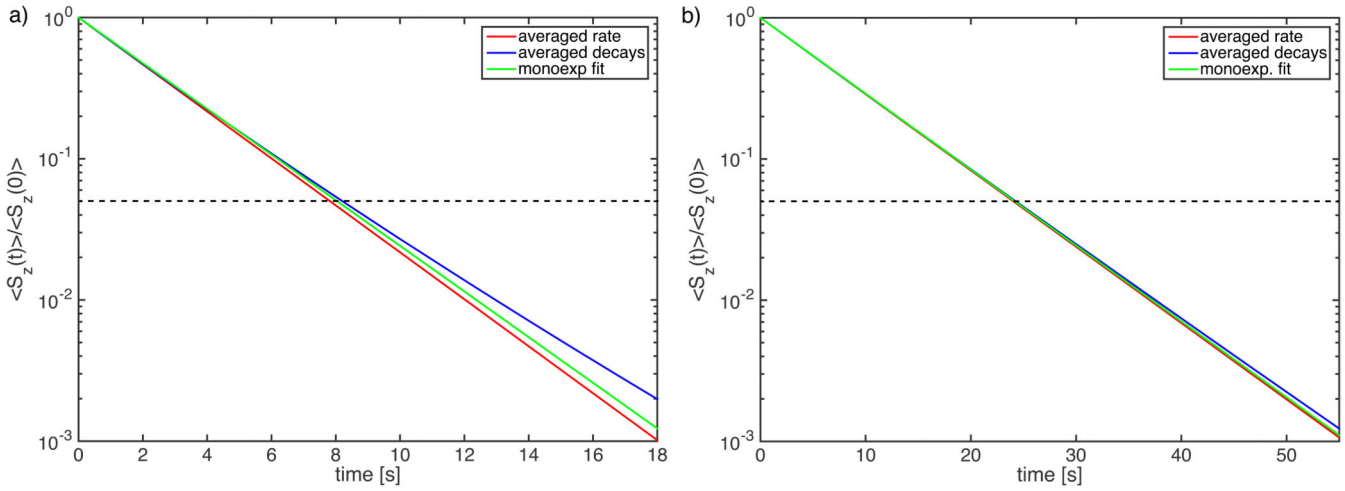

Figure 5.

Simulated decay of the magnetization in a powder using averaged decays (blue) and approximations using averaged rate constants (red) and a mono-exponential fit (green) of the powder-averaged decays up to a value of 5% of the initial intensity for a) a two-site jump model and b) a restricted rotational diffusion model with the same parameters as in Fig. 4. The black dashed line indicates the cut-off value used in the fitting of the rate constants.

Europe PMC Funders Author Manuscripts

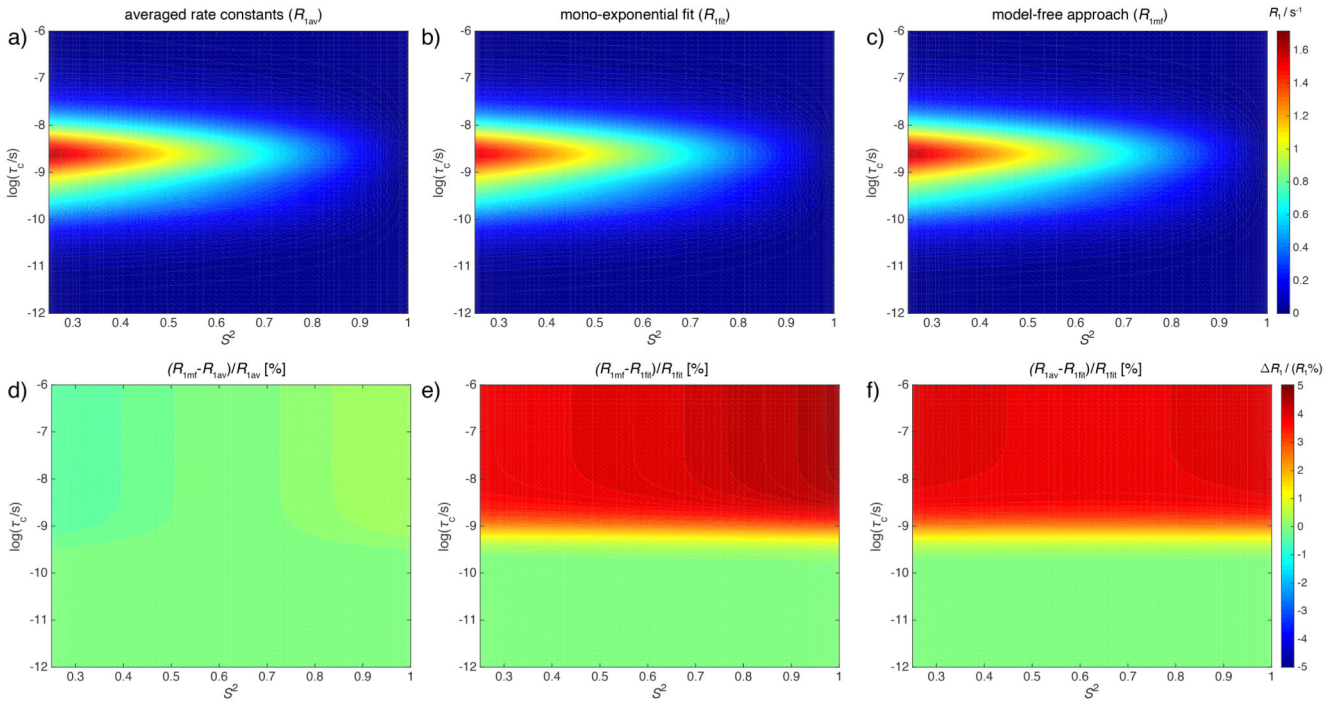

Figure 6.

Plot of the longitudinal ^{15}N relaxation-rate constant for a two-site jump model and dipolar relaxation at a static magnetic field of 14.1 T (corresponding to a ^{1}H resonance frequency 600 MHz) as a function of the correlation time τ_c and the jump angle θ. a) Powder-averaged rate constant for a two-site jump model, b) mono-exponential fit of the averaged decays for a two-site jump model, and c) model-free calculation. The relative differences between the powder-averaged rate constants and the model-free calculations are shown in d) while e) shows the relative difference between the mono-exponential fits and the model-free rate constants. f) Relative difference between the averaged rate constants and the mono-exponential fits.

Europe PMC Funders Author Manuscripts

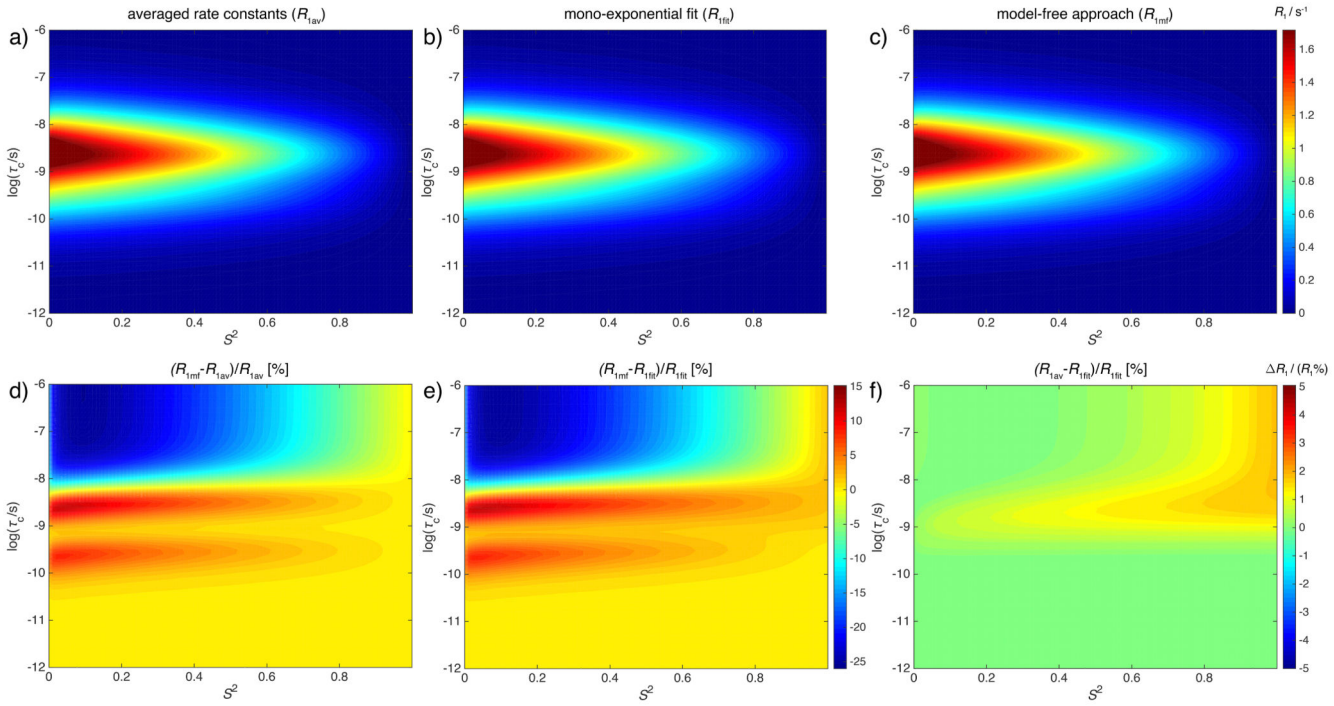

Figure 7.

Plot of the longitudinal ^{15}N relaxation-rate constant for a restricted rotational-diffusion in a cone model and dipolar relaxation at a static magnetic field of 14.1 T (corresponding to a ^{1}H resonance frequency 600 MHz) as a function of the correlation time τ_c and the cone opening angle θ. a) Powder-averaged rate constant for the wobbling-in-a-cone model, b) mono-exponential fit of the averaged decays for the wobbling-in-a-cone model, and c) model-free calculation. The relative differences between the powder-averaged rate constants and the model-free calculations are shown in d) while e) shows the relative difference between the mono-exponential fits and the model-free rate constants. f) Relative difference between the averaged rate constants and the mono-exponential fits.

Europe PMC Funders Author Manuscripts

Europe PMC Funders Author Manuscripts

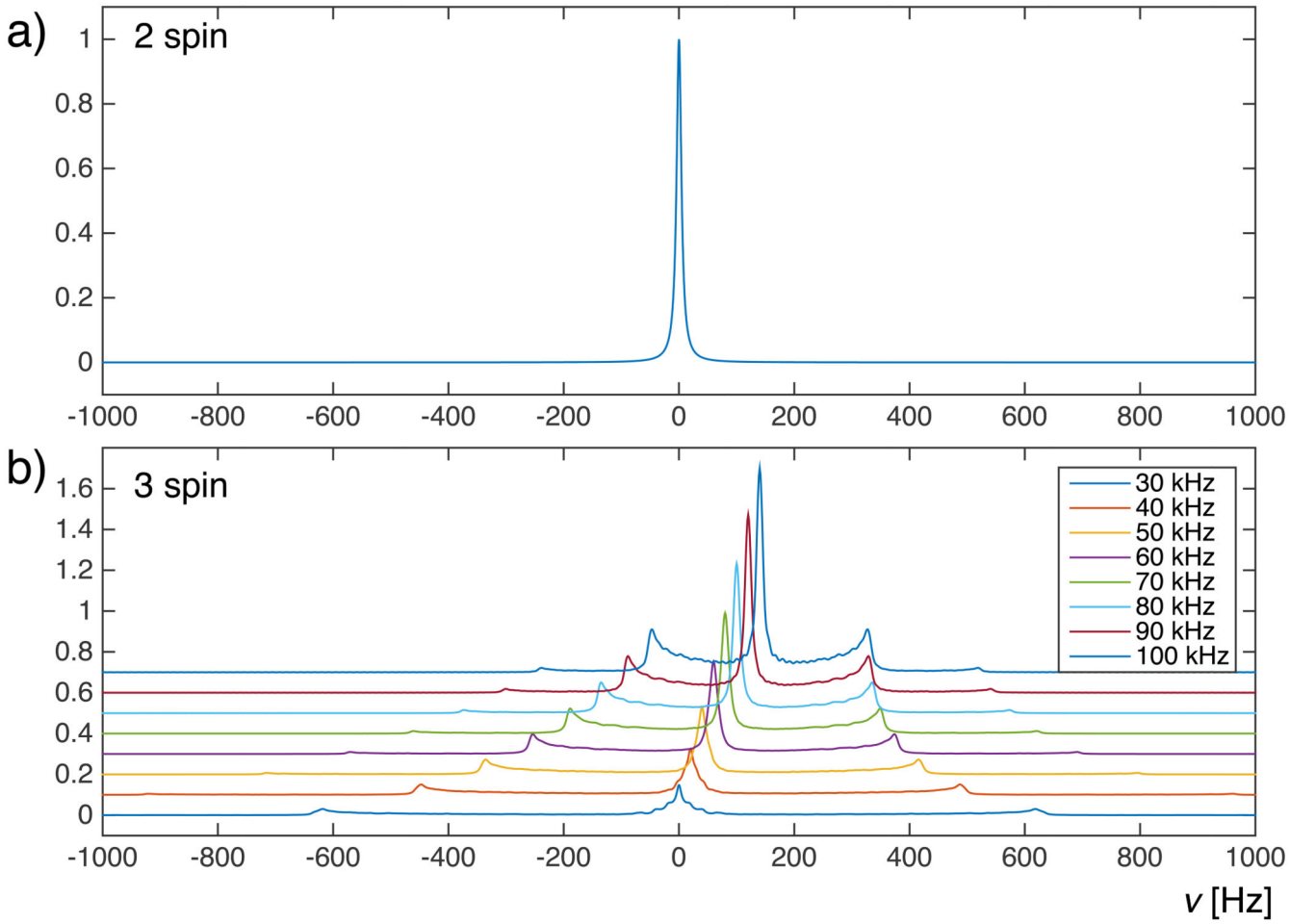

Figure 8.

Simulation of the MAS spectrum of a proton spin system consisting of (a) 2 and (b) 3 protons with identical chemical shifts and dipolar couplings of 10 kHz between all protons as a function of spinning frequency. The spectrum of the two-spin system is independent of the spinning frequency. The spectra have been horizontally shifted to improve the visibility.

Europe PMC Funders Author Manuscripts

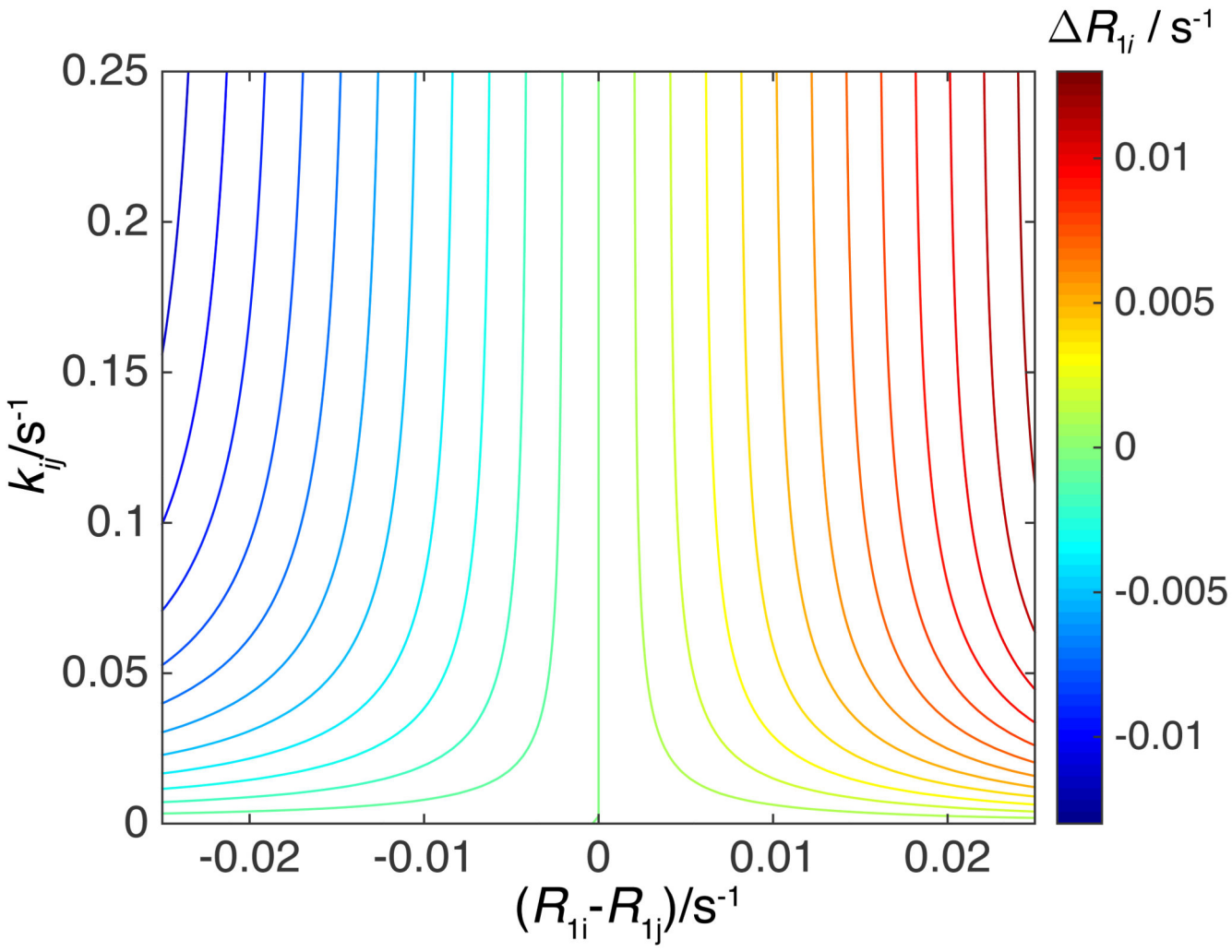

Figure 9.

Plot of the changes in the longitudinal relaxation-rate constant $R_{1i} = 0.05\ s^{-1}$ as a function of the difference of the two relaxation-rate constants R_{1i} and R_{1j} and the spin-diffusion rate constant k_{ij} (see Eqs. (32) and (33)). This clearly shows that for reliable results, the spin-diffusion rate constant must significantly smaller than the difference of the two relaxation-rate constants.

Europe PMC Funders Author Manuscripts

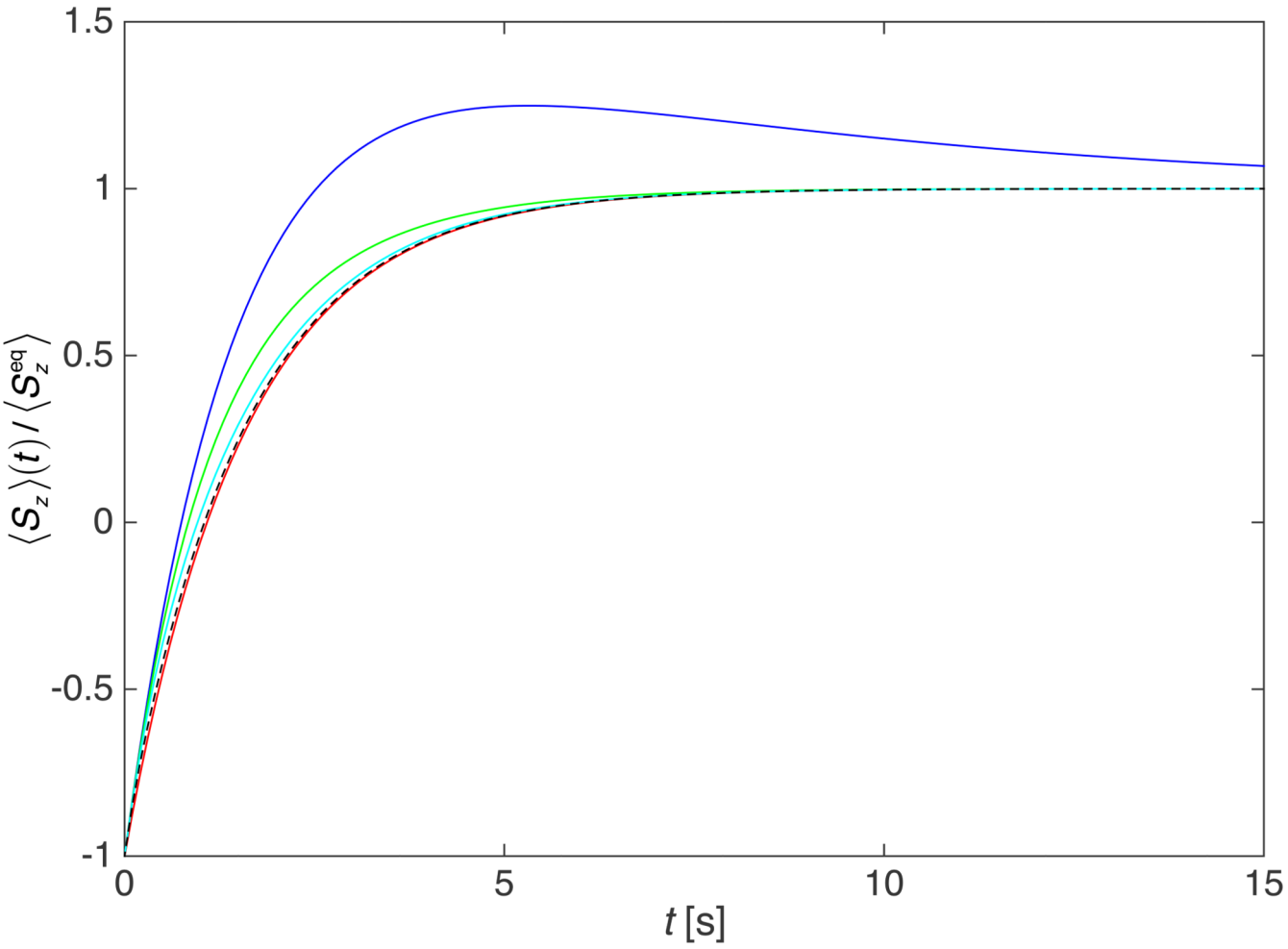

Figure 10.

Time evolution of the inverted ^{15}N polarization in a N-H two-spin system at 600 MHz Larmor frequency under restricted rotational diffusion with $D_w = 10^8$ s^{-1} and $\theta = 40°$ leading to $T_{1H} = 5.3$ s, $T_{1N} = 1.6$ s and $\Gamma_{HN} = 0.11$ s^{-1}. The red line shows the mono-exponential decay with the time constant of T_{1N} while the blue one shows the multi-exponential decay obtained from the system of coupled differential equations of Eq. (34). Increasing the ^{1}H auto-relaxation rate constant by 1 s^{-1} and 3 s^{-1} leads to the decay shown in green and cyan, respectively. An increase to 10 s^{-1} leads to the black dashed line that is almost equivalent to the mono-exponential decay shown in red.

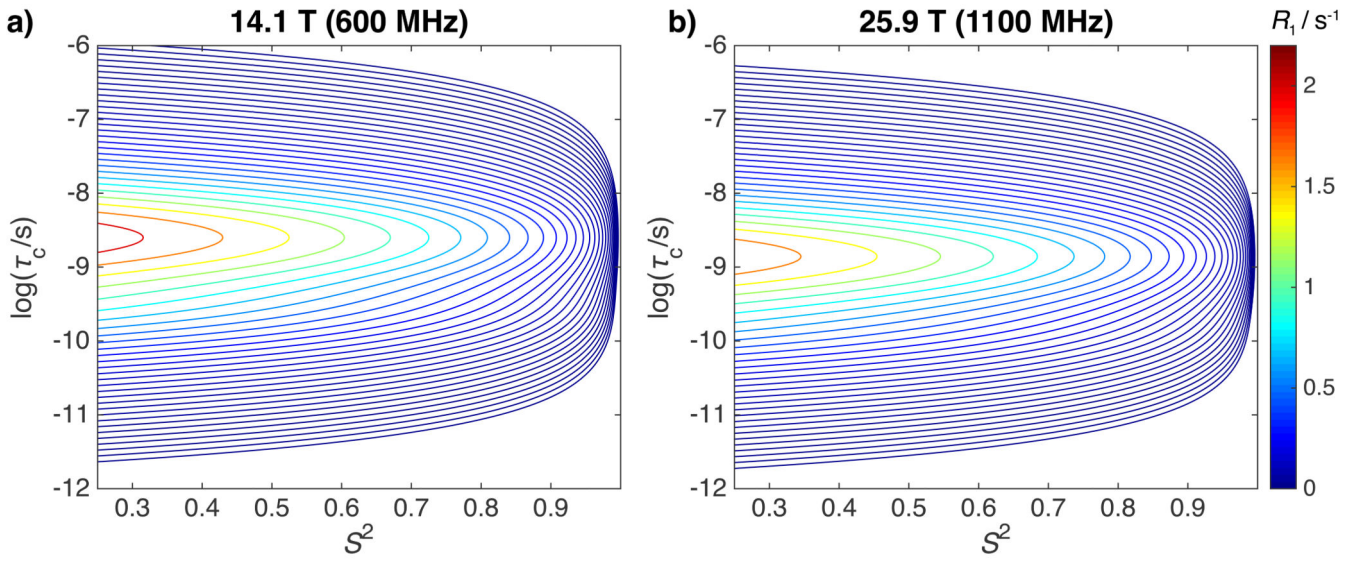

Figure 11.

Dependence of $R_1 = 1/T_1$ on the correlation time and the order parameter for a single time-scale model-free approach for an H-N two spin system at (a) 600 MHz and (b) 1100 MHz proton Larmor frequency. The anisotropy of the dipolar coupling was assumed to be $\delta_{NH} / 2\pi = 22954$ Hz and the anisotropy of the axially-symmetric CSA tensor $\delta_N / 2\pi = 113$ ppm.

Europe PMC Funders Author Manuscripts

Europe PMC Funders Author Manuscripts

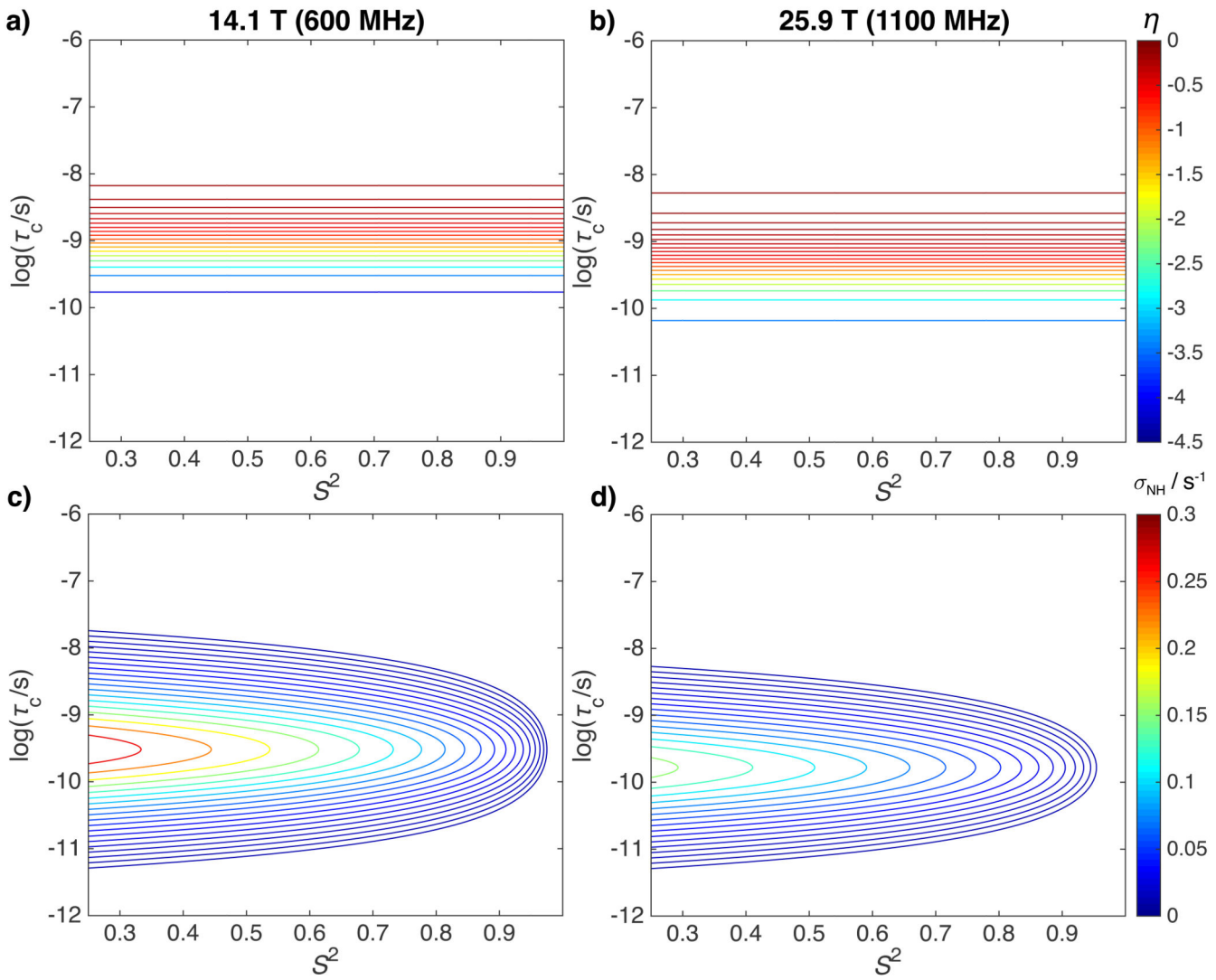

Figure 12.

Dependence of the steady-state NOE η and the cross-relaxation rate constant $\sigma_{NH} = \Gamma_{I_z,S_z}$ on the correlation time and the order parameter for a simple single time-scale model-free approach for an H-N two spin system. (a) η at 600 MHz and (b) η at 1100 MHz, (c) σ_{NH} at 600 MHz and (d) σ_{NH} at 1100 MHz proton Larmor frequency. The anisotropy of the dipolar coupling was assumed to be $\delta_{NH} / 2\pi = 22954$ Hz.

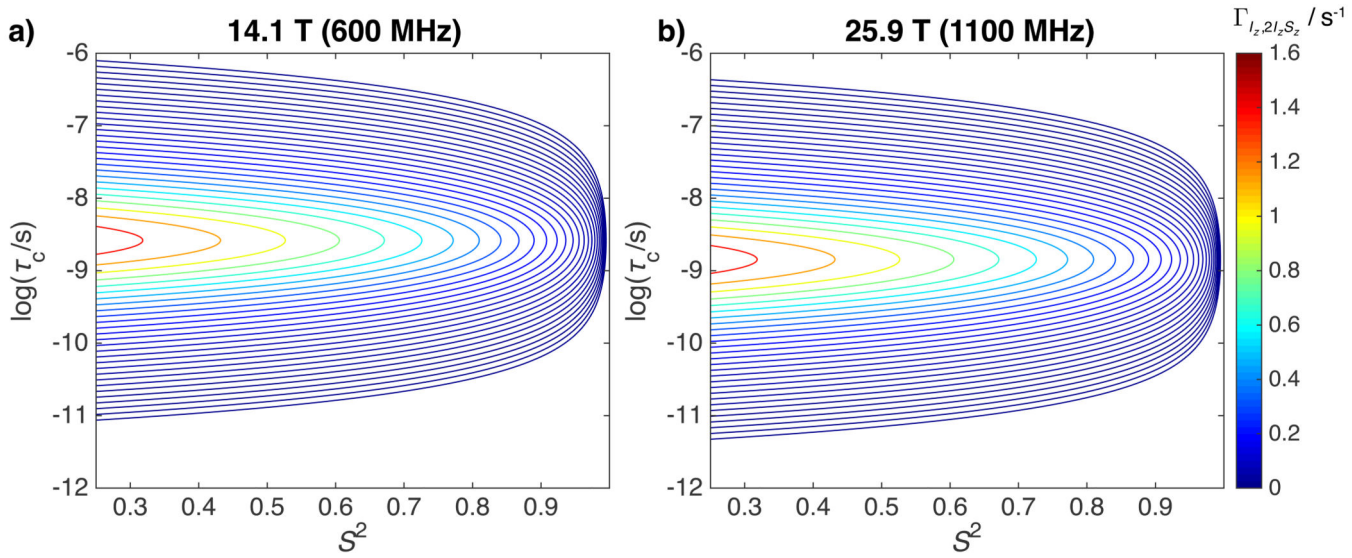

Figure 13.

Dependence of the dipolar/CSA cross-correlated cross-relaxation rate constant $\Gamma_{S_Z,2I_ZS_Z}$ on the correlation time and the order parameter for a simple single time-scale model-free approach for an H-N two spin system at (a) 600 MHz and (b) 1100 MHz proton Larmor frequency. The anisotropy of the dipolar coupling was assumed to be $\delta_{NH} / 2\pi = 22954$ Hz and the anisotropy of the axially-symmetric CSA tensor $\delta_N / 2\pi = 113$ ppm.

Europe PMC Funders Author Manuscripts

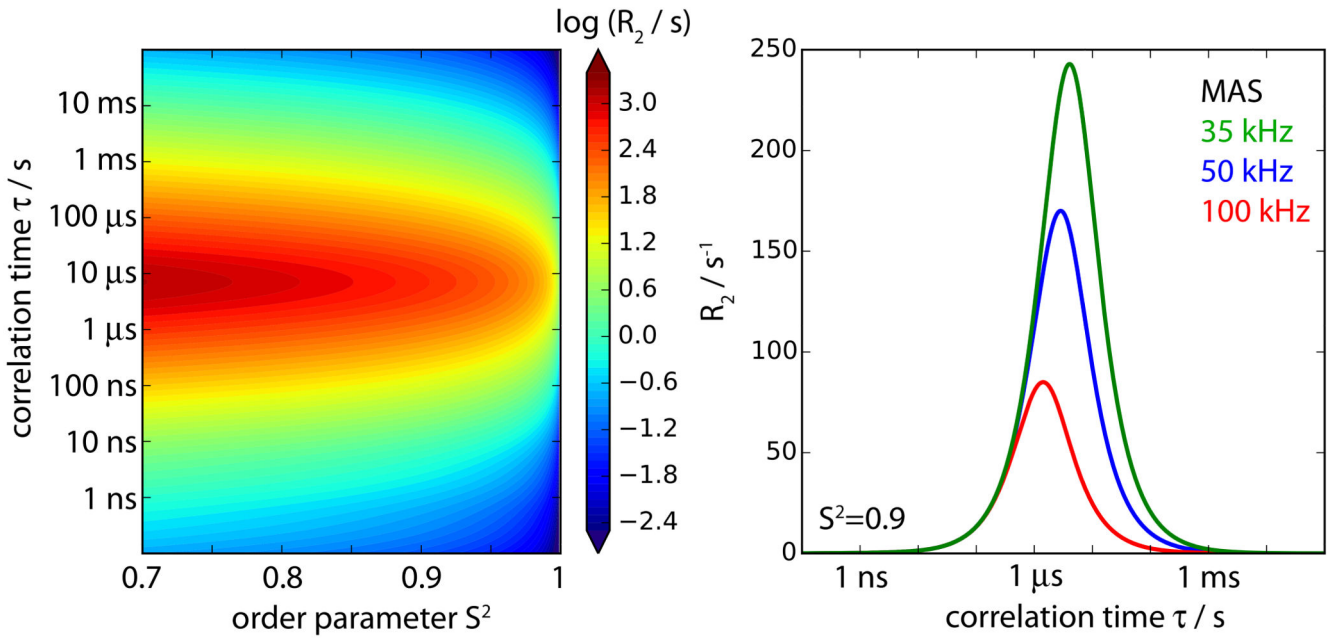

Figure 14.

^{15}N R_2 relaxation-rate constant, obtained from Eq. (46). In the contour plot on the left, a MAS frequency of 20 kHz was assumed; the right panel shows traces at an order parameter of $S^2 = 0.9$ for three MAS frequencies, as indicated. In all cases a magnetic field strength of 14.1 T was assumed.

Europe PMC Funders Author Manuscripts

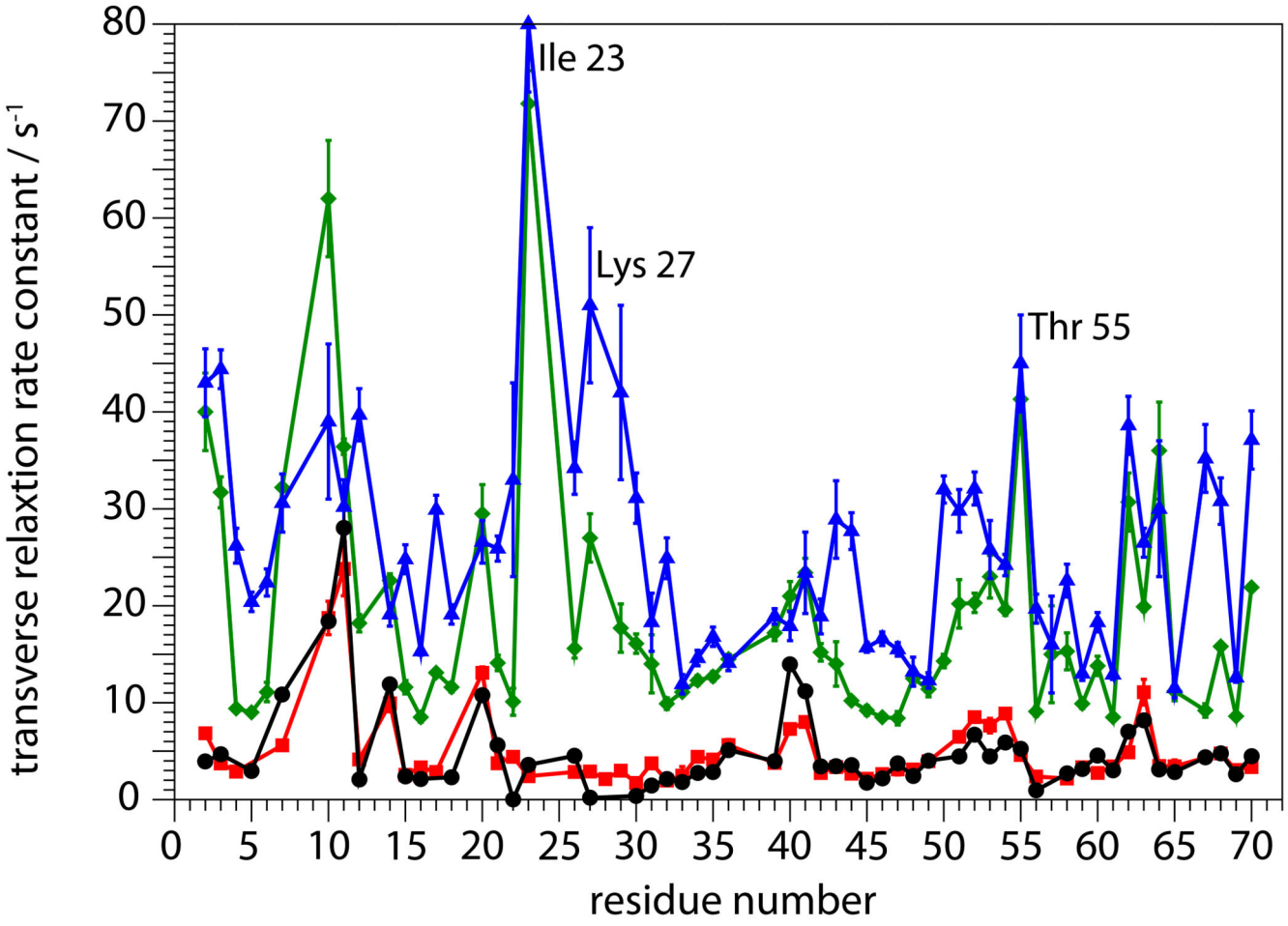

Figure 15.

^{15}N transverse decay rate constants in crystals of deuterated ubiquitin. The R_2' data set in blue was recorded on a perdeuterated sample, re-protonated on amide sites to 20%, at a MAS frequency of 57 kHz and a B_0 field strength of 19.9 T (850 MHz ^{1}H Larmor frequency). In this experiment, a simple delay – π pulse – delay sequence without any ^{1}H decoupling was used. In the data set in green, the same experimental conditions were chosen, but a 3.1 kHz WALTZ decoupling on ^{1}H was applied. The data set shown in red is the ^{15}N $R_{1\varrho}$ relaxation rate constant (on-resonance), which was measured at 39.5 kHz MAS frequency at a B_0 field strength of 14.1 T in the presence of a 15 kHz spin-lock RF field strength (without ^{1}H decoupling). The sample used for this measurement was perdeuterated at non-exchangeable sites, and re-protonated to 50% at exchangeable sites (prepared in a H_2O/D_2O mixture under conditions that allow full equilibration at all sites at the desired ratio). The data set in black is the predicted ^{15}N $R_{1\varrho}$ relaxation rate constant, which is based on amplitudes and time scales of amide motion, as obtained from a model-free fit [110]. For this latter, a set of up to six relaxation rate constants and the motional averaged H-N dipolar coupling anisotropy was used in a fit. The three residues indicated have been shown to undergo conformational exchange on a microsecond time scale, contributing the their transverse relaxation rate constants.

Europe PMC Funders Author Manuscripts

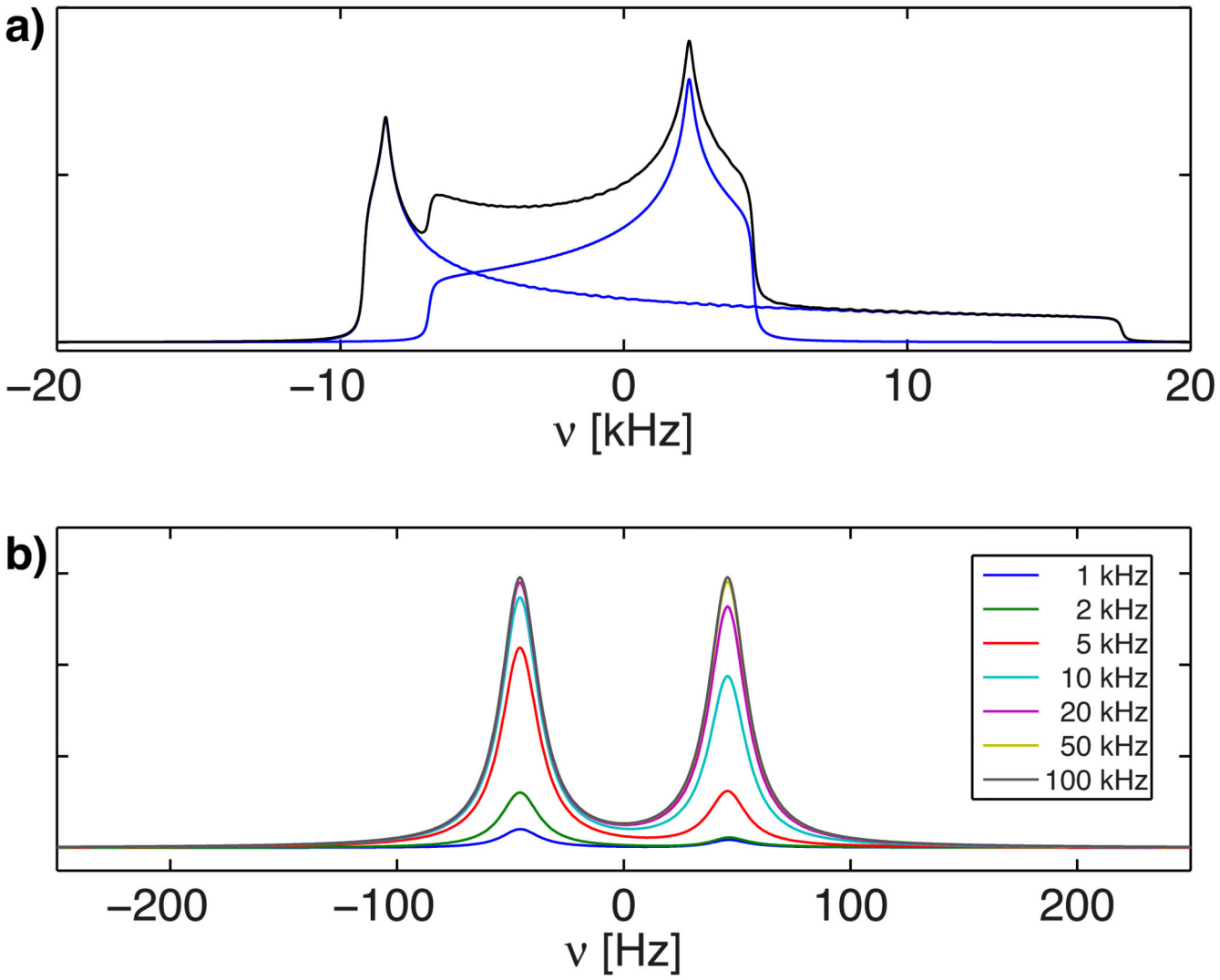

Figure 16.

a) Coherent contributions to the two ^{15}N multiplet lines from CSA/dipole interference at 600 MHz ^{1}H Larmor frequency in the static case. The dipolar coupling has an anisotropy of $\delta_{NH}/2\pi$ = 22954 Hz and the CSA tensor anisotropy is $\delta_{N}/2\pi$ = 6867 Hz pattern (black line) and the two multiplet lines (blue lines) corresponding to the proton spin in α and β state, respectively. b) shows the center band of the MAS manifold as a function of the spinning frequency (ν_r = 1, 2, 5, 10, 20, 50, 100 kHz, for color code see legend in figure). One can clearly see the intensity difference between the two multiplet lines at lower spinning frequencies due to the different width of the powder patterns. At MAS frequencies above 20 kHz the difference becomes small.

Europe PMC Funders Author Manuscripts

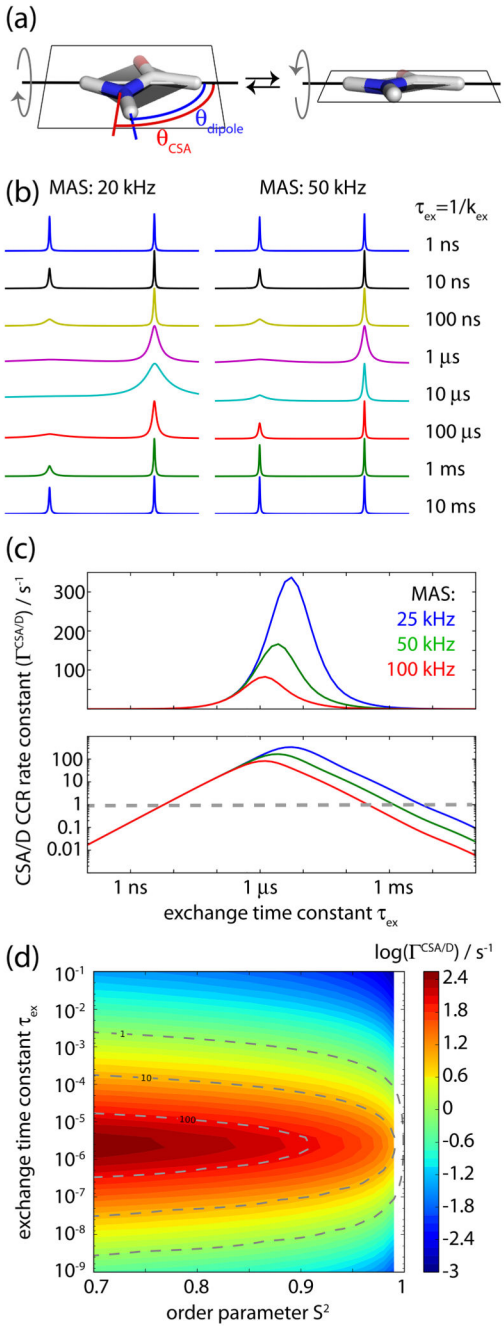

Figure 17.

^{1}H-^{15}N dipolar/^{15}N CSA cross-correlated relaxation, from numerical simulations. (a) Exchange model used for these simulations. The exchange occurs between two distinct states, in which the peptide plane is rotated along the C^{α}-C^{α} axis by an angle φ. The ^{1}H-^{15}N dipolar interaction (1.02 Å distance) is inclined with respect to this rotation axis by an angle θ_D = 77°, and the ^{15}N CSA tensor (assumed to be axially symmetric, with $\Delta\sigma$ = −170 ppm) is inclined by θ_{CSA} = 97°. The jump angle can be related to a generalized order parameter S^2 as $S2 = (1+3\cos^2\varphi)/4$. Panel (b) shows ^{15}N spectra resulting from free evolution of ^{15}N

coherence without 1H decoupling. The asymmetry of the line width of the doublet components is evident. Two different MAS frequencies are shown, as indicated. All spectra are normalized to the height of the larger peak. (c) Cross-correlated relaxation rate constant $\Gamma^{CSA/D}$ as a function of the jump time constant for three different MAS frequencies, as indicated. The lower plot is a logarithmic plot of the rate constant. The value of $\Gamma^{CSA/D} = 1\ s^{-1}$, which is the approximate detection limit. The exchange jump angle was assumed as $\theta = 26.5°$, corresponding to an order parameter $S^2 = 0.85$. Panel (d) shows Γ_{I^+, I^+S_z} as a function of the amplitude of motion and the time constant. The MAS frequency was set to 50 kHz.

Europe PMC Funders Author Manuscripts

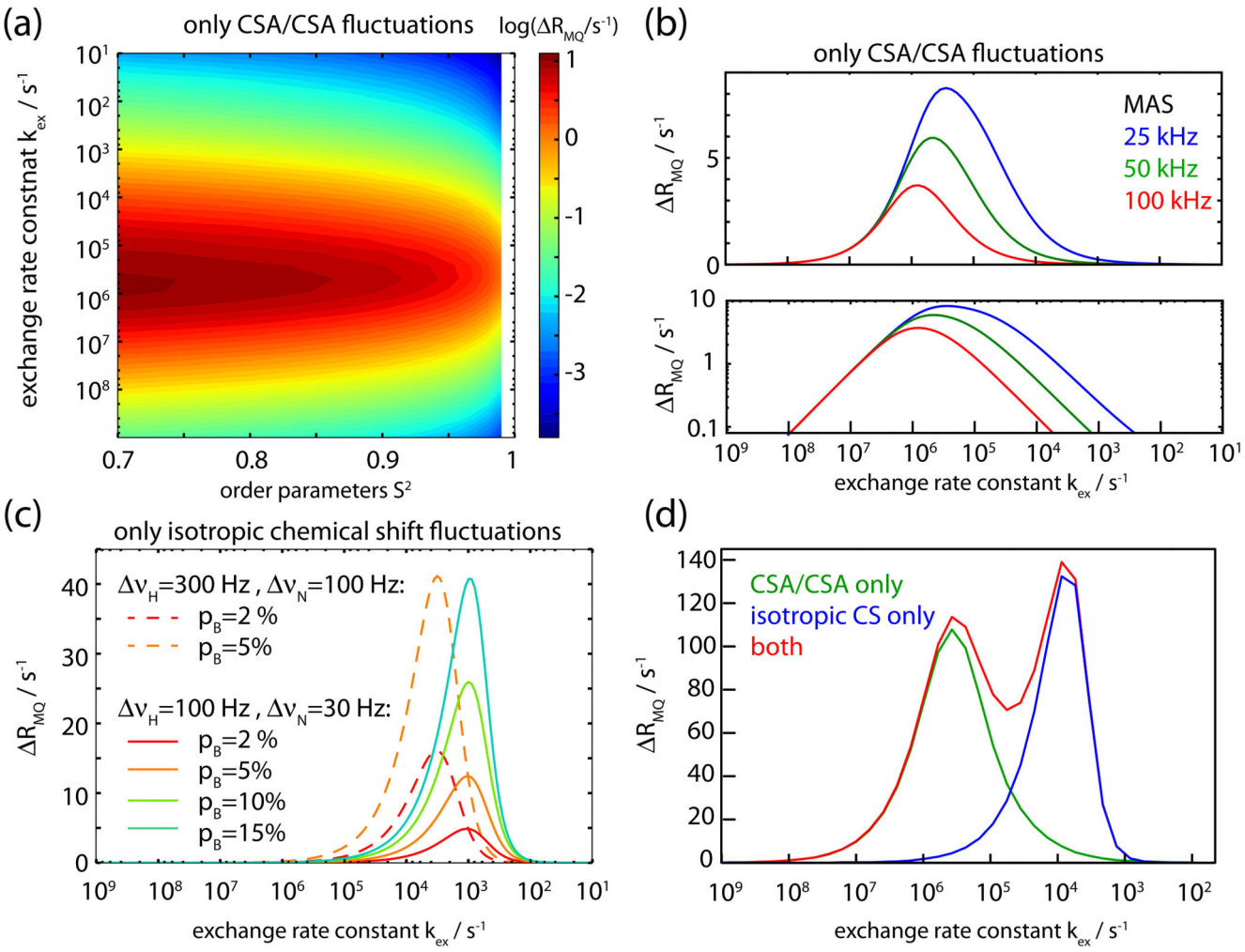

Figure 18.

Simulation of the differential DQ/ZQ relaxation, ΔR_{MQ}, The simulation assumed a two-site exchange model (the same as in Figure 17), in which the axially symmetric ^{15}N CSA tensor had a $\Delta\sigma$ = 6800 Hz (−170 ppm at 14.1 T), and the assumed axially symmetric ^{1}H CSA tensor had a $\Delta\sigma$ = 480 Hz. The ^{1}H CSA tensor was inclined relative to the ^{15}N tensor by 10 degrees. In this simulation we followed a previously employed experimental scheme in solution [132] in which the buildup of $2H_yN_y$ from $2H_xN_x$ is monitored. This buildup arises from differences in relaxation rate constants of ZQ and DQ coherences, as can easily be verified by expressing these product operators in raising/lowering operator basis. The differential relaxation rate constant ΔR_{MQ} can be obtained from $\langle 2H_yN_y\rangle/\langle 2H_xN_x\rangle = \tanh(\Delta R_{MQ}\, t/2)$. Panel (a) shows the differential relaxation rate constant ΔR_{MQ} as a function of time scale and amplitude of the motion, assuming that all isotropic chemical shifts are equal in the two states. The jump angle was converted to an order parameter S^2 as $S^2 = (1+3\cos^2\varphi)/4$. Panel (b) shows the MAS dependency of ΔR_{MQ} as a function of the time scale of motion, for a jump amplitude of $\varphi = 5°$. In both (a) and (b) we assumed that the isotropic chemical shift is identical in the two exchanging states, and that the two states are populated equally. In panel (c) it is assumed that the two CSA tensors and the dipolar coupling are

unchanged by the exchange process, and the isotropic chemical shifts of ^{1}H and ^{15}N vary. Two different assumptions about the $\Delta\omega$ values and different relative populations show the MAS dependence of ΔR_{MQ}, due to CSA/CSA modulation. Panel (d) shows a general case, which involves fluctuation of both the isotropic and anisotropic components of the two chemical shifts. Here $\Delta\sigma_{15N}$ = 6800 Hz, $\eta_{CSA,15N}$ = 0, $\Delta\sigma_{1H}$ = 3600 Hz, $\eta_{CSA,1H}$ = 0.9 and the exchange occurred between two states (90%/10% population) in which the orientations of the tensors are inclined by 30°, and the isotropic chemical shift changes are $\Delta\nu_{15N}$ = 160 Hz, $\Delta\nu_{1H}$ = 800 Hz.

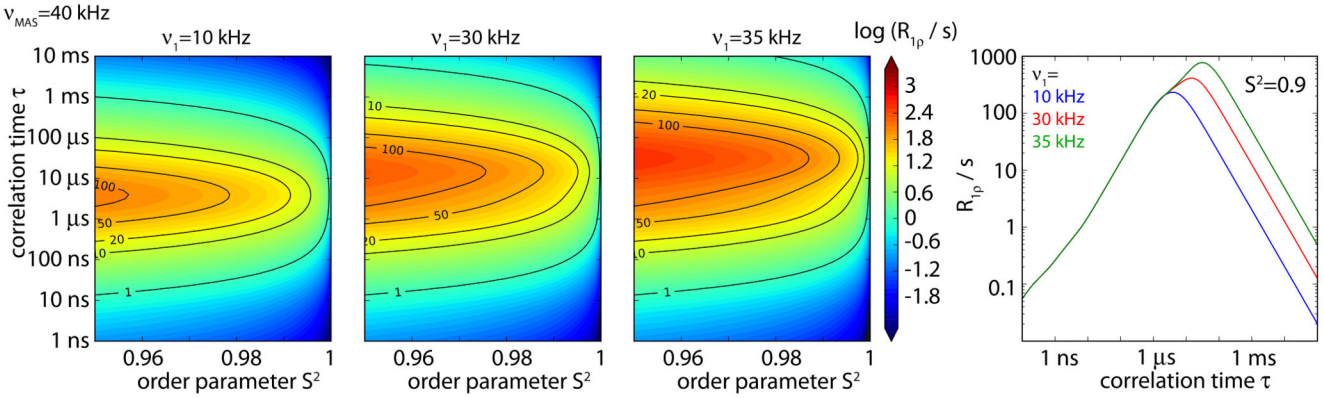

Figure 19.

^{15}N $R_{1\varrho}$ rate constants for a MAS frequency of 40 kHz and three different RF-field amplitudes, 10 kHz, 30 kHz and 35 kHz. The data were calculated based on the analytical expressions (Eq. (53)) derived within the Redfield-theory framework. The ^{15}N CSA was set to 6800 Hz and the dipolar coupling to 22.9 kHz (1.02 Å distance).

Europe PMC Funders Author Manuscripts

Europe PMC Funders Author Manuscripts

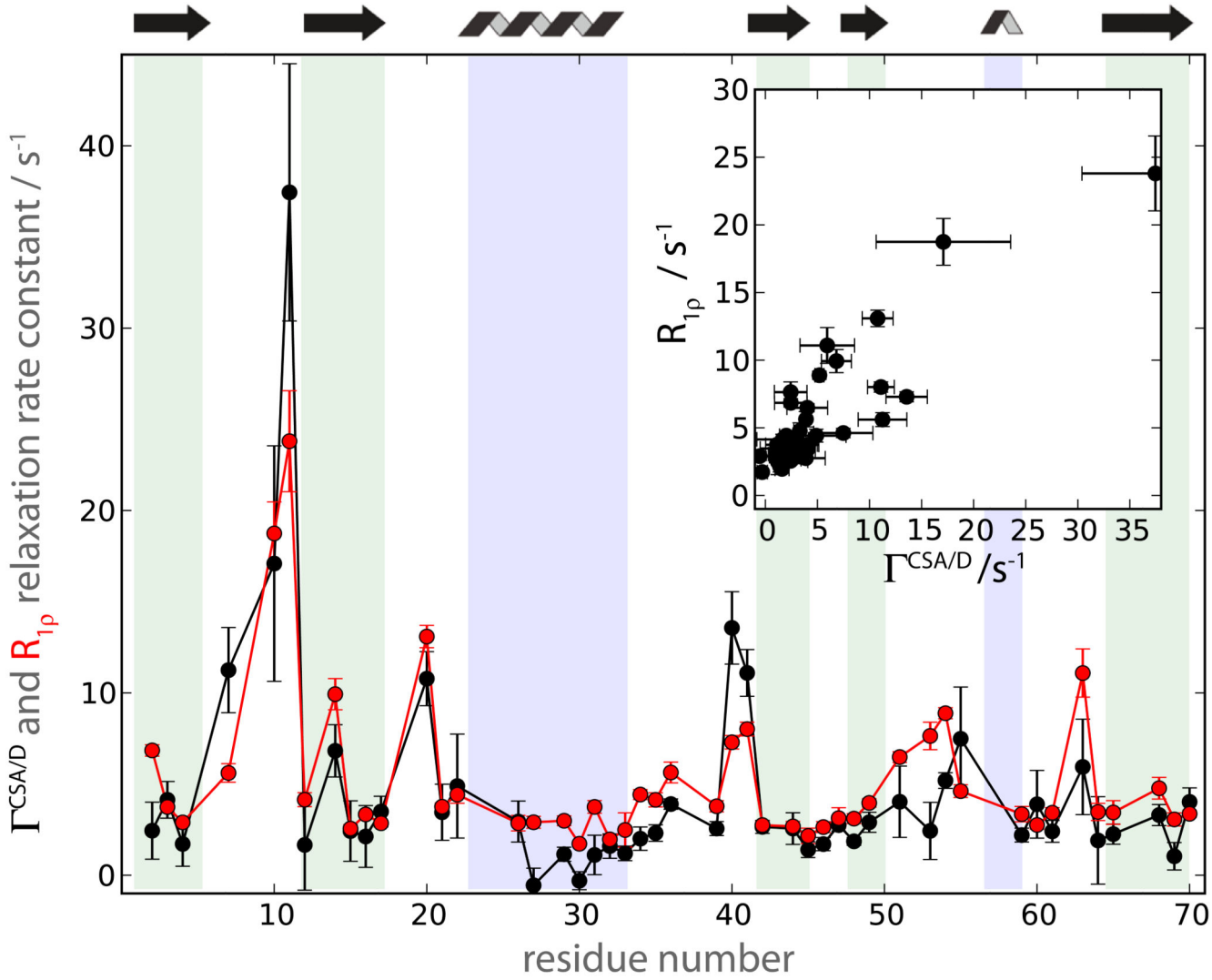

Figure 20.

Comparison of two different ^{15}N relaxation rate constants, measured in deuterated ubiquitin at fast MAS. Shown in red and black are the ^{15}N $R_{1\varrho}$ (at 39 kHz MAS and 15 kHz spin-lock) and the ^{1}H-^{15}N dipolar/^{15}N CSA cross-correlated relaxation [98], respectively. The insert shows a correlation between these two.

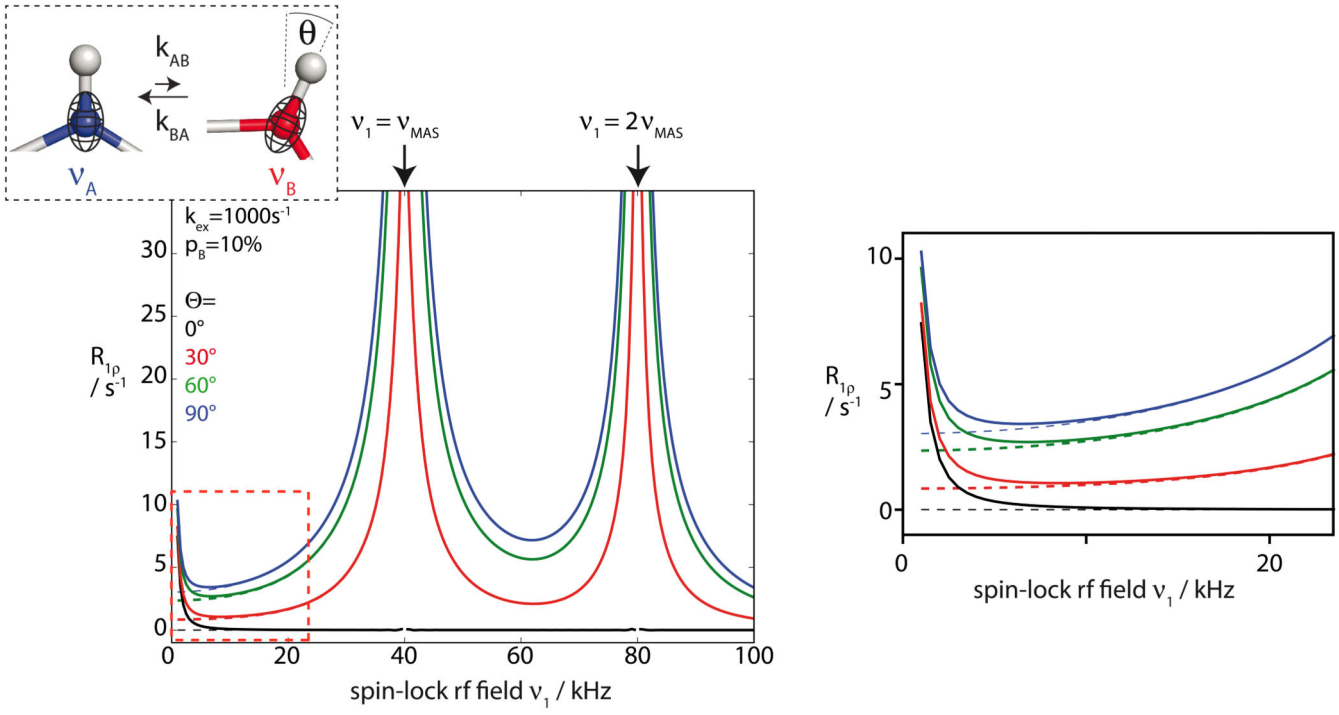

Figure 21.

Conformational exchange as seen by ^{15}N $R_{1\varrho}$ relaxation-dispersion experiments under MAS, obtained by stochastic Liouville simulations. An exchange between two states is assumed populated to 90% and 10% respectively, and differing in the bond orientation (CSA, dipole), and the ^{15}N isotropic chemical shift ($\Delta\nu$ = 300 Hz). Different jump angles are simulated, as shown in the figure, and the exchange rate was 1000 s^{-1}. The MAS frequency was 40 kHz, and the B_0 field strength was 14.1 T. The red dashed area is shown in a zoom view on the right. Dashed curves show the case in which the isotropic chemical shift difference between the two states is zero, i.e. where only fluctuations of the anisotropic interactions occur.

Europe PMC Funders Author Manuscripts

Europe PMC Funders Author Manuscripts

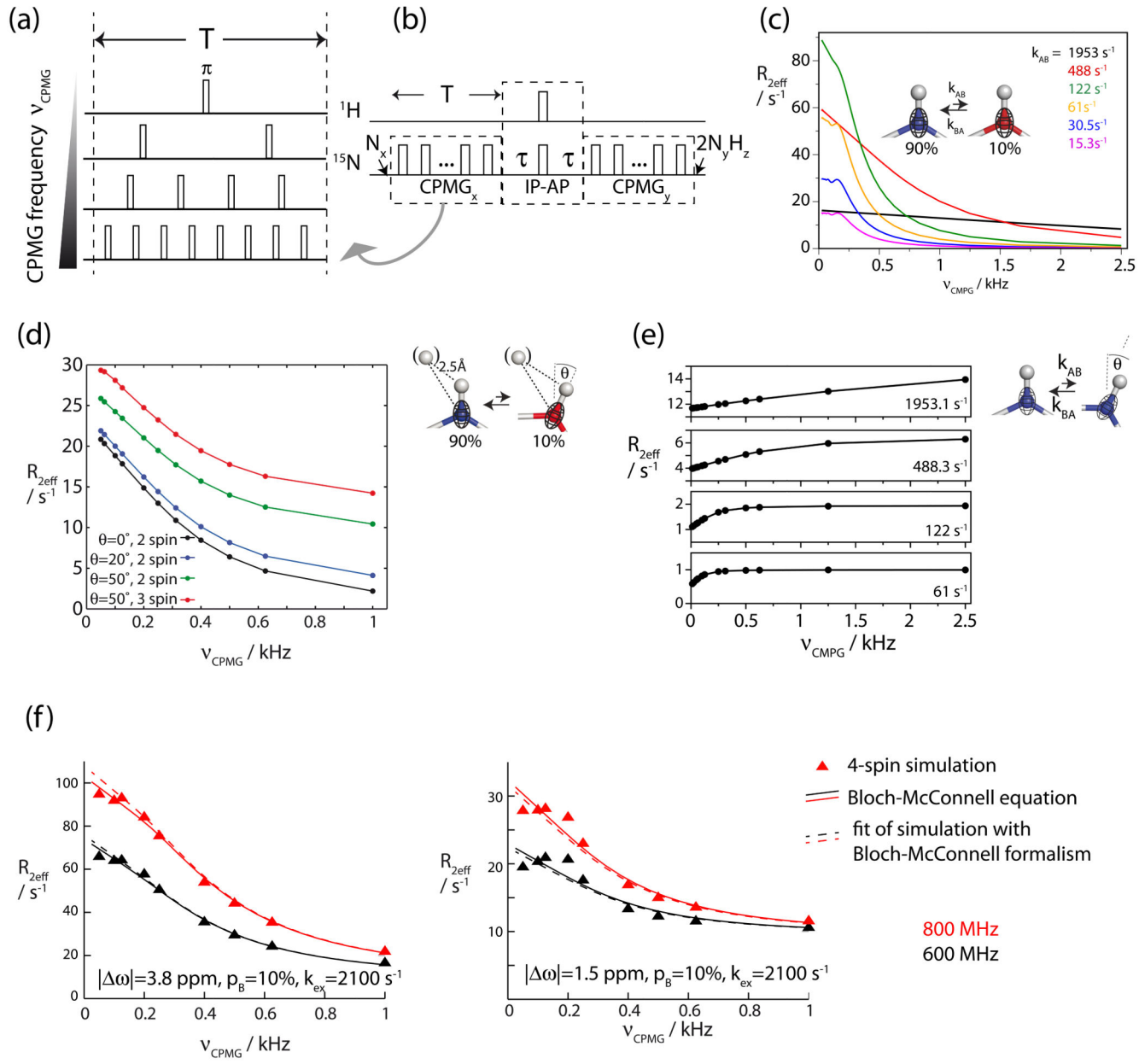

Figure 22.

Carr-Purcell-Meiboom-Gill (CPMG) relaxation dispersion experiments in rotating solids. (a) Illustration of the CPMG pulse sequence element; shown are four different repetition rates of the refocusing pulse train, applied to the ^{15}N nucleus. (b) Implementation of the CPMG pulse element in a so-called relaxation-compensated scheme [143]. In this scheme, an in-phase-to-anti-phase element is inserted in the middle of the constant-time relaxation delay. (c) CPMG dispersion profiles, i.e. effective R_2 rate constants, determined from a 40 ms constant-time relaxation delay, as a function of the CPMG frequency. These profiles were obtained from numerical integration of the Bloch-McConnell equation; they are identical to numerical simulations, assuming that the two states differ exclusively in their ^{15}N isotropic chemical shift, i.e. that the two states are identical in terms of dipolar coupling and CSA.

The two exchanging states (populated to p_A = 90%, p_B = 10%) have a ^{15}N isotropic chemical-shift difference of $|\Delta\omega_{15N}|$ = 300 Hz, and different exchange rate k_{AB} as indicated in the legend. (d) Numerical simulations of the exchange process in a three-spin system, as shown in the insert, in which the NH bond undergoes a jump. In one simulation an additional remote ^1H spin (fixed in space) is included. Here, $k_{ex} = k_{AB}+k_{BA}$ = 2112 s^{-1}, p_B = 10%, $|\Delta\omega_{15N}|$ = 760 Hz and different jump angles are assumed as indicated. (e) Two-spin (HN) simulations, assuming $|\Delta\omega_{15N}| = 0$, p_B = 10%, and different k_{AB}. The jump angle θ = 20° (f) Four-spin simulations (HN pair and two space-fixed remote protons) of CPMG relaxation dispersion, showing the deviation of the dispersion profiles from the Bloch-McConnell-type dispersion curves. The four-spin simulations (triangles) show a “scatter” around the curves corresponding to the Bloch-McConnell calculations for the same exchange parameters. Consequently, the fits (dashed lines) result in systematic errors; the size of these errors, which in this case are within the experimental noise, can be estimated through numerical simulations. Details about these simulations are provided in the Supporting Information of Ref. [44].

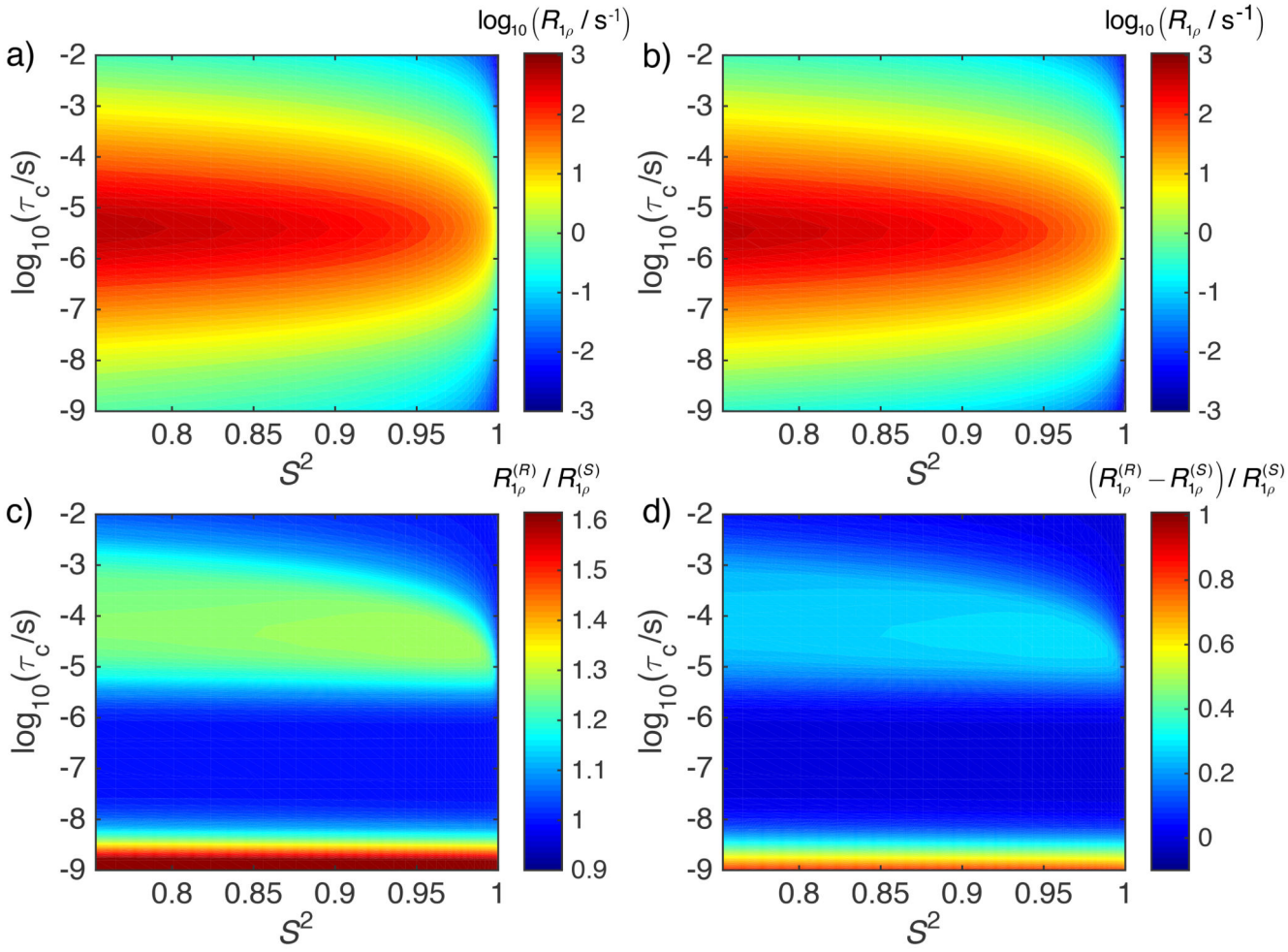

Figure 23.

Comparison of $\log_{10}(R_{1\varrho})$ rate constants calculated with (a) Redfield theory [135] (Eqs. (53) and (54)), and (b) obtained from stochastic Liouville simulations (ν_r = 40 kHz, ν_1 = 12 kHz). Panel (c) shows the ratio of the Redfield and the stochastic calculations while (d) shows the relative difference between the two with the stochastic calculation. The two methods agree very well in the range of correlation times from 10^{-8} s to 10^{-6} s. For longer correlation times, there is a clear difference with the rates calculated by the Redfield approach being larger. For very long correlation times, the agreement becomes better again. For correlation times shorter than 10^{-8} s, there is again a discrepancy between the two methods, which is due to the stochastic simulations being carried out in the rotating frame. As soon as the correlation times approach the Larmor frequencies, such an approach gives wrong results.

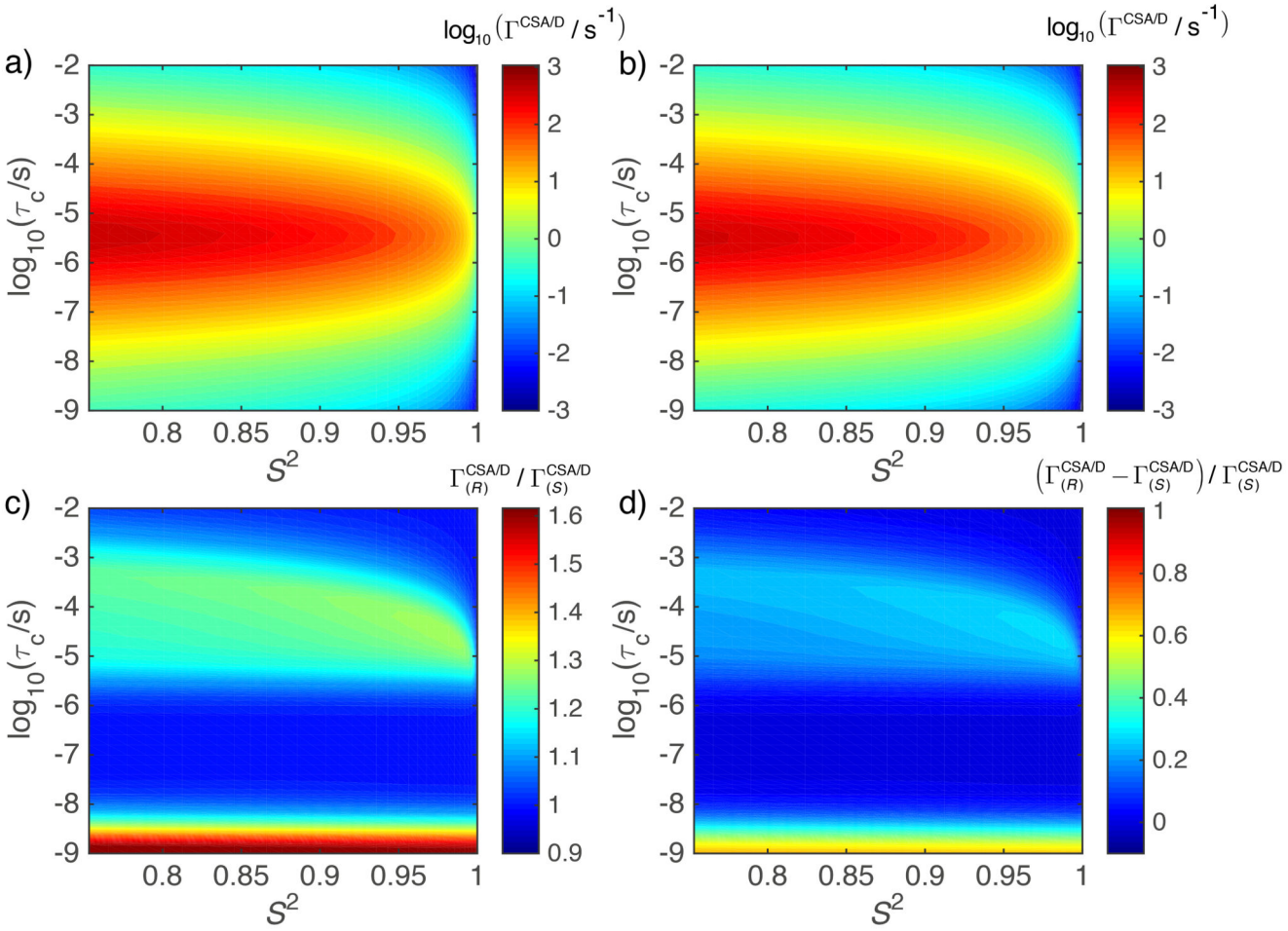

Figure 24.

Comparison of the CSA/D cross-correlated cross-relaxation rate constants $\log_{10}(\Gamma^{CSA/D})$ calculated with (a) Redfield theory and (b) obtained from stochastic Liouville simulations (ν_r = 40 kHz, ν_1 = 12 kHz). Panel (c) shows the ratio of the Redfield and the stochastic calculations while (d) shows the relative difference between the two with the stochastic calculation.

Europe PMC Funders Author Manuscripts

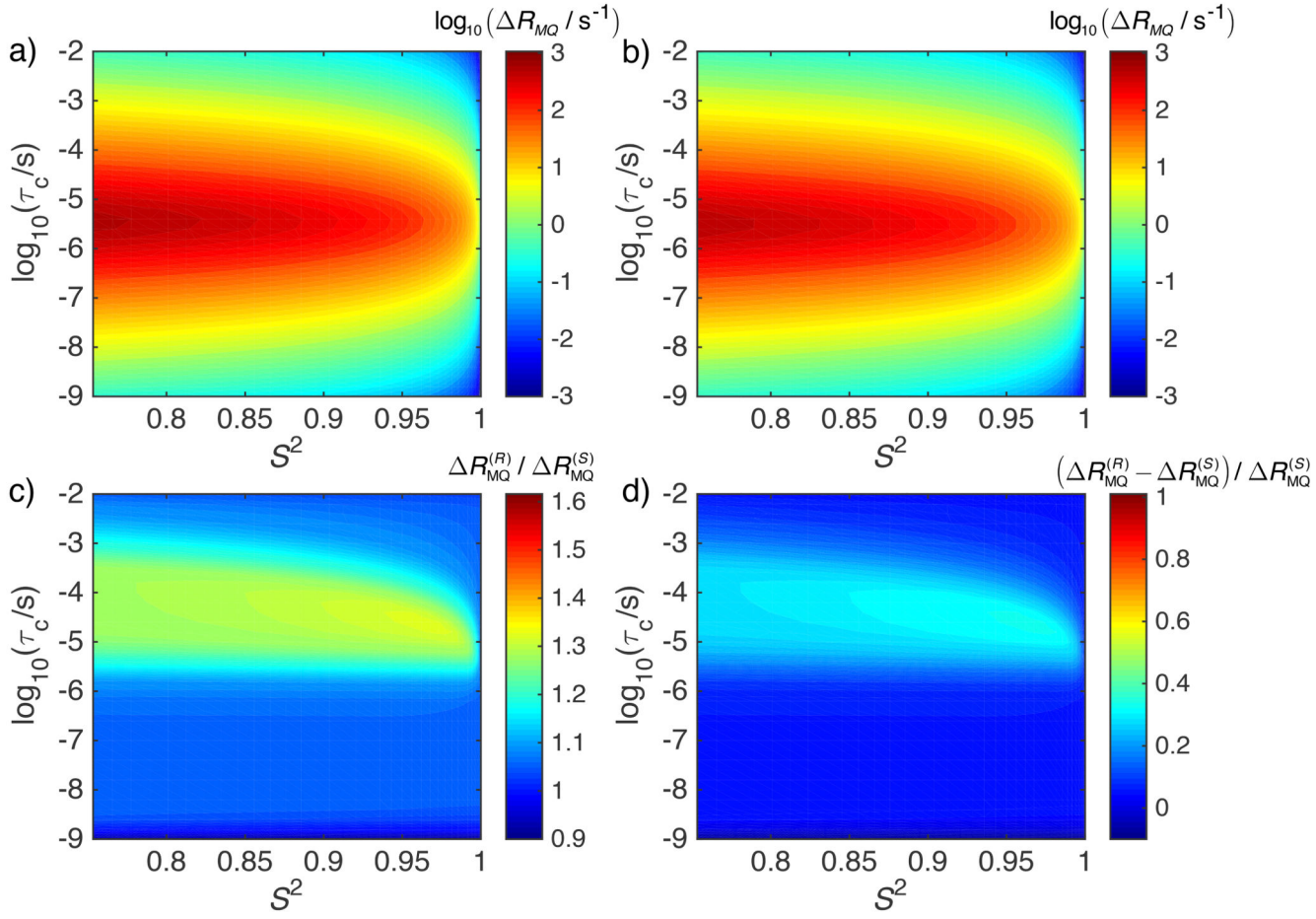

Figure 25.

Comparison of the CSA/CSA cross-correlated cross-relaxation rate constants $\log_{10}(\Delta R_{MQ})$ (Eq. (50)) calculated with (a) Redfield theory and (b) obtained from stochastic Liouville simulations (ν_r = 40 kHz). Panel (c) shows the ratio of the Redfield and the stochastic calculations while (d) shows the relative difference between the two with the stochastic calculation.

Europe PMC Funders Author Manuscripts

Europe PMC Funders Author Manuscripts

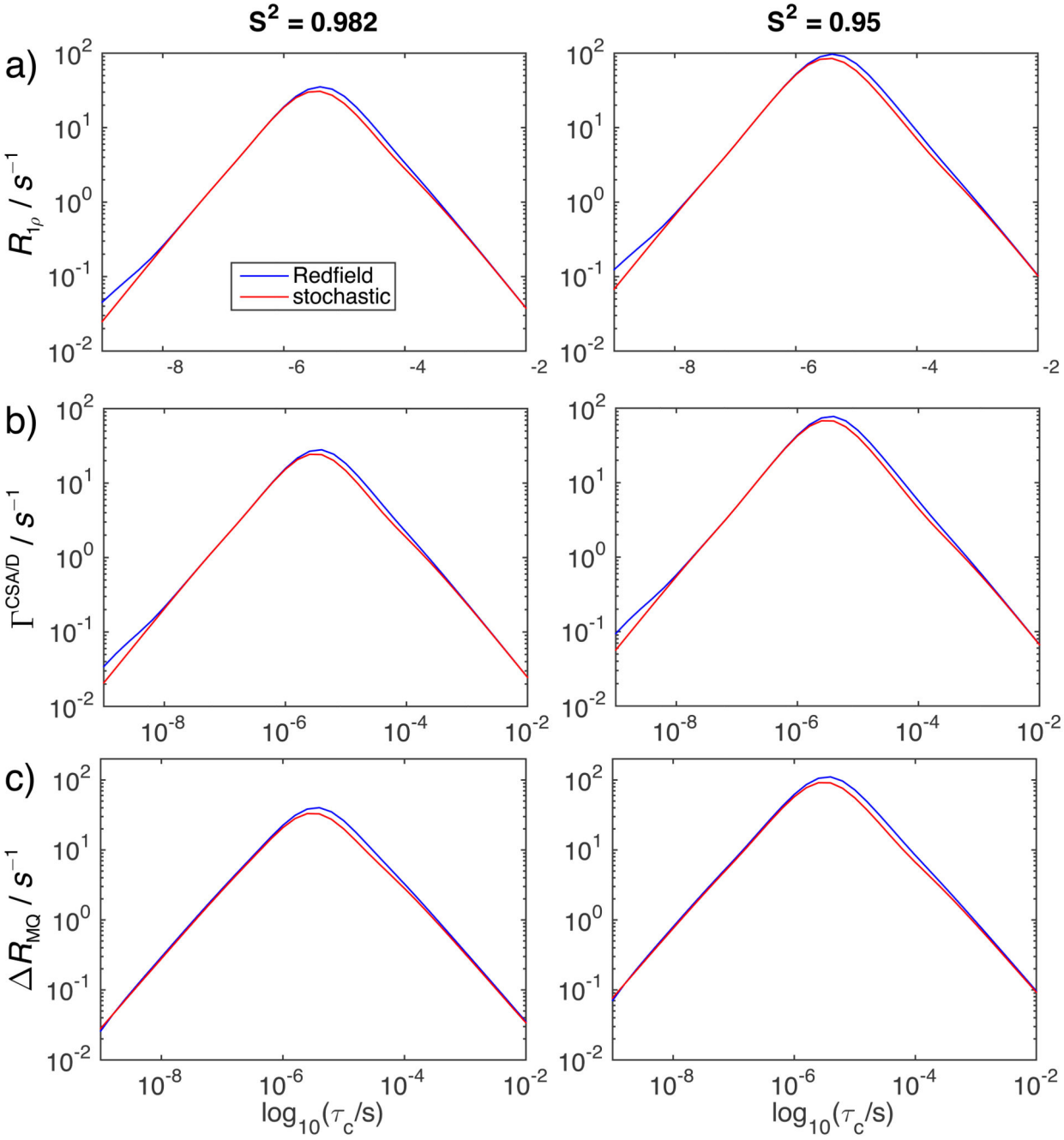

Figure 26.

Slices from Figure 23-Figure 25 at two values of the order parameters. this illustrates the differences between the Redfield and stochastic Liouville approach if the MAS spinning frequency and the stochastic motion are of the same order of magnitude. The differences for very short correlation times are due to the fact that the stochastic simulations are carried out in the rotating frame and do not sample spectral densities at the Larmor frequency and higher.

Europe PMC Funders Author Manuscripts

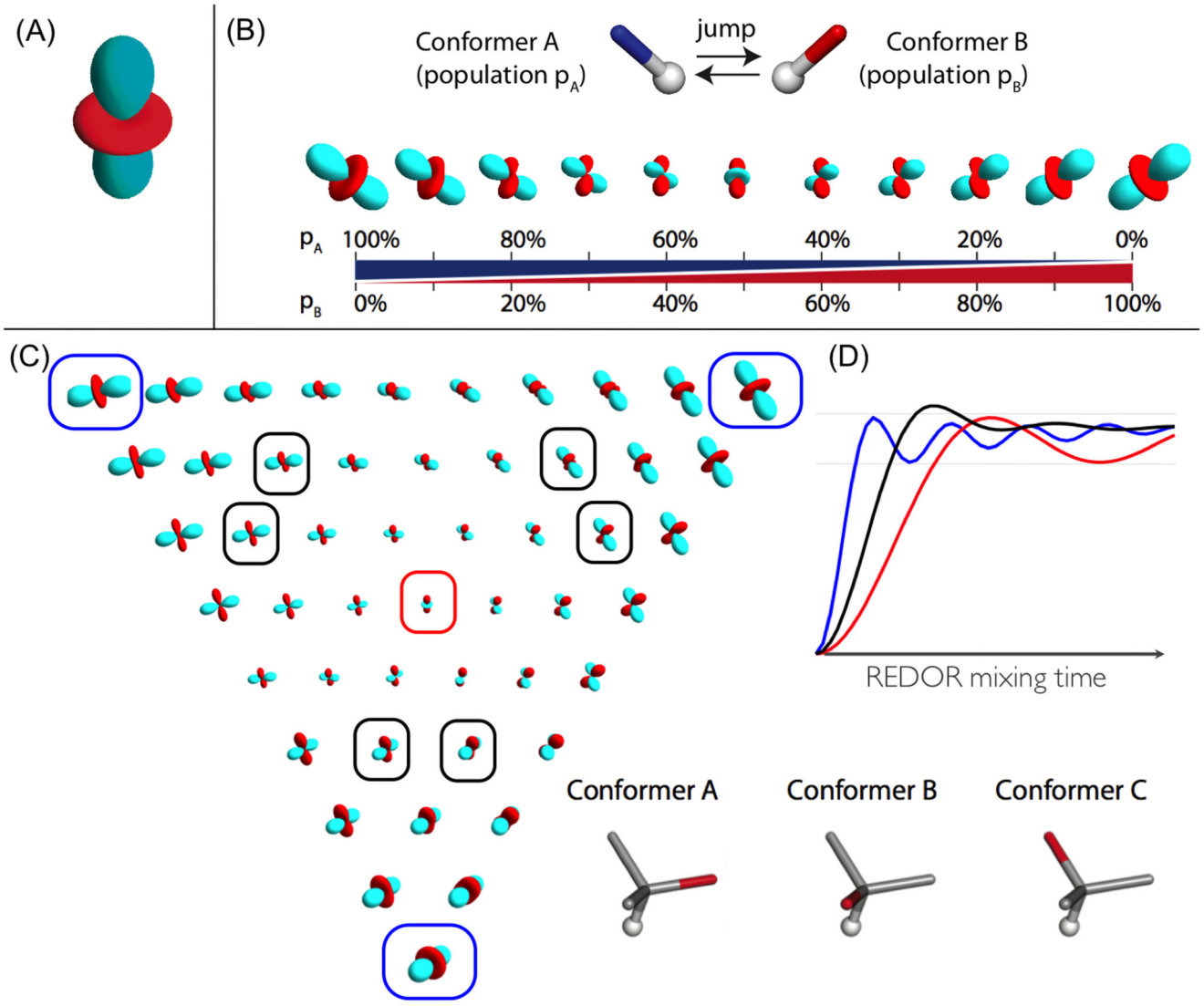

Figure 27.

Graphical representation of a second-rank tensor, and dynamic averaging. (A) Representation of a dipolar-coupling tensor, a symmetric rank-2 tensor. (B) Visualization of the tensor-averaging by a stochastic two-site jump. Here it is assumed that the two conformations, shown in blue and red in the top part are separated by an angle of 90°; the averaged tensors are shown for different relative populations of the two states, ranging from 100% state A (left) to 100% state B (right). As one can readily see, the averaged tensors have a smaller magnitude (tensor anisotropy), and they are generally not axially symmetric any more ($\eta > 0$). (C) Investigation of the tensor averaging resulting from a three-site jump. The three conformations span a tetrahedral geometry (lower right part). The resulting tensors from fast exchange between these states are depicted, as a function of the relative populations of the states; the tensors in the corners of the triangle correspond to 100% of a given conformer. For three examples the tensors are encircled and the corresponding REDOR curves are shown in panel (D). The red curve corresponds to equal population of

the three states (C_3 symmetry), and the REDOR curve is simply scaled relative to the rigid-limit case (blue). In the general case (black), the functional form of the REDOR curve deviates from the simple behavior, which is due to the asymmetry of the averaged tensor.

Europe PMC Funders Author Manuscripts

Europe PMC Funders Author Manuscripts

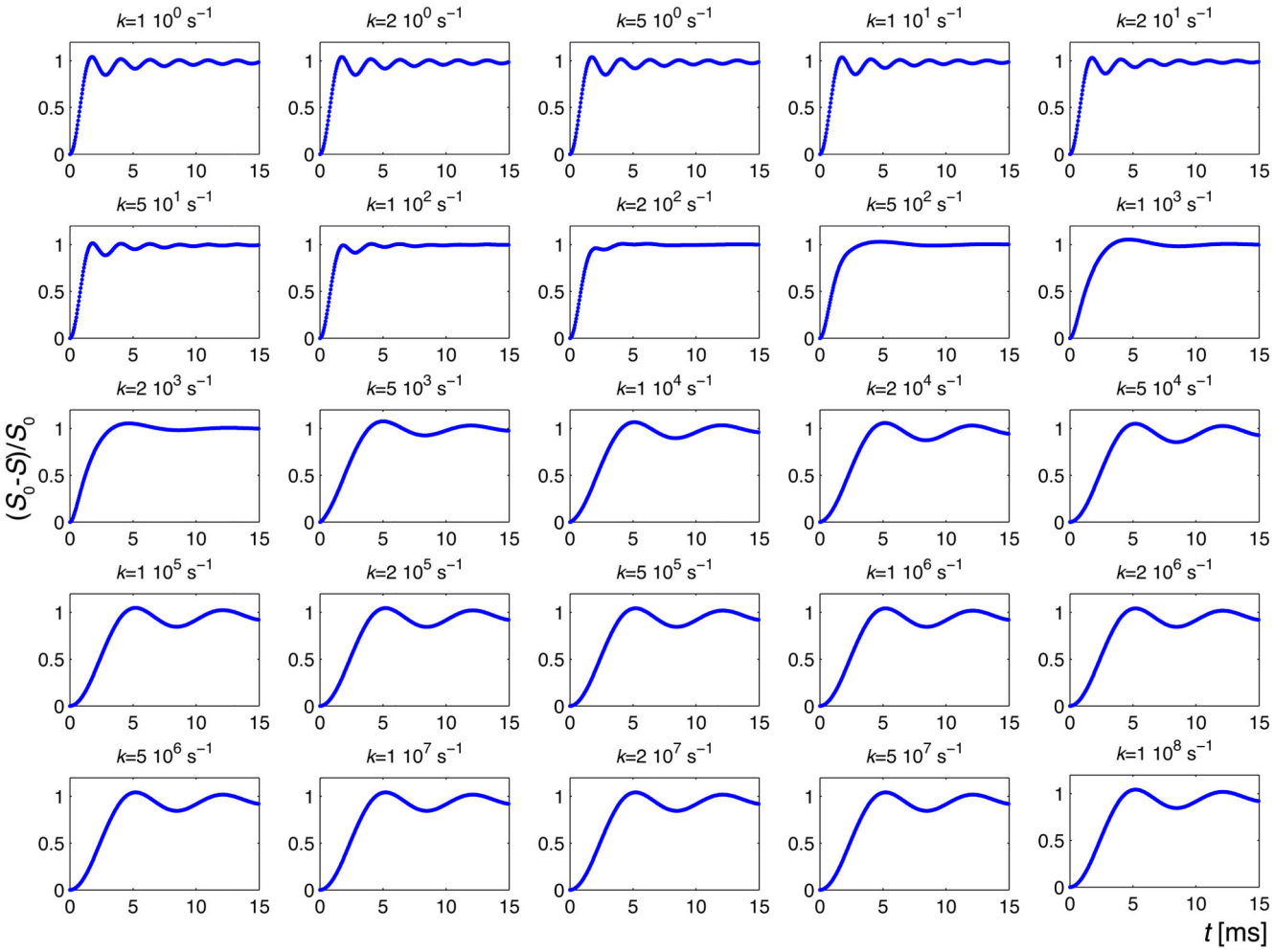

Figure 28.

REDOR curves and averaging of motion occurring at different time scales. These simulations assumed a N-H dipolar coupling with an anisotropy of $\delta_{NH}/(2\pi)$ = 20 kHz at a MAS frequency of 40 kHz. In order to sample the REDOR curve sufficiently during the initial increase, a shifted finite-pulse REDOR sequence [98,148,161] was used with a time shift of 10 μs. Simulated REDOR curves for a shifted finite-pulse REDOR experiment (ν_r = 40 kHz, τ_s = 10 μs, $\nu_{1I} = \nu_{1S}$ = 100 kHz, $\delta_{NH}/(2\pi)$ = 20 kHz) on a two-spin N-H system. The motional model is a symmetric three-site jump model (θ = 70.5°, φ = 120°) where the rate constant was varied between the values 1 s^{-1} and 10^8 s^{-1}.

Europe PMC Funders Author Manuscripts

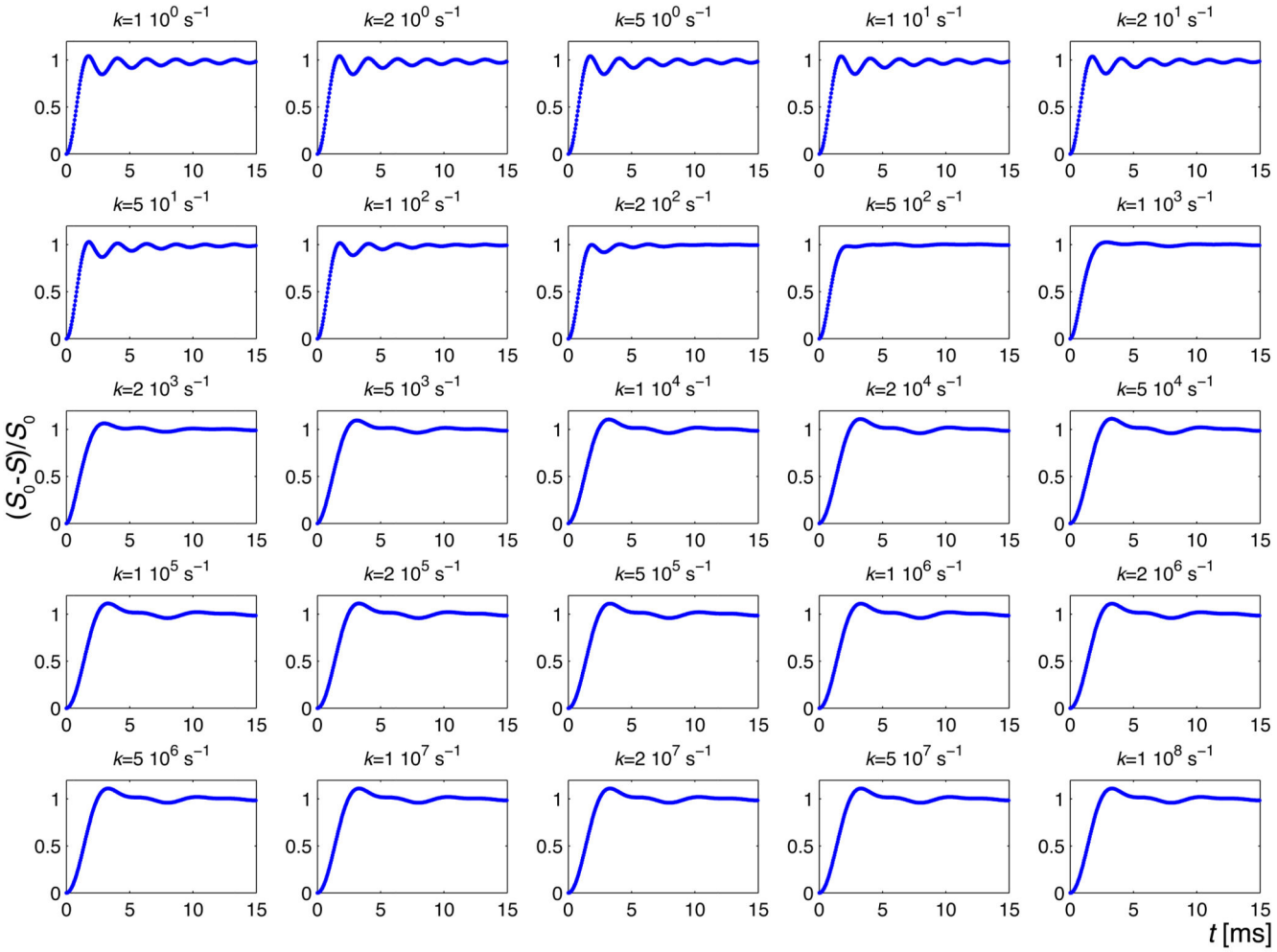

Figure 29.

Simulated REDOR curves for a two-site exchange process. Simulated REDOR curves for a shifted finite-pulse REDOR experiment (ν_r = 40 kHz, τ_s = 10 μs, ν_{1I} = ν_{1S} = 100 kHz, $\delta_{NH}/(2\pi)$ = 20 kHz) on a two-spin N-H system. The motional model is a two-site jump model (θ = 70.5°) where the rate constant was varied between the values 1 s^{-1} and 10^8 s^{-1}. One can clearly see that for large rate constants one does not obtain a typical REDOR curve due to the fact that the averaged dipolar coupling in this case is not axially symmetric.

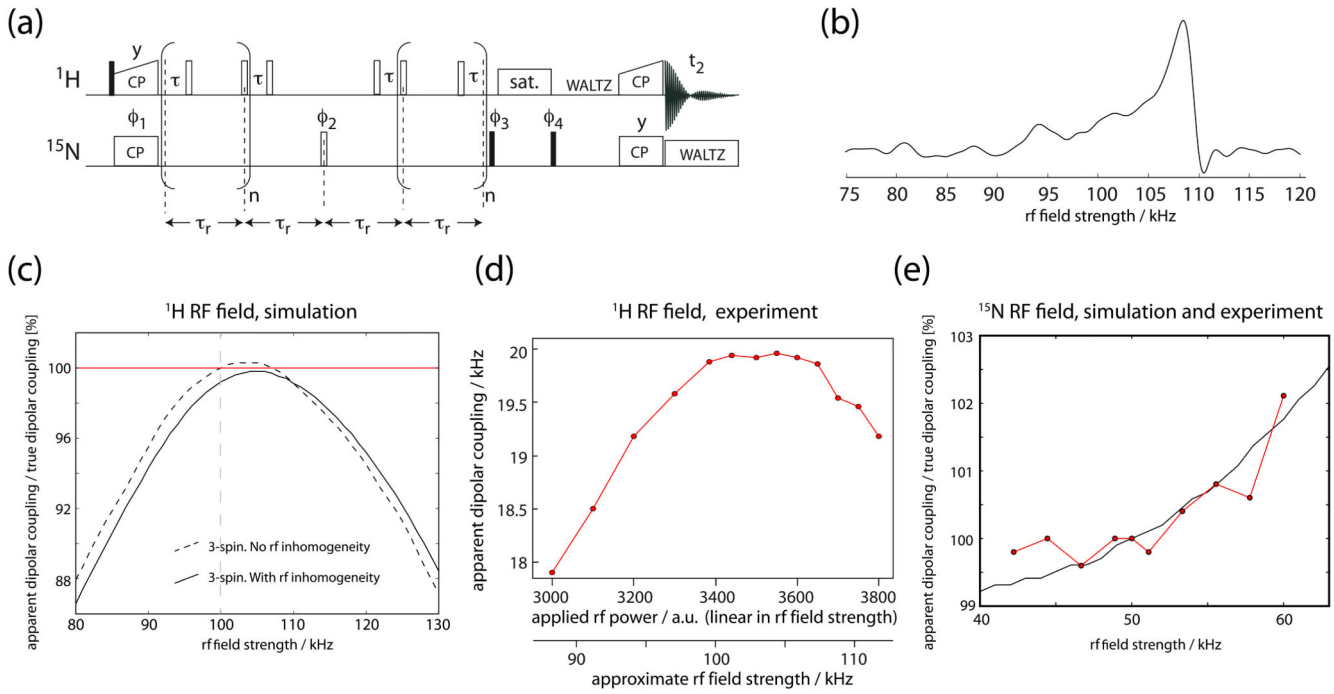

Figure 30.

The effect of RF field misadjustment on apparent dipolar coupling strengths. (a) The pulse sequence used here, a time-shifted REDOR experiment, for measurement of ^{1}H-^{15}N dipolar couplings [98]. (b) RF field distribution in a 1.6 mm HXY probe, obtained by Fourier transformation of a nutation curve. (c) Simulated REDOR curves, obtained with the ^{1}H RF pulses applied at different field strengths (x-axis) were fitted to obtain the apparent dipolar coupling strength (y-axis). A perfect π pulse here has an RF field strength of 100 kHz (5 μs duration). Deviations of the apparent dipolar coupling from the nominal value (red line) are seen when the RF field is misadjusted. The dashed line results when RF inhomogeneity is included explicitly in the simulations. (d) Experimental verification of the data in panel (c). 1D REDOR curves were measured with different RF field settings (x-axis) and the apparent dipolar coupling was extracted by numerical fits of the REDOR curves. Similar to the simulated case, the dipolar coupling is underestimated when the RF field is misset. (e) Similar simulations and experiments, with the ^{15}N RF field being varied. Details can be found in reference [110].

Europe PMC Funders Author Manuscripts

Europe PMC Funders Author Manuscripts

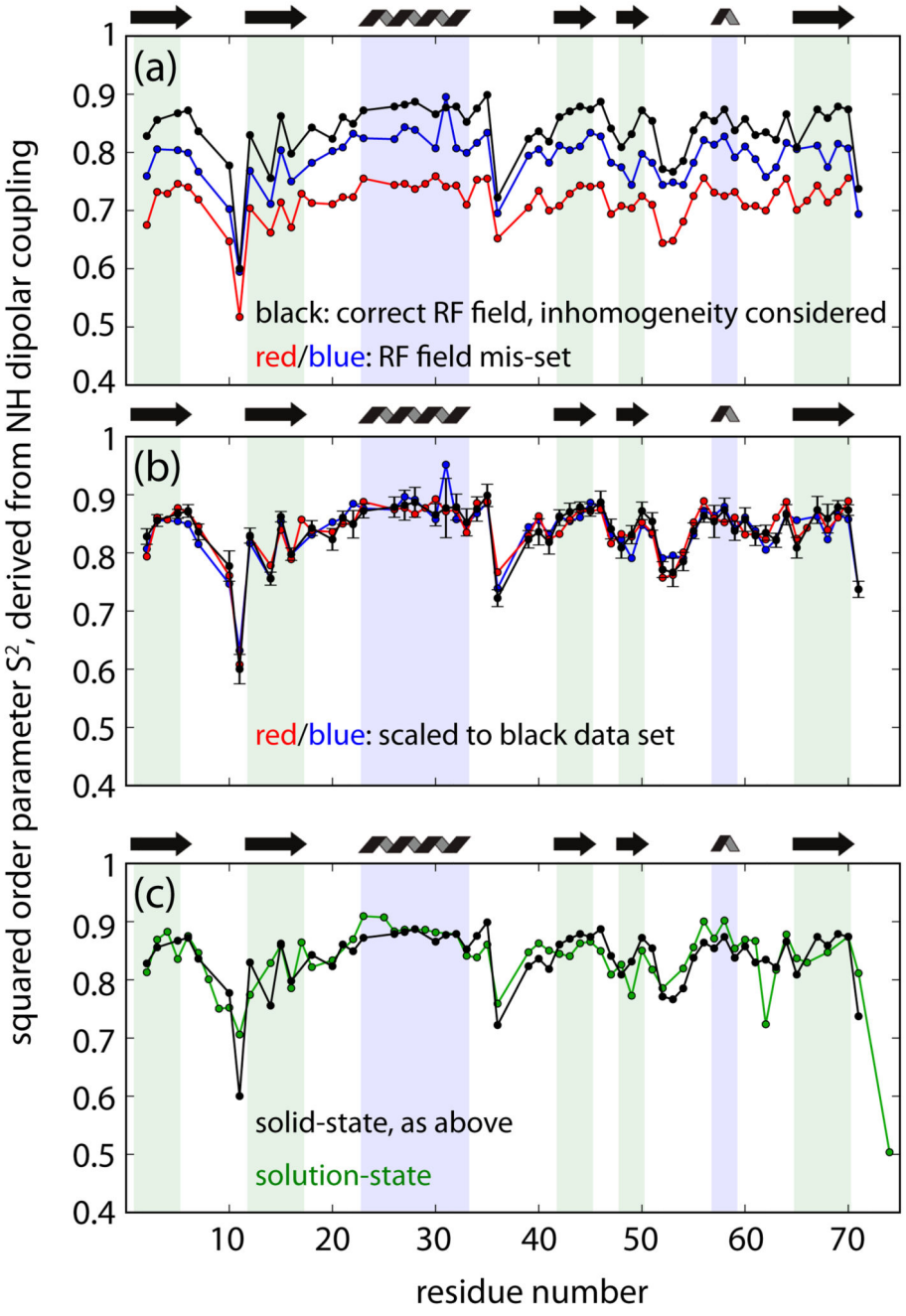

Figure 31.

REDOR-derived HN order parameters in ubiquitin. (a) Three different measurements of dipolar order parameters, using best-possible RF calibration, and explicit consideration of the RF inhomogeneity upon fitting (black), as well as two measurements with slightly misset RF field strengths (blue, red). In (b), the red and blue data set have been multiplied by a factor that minimizes the offset to the black data set. Panel (c) shows a comparison to solution-state order parameters (derived from relaxation measurements). See reference [110] for details.

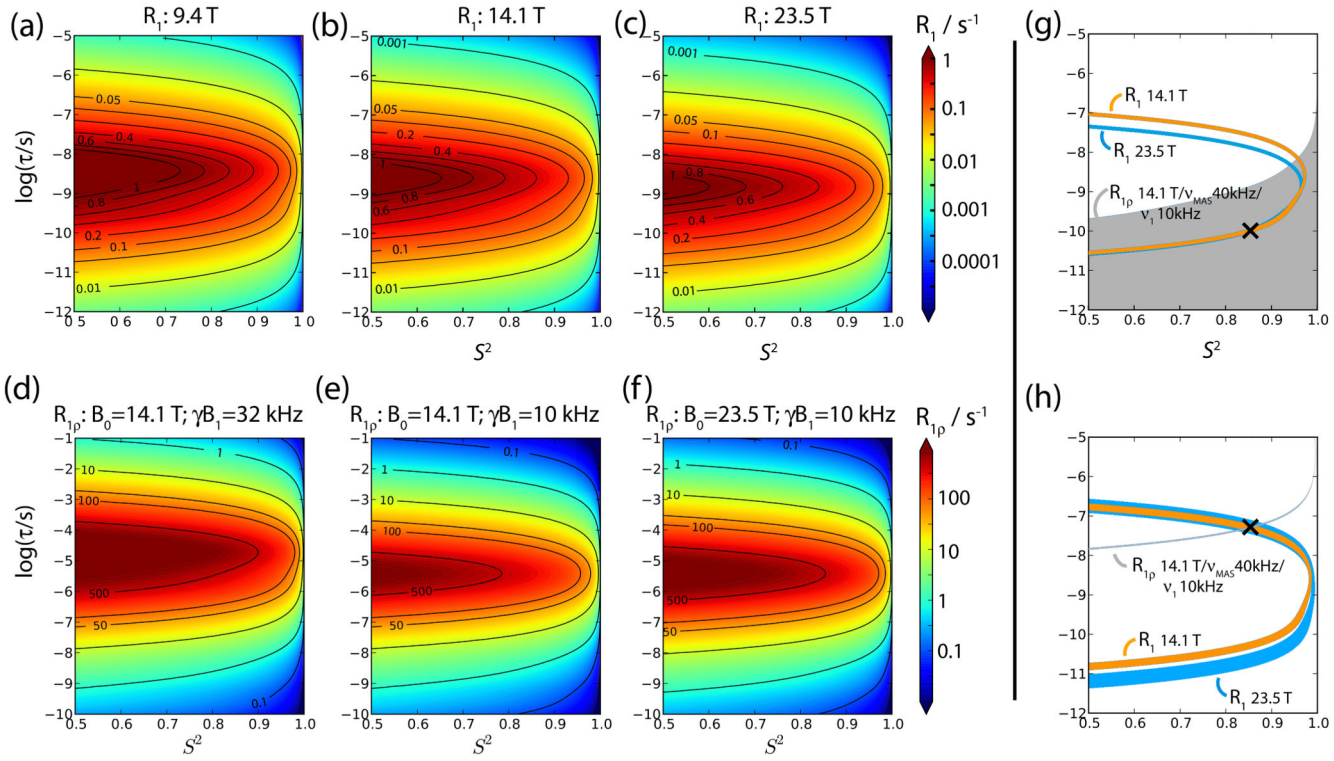

Figure 32.

^{15}N relaxation rate constants as a function of motional parameters within the model-free approach. Panels (a), (b) and (c) represent ^{15}N R_1 relaxation rate constants at field strengths corresponding to 400, 600 and 1000 MHz ^{1}H Larmor frequencies, respectively. Panels (d), (e) and (f) show ^{15}N $R_{1\varrho}$ relaxation rate constants, at 40 kHz MAS frequency. The B_0 field strength and spin-lock RF field strengths are indicated above the panels. Note that the vertical axis in panels (a)-(c) range from 1 ps to 10 μs, while in panels (d)-(f) it extends from 100 ps to 100 ms. Panels (g) and (h) illustrate two concrete examples of motional scenarios, and how given motional parameters are reflected in relaxation rate constants. In (g) it is assumed that the motion is described by an order parameter $S^2 = 0.85$, and a correlation time constant $\tau = 100$ ps, as indicated by a cross. The relaxation rate constants (R_1 at 14.1 T, R_1 at 23.5 T and $R_{1\varrho}$ at 14.1 T, 40 kHz MAS and 10 kHz spin-lock) were calculated, and realistic noise levels were added to these rate constants (0.009 s^{-1} for R_1, 0.4 s^{-1} for $R_{1\varrho}$). The grey area represents the regions of the parameter space (S^2, τ) which are in agreement with the relaxation rate constants. It is evident that the two R_1 relaxation rate constants fail to restrain the S^2 values; the possible parameter space for the $R_{1\varrho}$ measurement is very large, owing to the fact that for such fast motions the $R_{1\varrho}$ rate constant is very small compared to its uncertainty. Thus, the amplitude of such fast motion can hardly be fitted from any relaxation measurements. Panel (h) shows a similar analysis for slower motion ($S^2 = 0.85$, $\tau = 50$ ns). As $R_{1\varrho}$ is sensitive to such slower motion, the combined information from R_1 and $R_{1\varrho}$ measurements allows the motional parameters to be defined. See text for further discussion.

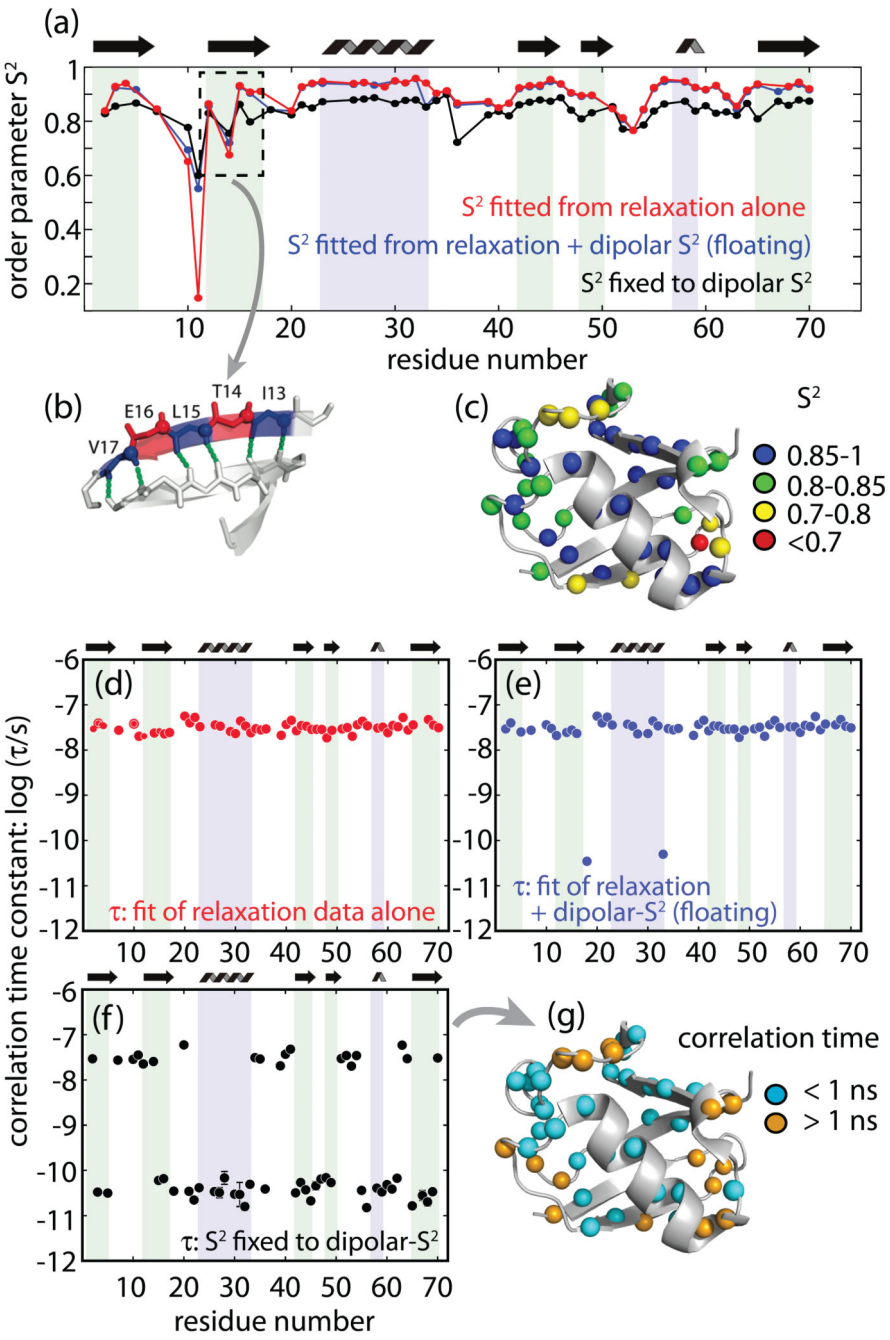

Figure 33.

Model-free fits of backbone dynamics in microcrystalline ubiquitin. For these fits, ^{15}N R_1 rate constants (3 different B_0 fields), ^{1}H-^{15}N dipolar-^{15}N CSA cross-correlated relaxation (2 different B_0 fields) and ^{15}N $R_{1\varrho}$ rate constants were used, as well as ^{1}H-^{15}N dipolar-coupling derived order parameters. (a) Order parameters S^2 obtained from three different fit approaches: (i) fitting relaxation data without the dipolar order parameters (red), (ii) including the dipolar-S^2 in the fit, but not fixing the order parameter to the dipolar-S^2 (blue) and (iii) fixing the S^2 to the dipolar-S^2 (black). (b) Zoom into part of the β-strand that has

alternating pattern of high/low S^2 values, and alternating H-bonding pattern. (c) Plot of S^2 values on the structure. The corresponding time scales for the three cases are shown in (d), (e) and (f), respectively. Panel (g) shows the correlation times from panel (f) on the structure. Note that the dipolar-S^2 are very similar to solution-state S^2 (see Figure 31), whereas a fit of R_1 and $R_{1\varrho}$ leads to systematically higher S^2 and detection of nanosecond motion for all residues. Figure reproduced from reference [110].

Europe PMC Funders Author Manuscripts

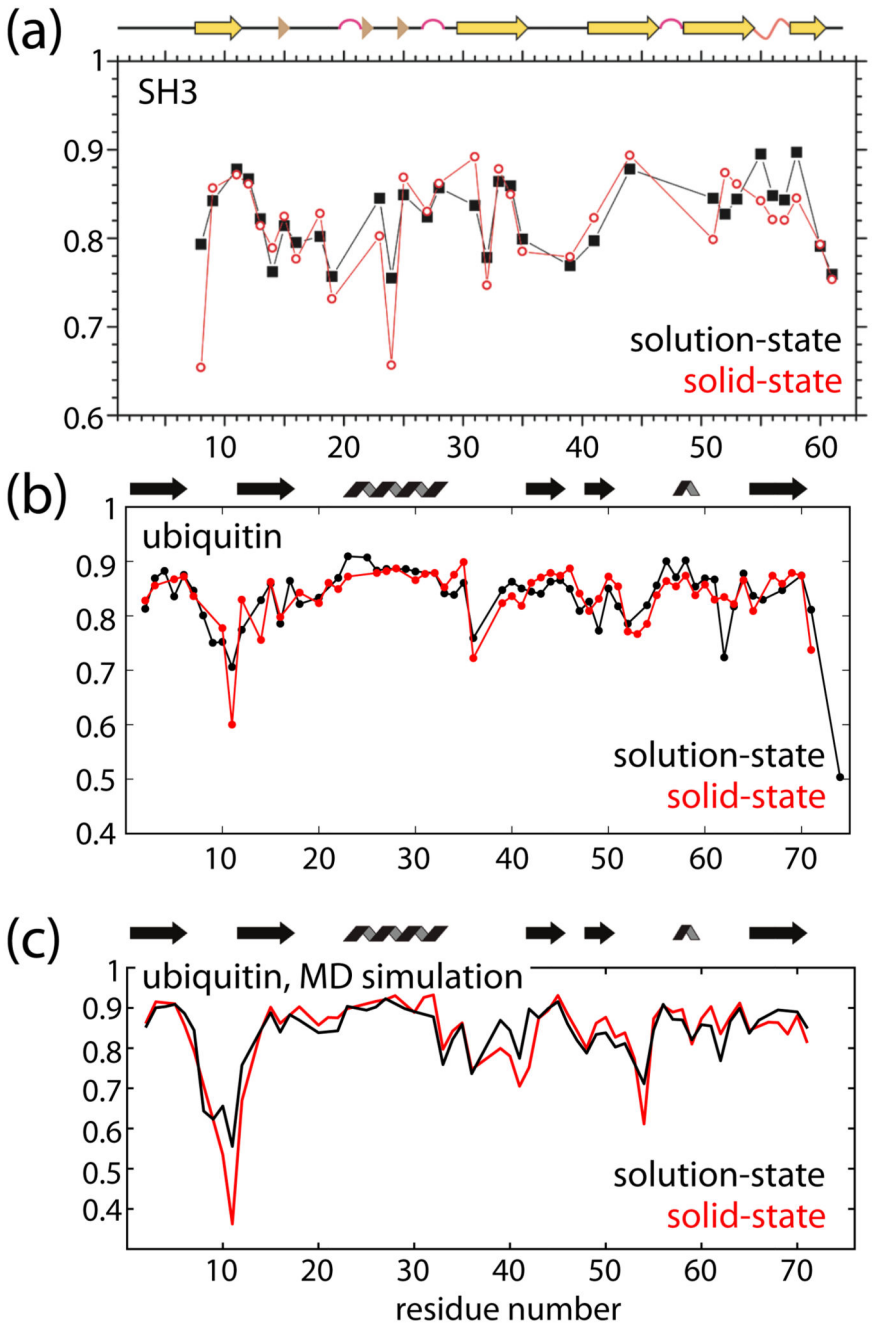

Figure 34.

Backbone NH order parameters in solution and crystals in SH3 (a) and ubiquitin (b,c). Data in panels (a) and (b) are from HN dipolar couplings obtained on crystalline SH3 [182] and ubiquitin [110], respectively, or from ^{15}N spin relaxation measurements (for the corresponding solution-state samples). In panel (a), only those residues are shown for which both solution- and solid-state data are available. Data in panel (c) are from MD simulations. For the simulation of the crystalline protein an explicit crystal lattice, composed of 48 molecules was simulated, according to the crystalline arrangement in the experimental

structure. Water was explicitly simulated in both the solution- and crystal-state MD simulation. Details can be found in reference [189].

Europe PMC Funders Author Manuscripts

Europe PMC Funders Author Manuscripts

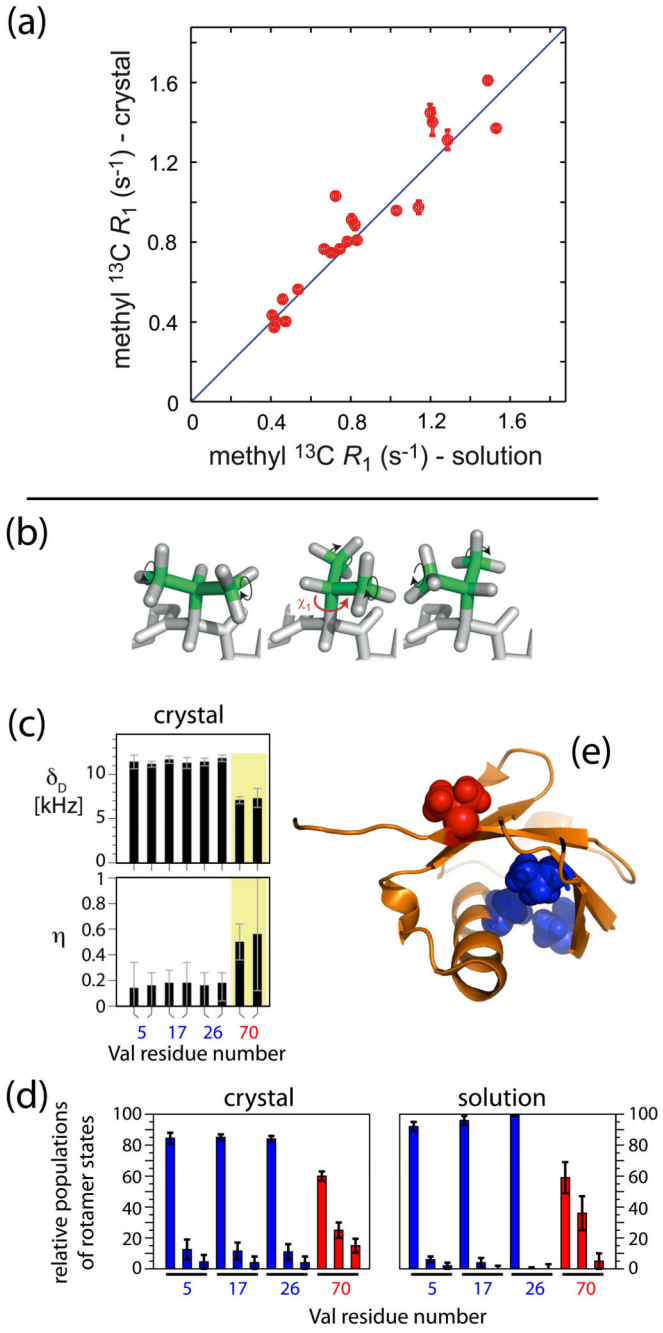

Figure 35.

Methyl side chain dynamics in solution and crystal as seen by solid- and solution-state NMR. (a) ^{13}C R_1 relaxation rate constants in CHD_2-labeled Val/Leu methyl groups in the protein SH3. The effect of overall tumbling on the solution-state rate constants has been subtracted out. A high degree of correlation is evident, providing evidence that sub-microsecond side chain motions in solution and crystals are similar. Panels (b) to (e) show Val methyl side chain dynamics in the protein ubiquitin. Here, the focus is on side chain rotamer jumps; possible rotamer states for Val side chains are depicted in panel (b).

Asymmetric dipolar couplings (c), characterized by their tensor anisotropy δ_D and asymmetry η show that Val 70 has a higher amplitude of motion than Val 5, 17 and 26 [154]. In (d) these data were used to compute relative rotamer populations for valines in the crystal sample, assuming the three-site jump model from panel (b). For each Val residue, three bars are shown, representing the populations of the three rotamer states (ordered by decreasing population level, as the populations cannot be unambiguously assigned to gauche+, gauche and trans states). Also shown in (d) are solution-state rotamer populations [188], obtained from analysis of J-couplings. As in the crystal, Val 70 populates all three rotamers, while Val 5, 17 and 26 populate essentially only one rotamer. (e) Location of the Val residues in the ubiquitin structure.

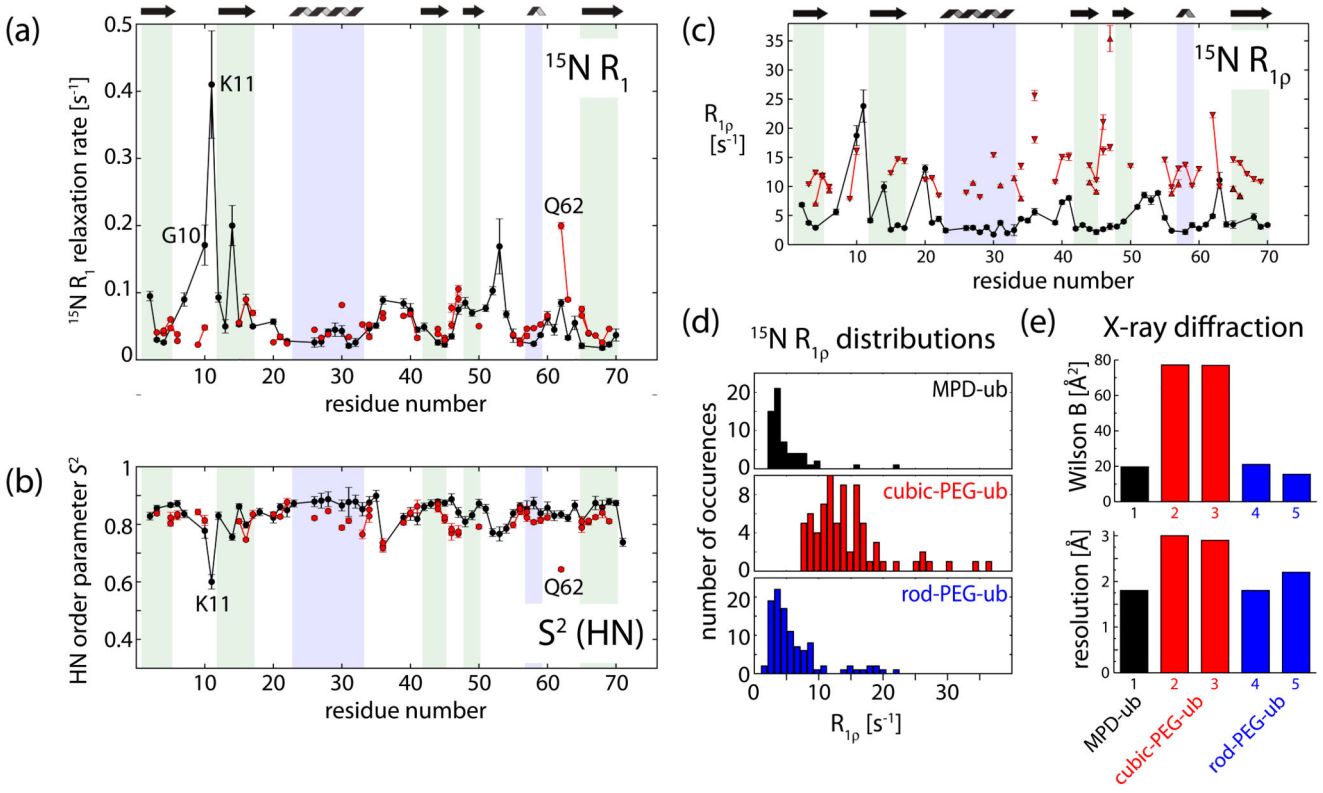

Figure 36.

Backbone dynamics in different crystal forms of the protein ubiquitin. All data shown in black are from ubiquitin crystals obtained with the precipitant MPD (which is the crystal form used in all discussions above), data in red are from cubic-shaped crystals obtained with the precipitant PEG, and data in blue are from rod-shaped ubiquitin crystals with PEG. Panels (a)-(c) show residue-wise comparisons of ^{15}N R_1 rate constants, HN dipolar order parameters and ^{15}N $R_{1\varrho}$ rate constants, respectively. While ^{15}N R_1 rate constants and S^2 values are similar in the two crystals, the ^{15}N $R_{1\varrho}$ rate constant is clearly offset in cubic-PEG-ub, as compared to MPD-ub (c). In (d) a histogram of ^{15}N $R_{1\varrho}$ rate constants is shown for the two crystal forms shown in panels (a)-(c), as well as the third crystal form, rod-PEG-ub. The overall increased ^{15}N $R_{1\varrho}$ in cubic-PEG-ub points to an overall motion of the molecule in this crystal form. Panel (e) provides evidence that such a restricted overall motion also has consequences for X-ray observables: cubic-PEG-ub crystals diffract to lower resolution, and the Wilson-B factor is higher than in the other two crystal forms (two independent data sets are reported for the PEG-derived crystals). Reproduced with permission from reference [189].

Europe PMC Funders Author Manuscripts

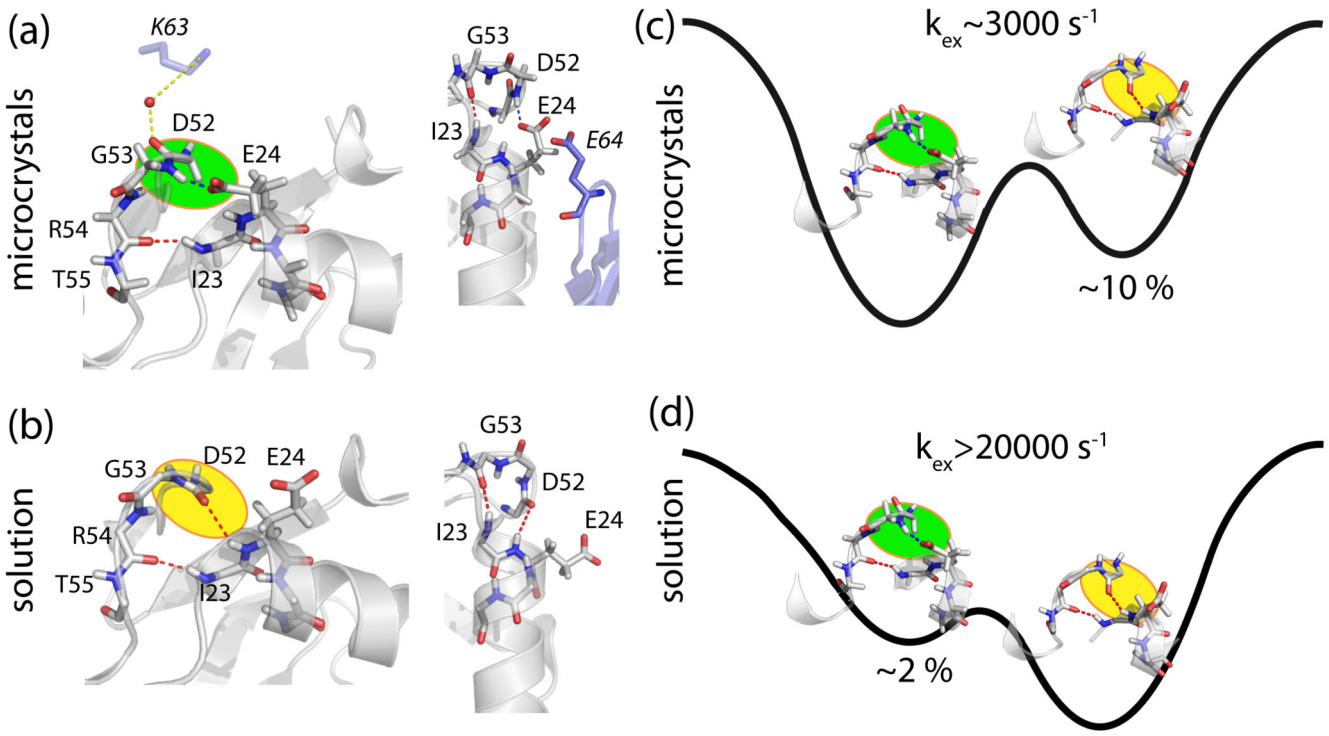

Figure 37.

Conformational exchange processes on μs time scales in ubiquitin in solution and crystals. (a) Zoom into the crystal structure of the crystals used for solid-state NMR studies. The peptide plane 52/53, which presumably undergoes an exchange process, is highlighted. The hydrogen bonding of this β-turn loop to the adjacent helix is also indicated. Molecules shown in blue are neighboring molecules in the crystal. (b) Zoom into the equivalent part in the solution-state structure. Note that the hydrogen bonding is changed, the peptide plane 52/53 is flipped relative to its orientation in (a), as indicated by colored circles, and the side chain of E24 is pointing outward. Panels (c) and (d) show schematic free-energy landscapes (free energy is increasing vertically); the exchange rate constant and the populations of the "minor state", as determined from relaxation-dispersion NMR in solids and solution, respectively, are indicated. The slowing-down of the exchange process in crystals may be explained by steric hindrance of side chain E24 which contacts E64 of a neighboring molecule in the crystal, and the stabilization of the peptide plane conformation of D52/G53 (water-mediated H-bond to K63 of neighboring molecule).

Europe PMC Funders Author Manuscripts